Interface dynamics of soft solids with liquids, solids, and gels

by

A-Reum Kim

A thesis

presented to the University of Waterloo

in fulfillment of the

thesis requirement for the degree of

Doctor of Philosophy

in

Chemical Engineering (Nanotechnology)

Waterloo, Ontario, Canada, 2023

Examining Committee Membership

The following served on the Examining Committee for this thesis. The decision of the Examining Committee is by majority vote.

External Examiner	**Prof. Benjamin D. Hatton** Professor, Department of Materials Science & Engineering
Supervisor	**Prof. Boxin Zhao** Professor, Department of Chemical Engineering
Supervisor	**Prof. Sushanta K. Mitra** Professor, Department of Mechanical & Mechatronics Engineering
Internal Member	**Prof. Tizazu Mekonnen** Professor, Department of Chemical Engineering
Internal Member	**Prof. Marios Ioannidis** Professor, Department of Chemical Engineering
Internal-external Member	**Prof. Carolyn Ren** Professor, Department of Mechanical & Mechatronics Engineering

Author's Declaration

This thesis consists of material, all of which I authored or co-authored: see the Statement of Contributions included in the thesis. This is a true copy of the thesis, including any required final revisions, as accepted by my examiners.

I understand that my thesis may be made electronically available to the public.

Statement of Contributions

Chapter 2 is published as: **A-Reum Kim**, Aleksander Cholewinski, Sushanta K. Mitra, and Boxin Zhao. "Viscoelastic Tribopairs in Dry and Lubricated Sliding Friction." *Soft Matter,* 2020, vol. 16 (32). 7447-7457.

- The contributions of the co-authors are as follows: B.Z. and S.K.M. conceived the study. A-R.K., performed the experiments and analyzed the data. All authors discussed the results. A-R.K. wrote the manuscript with inputs from B.Z. and S.K.M., which was proofread by A.C. B.Z. and S.K.M. B.Z. and S.K.M. supervised the research.

Chapter 3 is published as: **A-Reum Kim**, Sushanta K. Mitra, and Boxin Zhao. "Capillary Pressure Mediated Long-Term Dynamics of Thin Soft Films." *Journal of Colloid and Interface Science,* 2022, vol. 628. 788-797.

- The contributions of the co-authors are as follows: B.Z. and S.K.M. conceived the study. A-R.K. performed the experiments and analyzed the data. All authors discussed the results. A-R.K. wrote the manuscript with inputs from B.Z. and S.K.M. B.Z. and S.K.M. supervised the research.

Chapter 4 is published as: **A-Reum Kim**, Sushanta K. Mitra, and Boxin Zhao. "Reduced Pressure Drop in Viscoelastic Polydimethylsiloxane Wall Channels." *Langmuir*, 2021, vol. 37 (49). 1429-14301.

- The contributions of the co-authors are as follows: B.Z. and S.K.M. conceived the study. A-R.K. performed the experiments and analyzed the data. All authors discussed the results. A-R.K. wrote the manuscript with inputs from B.Z. and S.K.M. B.Z. and S.K.M. supervised the research.

Chapter 5 is submitted as: **A-Reum Kim**, Surjyasish Mitra, Sudip Shyam, Sushanta K. Mitra, Boxin Zhao. “Connecting Adhesion and Wetting with a Hydrogel Bridge.”

- A-R.K. and S.M. equally contributed.
- The contributions of the co-authors are as follows: B.Z. and S.K.M. conceived the study. A-R.K., S.M., and S.S. performed the experiments and analyzed the data. All authors discussed the results. S.M. wrote the manuscript draft with inputs from A-R.K., S.S., B.Z., and S.K.M., which was revised by all of us. B.Z. and S.K.M. supervised the research.

Abstract

Soft solids are commonly composed of polymeric networks suspended in liquids while maintaining their physical form. They have intermediate properties between viscous liquids and elastic solids, which are easily deformed even by small stresses (*e.g.*, the interfacial tension with liquid droplets) but also resist deformation. Their distinctive softness has attracted many researchers and engineers to fruitfully apply soft solids in modern technologies such as 3D printing, *in-vitro* studies, soft robots, diagnostic chips, and artificial organs. In addition, many biological materials are soft solids, such as living tissues capable of conforming to the surface shape of the culture substrate and easily adapting to the surrounding environment.

The intermediate properties of soft solids create distinctive and unpredictable behaviors at interfaces beyond the scope of classical physics for pure liquids and solids. For example, soft solids show a time lag between the applied stress and the resultant strain. In addition, under certain extreme stress, soft solids might experience phase-separation between liquid and solid phases. Also, the polymeric chains might cause stick-slip motions of spreading liquid or sliding solid in contact with the soft polymeric surfaces. Understanding and controlling the different interfacial properties (*e.g.*, lubrication, adhesion, and wetting) of soft solids are crucial to developing advanced technologies for using soft solids and better understanding the wisdom of nature. However, the physical principles behind numerous phenomena at soft interfaces are not yet clearly understood. Thus, the objective of this dissertation was to reveal the root causes of the salient features of different soft contact systems: soft solids in contact with sliding solids, flowing fluids, and stationary solids and gels.

The sliding tribosystem is one of the most prevalent contact systems. In this thesis, the role of viscoelasticity was first investigated on the sliding tribological behavior with and without lubricants. The lateral friction force of purely soft tribopairs (soft-on-soft) was examined. Through a regression analysis, a correlation was found among key parameters (*e.g.*, sliding speed, preload, and viscoelasticity), showing the

significant role of the loss tangent in the friction coefficient. On the one hand, above a certain level of free liquids in the elastic network of tribopairs (~ 30 wt.%), the liquid phase predominantly reduced the friction coefficient, potentially working as a lubricant at the interface.

Inspired by the findings on the role of the free liquids in the sliding tribosystem, a more detailed study on the surface deformation of soft solids with a larger fraction of liquids (~ 62 wt.%) (*i.e.*, gel) was further investigated in contact with a stationary glass sphere. The soft surface evolved significantly longer (~ 85 hr) than its typical time scale (milliseconds) while the resultant strain was still within the elastic limit. The reasons behind this were the predominant finite-size and preload effects, minimized or neglected in most conventional and modified contact theories. The scope of research in this thesis was further expanded by engaging flowing Newtonian fluids (*e.g.*, water and glycerol) in contact with soft solids.

The role of viscoelastic solids was researched on the flowing fluids by measuring the pressure drop of flowing fluids. To focus on the interface dynamics between soft solids and flowing fluids, the deflection of soft walls (*i.e.*, bulging effect) was prevented by fabricating soft walls inside a rigid backing layer (*i.e.*, rigid tube). Nonetheless, soft wall channels presented a reduced pressure drop compared to the calculated value of the Hagen-Poiseuille equation for rigid channels. As the free liquids fraction of the soft walls increased, the lower pressure drop was measured, implying that less energy was consumed. The cause of this reduced pressure drop was found to be the lubricating effect of free liquids on the soft surfaces, which was confirmed through dynamic contact angle measurements.

Lastly, via gels, the static contact signatures of two extreme physical states, pure liquids and solids, were bridged. A broad range of the effective elasticity of contact pairs was investigated from as low as near zero Pa to a few GPa. A scaling law was provided, connecting the wetting and adhesive contact regimes based on the measured contact radius and wetting foot. In addition, the experimental findings were validated through comparison with the experimental data presented in previous representative studies.

Acknowledgments

As the journey of graduate school study and research is coming to an end, I would like to sincerely thank everyone who has been a part of my graduate career at the University of Waterloo. Most importantly, I would like to express my deepest appreciation to my supervisors, Prof. Sushanta K. Mitra and Prof. Boxin Zhao. Under their guidance, I am privileged to do my Ph.D. studies at two laboratories allowing me to access more diverse experimental resources and learn from many other researchers. They guided me through this journey with great patience and intellectual input all the time. I do not have enough words to express my gratitude for their support throughout my Ph.D. studies. Had I not worked with them, I would have missed the true joy of questioning and the fruitful experience of filling the knowledge gap as a researcher.

I would like to show my gratitude to my lab colleagues for their help and meaningful suggestions. I am also grateful to my committee, Prof. Tizazu Mekonnen, Prof. Marios Ioannidis, and Prof. Carolyn Ren, and my external examiner, Prof. Benjamin D. Hatton, for helpful discussion on my research.

I am also thankful to the Department of Chemical Engineering, the Waterloo Institute for Nanotechnology, and the Graduate Studies and Postdoctoral Affairs at the University of Waterloo for the financial aid to complete my doctoral studies. I would like to also thank many tutors, especially Jane Russwarm, at the University of Waterloo Writing and Communication Centre, for assistance with various revisions of my writing.

Lastly, I sincerely wish to thank my family for their unconditional support and love in my life.

Table of Contents

List of Figures

List of Tables

List of Abbreviations

PDMS	Polydimethylsiloxane
LSCM	Laser scanning confocal microscopy
COF	Coefficient of friction
EHL	Elastohydrodynamic lubrication
DMA	Dynamic Mechanical Analyzer
SRM	Semi reflective mirror
GM	Galvanometric mirror
DM	Dichroic mirror
PMT	Photomultiplier tubes
PH	Size of pinhole
NA	Numerical aperture of the microscope objective
INA	Illumination numerical aperture

List of Symbols

Υ	Surface stress
$\gamma_s, \gamma_l, \gamma_{sl}$	solid-vapor, liquid-vapor, and solid-liquid interfacial tension
θ_1	Equilibrium contact angle
$\boldsymbol{\Upsilon_s}, \boldsymbol{\Upsilon_l}, \boldsymbol{\Upsilon_{sl}}$	solid-vapor, liquid- vapor, and solid-liquid interfacial stress tensor
$\mathbf{t_s}, \mathbf{t_l}, \mathbf{t_{sl}}$	solid-vapor, liquid- vapor, and solid-liquid interfacial tangent vector
E	Elasticity
γ	surface free energy
ϵ	Elastic strain
υ	Poisson’s ratio
$a, a_{F=0}$	Contact radius and contact radius at zero load
ε	Cutoff distance
d_x	Distance along the line of surface tension action
M	Molecular size
L_{ec}	Elastocapillary length
F, F_c, F_H, F_X	Preload, critical force, Hertzian preload, and lateral friction force
R_1, R_2	Curvatures of contact pairs
R^*	Reduced (or effective) curvature
E_1, E_2	Young’s modulus of contact pairs
E^*	Reduced (or effective) elasticity
ν_1, ν_2	Poisson’s ratio of contact pairs
w	Work of adhesion
$a_{Hertz}, a_{JKR}, a_{DMT}, a_{Schwarz}$	Contact radius of the Hertz, JKR, DMT, and Schwarz models
μ_T	Tabor’s dimensionless parameter
σ	Mean deviation of the asperity heights
D, D_{Hertz}	Indentation depth and Hertzian indentation depth
G, G', G''	Shear elasticity, shear storage modulus, and shear loss modulus
E', E''	Elastic storage modulus and elastic loss modulus
α	Empirical transition parameter
μ	Sliding friction coefficient
U, U_c	Sliding velocity and critical velocity
η	Liquid viscosity
Λ	Dimensionless film parameter
h_{min}	Minimum lubricant film thickness
R_i, R_O	Inner radius and outer radius
f_{sk}, f_k, f_s	Stiction spike, kinetic friction force, and static friction force
E', E''	Elastic storage modulus and elastic loss modulus
R_a, R_q	Average root mean square height and average surface roughness
λ	Wavelength of light

$I_r, \widetilde{I_r},$	Resultant raw light intensity and normalized intensity,
I_{min}, I_{max}	Minimum light intensity and maximum light intensity
V_{indent}	Volume of a glass sphere under the free surface of a soft substrate
V_{ridge}	Volume of a contact ridge
a_M, a_L	Experimental contact radius, contact radius on the free surface
L_c	Capillary length
δ	Contact ridge height
d	Submerged depth
ω	Frequency
τ_c	Viscoelastic time scale
n	Refractive index
H', H''	Electric field of light ray reflected off the bottom and top interfaces
dz	Size of optical slice
H_r	Resultant electric field
I', I''	Light intensity reflected off the bottom and top interfaces
φ	Phase difference
r_m	Radius of the mth interference ring (m: integer)
N	Number of peak points
f	Friction factor
h	Local gap distance
A	Apparent contact area
a_0	Apparent contact radius
H	Substrate film thickness
Re	Reynolds number
ρ	Density
ζ	Degree of shear deformation
L	Channel length
ΔP	Pressure drop
D_G	Outer diameter of soft wall channels
D_i	Inner diameter of soft wall channels
Q_0, Q_{rigid}	Volumetric flow rate and volumetric flow rate for rigid channels
P_{loss}	Pressure drop of the minor losses
$K_{L,i}$	Loss coefficient
P^*	Scaled pressure drop
k	Spring constant
θ^*	Finite contact angle (Contact angle of the hydrogel foot)
θ_m	Macroscopic contact angle (Contact angle of pure liquids)
R_0	Initial radius before deformation by contact

Chapter 1

Introduction

1.1 Motivation

In the early morning, a sip of a latte wakes us up. Applying lotions and creams helps our skin to be hydrated and healthy after washing our face. We head to work, having put on shoes with viscoelastic soles. When we look up emails and check the weather on our cell phones, we touch thermoplastic polyurethane (TPU) protective films, not the bare glass layer. Whether we know it or not, our daily lives are surrounded by soft materials. Those materials are typically distinguished from pure liquids and solids due to their intermediate mechanical properties between liquid and solid materials, creating a time-dependent strain or stress (*i.e., hysteresis*).

Our inspiration for the research in this thesis is focused on one subset of soft physical systems, soft viscoelastic polymers, which have typical elasticity of less than a few MPa. Such soft solids have been attracting great interest in various fields of study: artificial organs, bio 3D printing, wound-healing patches, moisture absorbents, drug delivery, anti-biofouling coatings, soft robots, *in-vitro* models, diagnostic chips, and food processing [1–8]. In addition, soft polymeric materials are ubiquitous in nature: mostly water-based materials [9,10]. Nature's soft materials with large liquid contents provide aqueous slippery surfaces in biology (*e.g.,* cartilaginous joints, ocular surfaces). Soft polymeric materials are composed of reticulated polymeric networks which deform to a less probable conformation under stress (*i.e.,* entropic origin). In contrast, ordinary crystalline solids change the interatomic distances under stress (*i.e.,* enthalpic origin). Here, the key players bringing the difference are 'Surface stress (Υ)' and 'Elasticity (E)', which relative importance is evaluated as the length scale, the elastocapillary length (Υ/E). Generally, at scales much larger than Υ/E, surface stresses are negligible. At scales smaller than Υ/E, the surface stresses overwhelm the elastic behavior, causing dramatic differences from classical mechanics designed for rigid solids. Soft viscoelastic polymers typically have an elastocapillary length near a few micrometers, while rigid solids have an elastocapillary length on an atomic scale, which makes it relatively easier to observe the capillary-driven behavior. This coupling effect of surface stress and elasticity opens a new era for interface dynamics in soft solids. Understanding the interface dynamics of soft polymers is critical to controlling and optimizing their adhesion, lubrication, and deformation, depending on specific applications. This is a truly multidisciplinary area of research combining physics, material science, chemistry, biophysics, pharmaceutical science, and tribology. Despite the huge potential and popularity of soft viscoelastic polymers, the fundamental dynamics of soft interfaces remain elusive. Over the last decade, a number of studies reported modified theories and experimental findings, but there are still many unanswered questions. This is mainly because of the materials' intrinsic complexity, as Pierre-Gilles de Gennes mentioned in his Nobel Lecture in Physics, 1991[11].

In this dissertation, the adhesion, lubrication, and wetting of soft solids in contact with solids, other soft polymers, and liquids in three systems: (i) sliding, (ii) equilibrated stationary, and (iii) confined flowing fluidic. We designed simplified experimental systems such as single spherical particles on soft surfaces and straight soft wall channels with flowing Newtonian fluids. This approach will eventually allow us to extrapolate our findings to practical physical applications. We investigated the relative roles of each key parameter, especially focusing on surface stress and viscoelasticity, based on a series of parameter studies. We comprehensively covered extreme limits of viscoelastic materials, near liquid (*i.e., wetting*) and solid phases (*i.e., adhesive contact*). Before going into each specific research in detail, we discuss the motivation behind each of the four research problems that are addressed in this thesis.

One of the most common surfaces of contact around us is a tribosystem. We studied the tribological behavior of sliding soft contact pairs, which may inspire one to design *artificial cartilage* and to understand *biological systems* such as *ocular tear films* and *mucosal surfaces*. Knowing the lubrication regime of the contact system is critical to understand how the applied stress is dissipated and wears contacting surfaces at different sliding speeds and preloads. Since soft viscoelastic polymers contain free liquids, which might work as a secondary lubricant, studying soft contact pairs with varying viscoelasticity is important beyond applying the classical theories developed for rigid tribopairs. Our study on stationary contact of soft polymers may inspire one to develop *soft robots* and *pressure-sensitive adhesive patches.* Soft robots might need to tolerate a wide range of external stress without plastic deformation while conforming to the counter surface structures [12]. Similarly, pressure-sensitive adhesive patches create strong physical adhesion upon contact with a counter surface without a chemical reaction. Our findings on the transient and steady-state deformation of soft materials might help engineer materials with enhancement in their durability. In addition, inert soft viscoelastic polymers might serve as qualitative models for more complex mesoscopic objects such as *biological tissues* due to their analogies of mechanical strength. Capillary interactions and viscoelastic behaviors of soft polymers might play a key role in understanding the self-organization of tissues (*e.g., embryotic morphogenesis, wound healing, cancer progression*) and developing *cell patterning* technologies for *artificial organs* [13]. Our findings on highly soft polymers' static deformation might provide critical insight into *tissue mechanics* [1,14–17]. In the form of fluidic channels, the scope of this thesis is extended: studying the contact behavior of soft materials in contact with flowing fluids. This may help *engineers* to develop *in-vitro vascular models* and *anti-biofouling coating of catheters*. The soft wall channels are widely utilized for drag reduction (*i.e.,* energy conservation), self-cleaning, and anti-fouling purposes in submarines and vessels [6,18–23]. Specific functions can be achieved by finely tuning the surface wettability, viscoelasticity, and system parameters (*e.g.,* flow rate, viscosity of fluids, and channel dimensions), which are investigated in this research.

1.2 Fundamentals of Wetting and Contact Adhesion of Soft Solids

In this section, the fundamental themes and relevant literature are reviewed to provide a context for the research problems presented in this thesis.

1.2.1 Partial Wetting on Soft Surfaces

A liquid drop atop a solid surface has a hemispherical cap shape when the droplet has a smaller size than the capillary length. At the three phases contact point, the contact angle, θ_1 is determined by the balance among cohesive and adhesive forces of the liquid, solid, and surrounding medium (typically, vapor), as described in the classical Young-Dupré equation: $\gamma_s = \gamma_l cos\theta_1 + \gamma_{sl}$ where γ_s , γ_l , and γ_{sl} are the interfacial tensions of solid (s)-vapor, liquid (l)-vapor, and solid-liquid (sl), respectively (Fig. 1.1(a)). Here, we find that only the force balances are described on the horizontal line. Neumann considered a different scenario that a liquid drop is resting on a liquid surface, assuming the two liquids are immiscible. In this case, the contact angle reaches the equilibrium state, creating significant underlying surface deformations (Fig. 1.1(b)). The equilibrium state can be described in vector (*i.e., Neumann's triangle law*): $\boldsymbol{\Upsilon}_{\boldsymbol{l}}\mathbf{t_l} + \boldsymbol{\Upsilon}_{\boldsymbol{s}}\mathbf{t_s} + \boldsymbol{\Upsilon}_{\boldsymbol{sl}}\mathbf{t_{sl}} = 0$ where $\boldsymbol{\Upsilon}_{\boldsymbol{l}}$, $\boldsymbol{\Upsilon}_{\boldsymbol{s}}$, and $\boldsymbol{\Upsilon}_{\boldsymbol{sl}}$ are the surface stress tensors at each interface, and $\mathbf{t_l}$, $\mathbf{t_s}$, and $\mathbf{t_{sl}}$ are the tangent vectors at each interface, as shown in Figure 1.1(c). Surface stress is the excess surface force per unit length. A liquid has isotropic surface stress (*i.e.,* surface tension) because molecules move from the bulk to the interface when creating new surfaces: $\boldsymbol{\Upsilon} = \boldsymbol{I}\gamma$. Therefore, the surface stress of liquids indicates the work required to create a new surface by cleaving (*i.e.*, the thermodynamic work). However, solids have an anisotropic surface stress because the solid molecules are not free to move and tend to preserve their original places. Hence, the surface stress depends on the surface free energy and its derivatives with strain: $\Upsilon = \gamma + d\gamma/d\epsilon$ where ϵ is the elastic strain parallel to the interface (*i.e., the Shuttleworth effect*) [24]. In the

Shuttleworth effect, $d\gamma/d\epsilon$ causes tangential elastic stress working below the direct contact line. $d\gamma/d\epsilon \sim 0$ is often assumed to make the research problem amenable to the incompressibility of materials (Poisson's ratio $\nu = 0.5$).

When a liquid droplet sits on a soft surface, the classical wetting theories, Young-Dupré and Neumann's triangle laws are not applicable because of the out-of-plane force ($O(\varepsilon)$) caused by the unbalanced vertical surface stress, $\gamma_l sin\theta_1$ where ε is a cutoff distance, typically a few nanometers (Fig. 1.1(c)). This force is negligible when $\gamma_l/E \ll a$ because the underlying surface is too stiff to deform by the surface stress, wherein a is the contact radius. However, when $\gamma_l/E \gg a$, $O(\varepsilon)$ pulls the soft surface upward at the contact line (*i.e., wetting ridge*) and pushes the soft surface down inside [25]. This rebalancing of interfacial energies might modify the contact angle and contact angle hysteresis of soft solids.

The wetting ridge was first found by A.I. Rusanov (1961) and G. Lester (1975) [26,27]. In 1987, the height of the wetting ridge was theoretically shown to be in the order of $\gamma_l[sin\theta(t)]/E$ where $\theta(t)$ is the apparent contact angle which was a function of spreading time [28,29]. Direct observation of the wetting ridge was first shown under scanning electron microscopy (SEM) by A. Carre *et al.* (Fig. 1.2(a)) [30]. The authors described the vertical displacement as $h(x) \approx (\gamma_l sin\theta_1/2\pi G)\ln(d_x/x)$ where G, d_x, and x are the shear elasticity, distance along the line of surface tension action, and distance from the triple contact line. This relation was applicable when $x > \varepsilon$ wherein the solid is linearly elastic. R. Pericet-G$\acute{a}$mara *et al.* showed the entire surface deformation profile of polydimethylsiloxane (PDMS) substrates in contact with a liquid droplet under laser scanning confocal microscopy (LSCM) [31]. Their research proved for the first time that a dimple underneath the liquid droplet was formed due to the Laplace pressure. They further studied the role of substrate thickness on dimple deformation (Fig. 1.2(b)) [32]. They found that the thinner, soft film caused the smaller dimple deformation due to the rigid support layer underneath the soft film. L. Limat described the whole profile of the cusp as the logarithmic profile based on the equilibrium of surface energies [33]. E.R. Jerison and R.W. Style predicted the cusp profile based on symmetric surface stresses (Fig.

1.2(c)) [34,35]. Many experimental works reported that millimeter-sized liquid droplets atop soft substrates have a larger contact angle as the soft substrates become softer [36–39]. L.A. Lubbers *et al.* suggested that the equilibrium state of a liquid drop on a soft solid was governed by three length scales, the droplet radius (R), the molecular size (M), and the elastocapillary length (L_{ec}). They showed that the apparent contact angle changes when $L_{ec} \gg R$ and the microscopic contact angle differs from Young's Law when $L_{ec} \gg M$. S. Park *et al*. revealed that the cusp of the wetting ridge was asymmetric under X-ray microscopy, unlike the findings of early studies (Fig. 1.2(d)) [40]. In addition to the surface profile deformation, the compositional change in the wetting ridge, especially near the cups, was found, created by the vertical surface stress by Z. Cai *et al.* (Fig. 1.2(e)) [41].

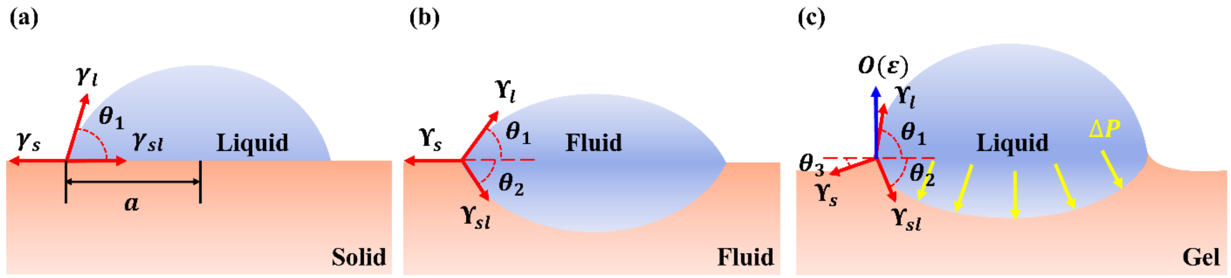

Figure 1.1 Schematics of a liquid drop deposited on different surfaces: (a) solid, **(b)** fluid, and **(c)** gel.

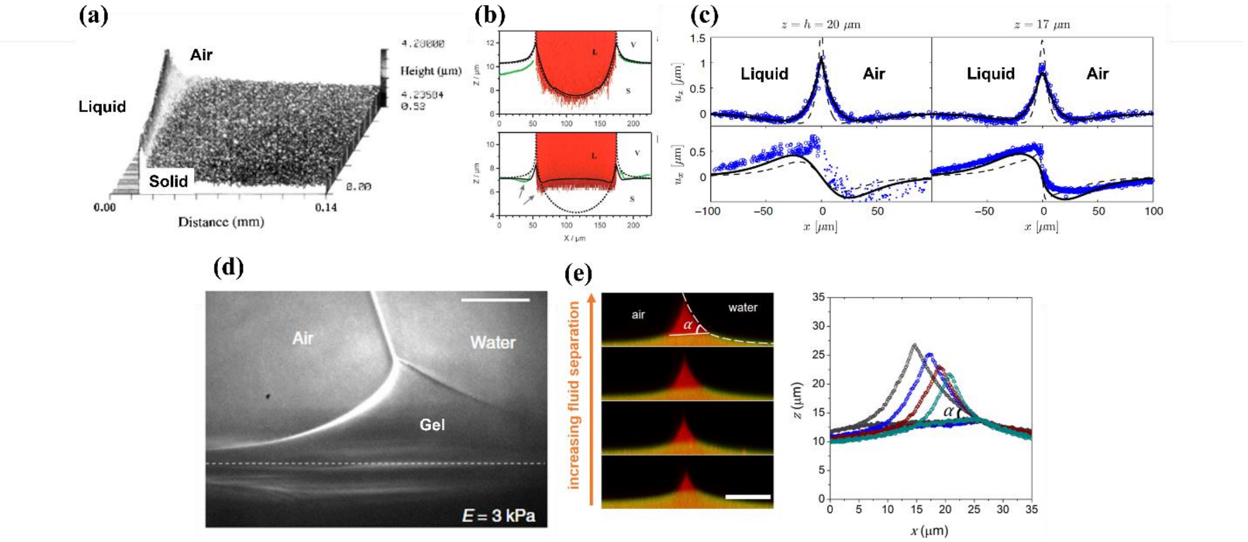

Figure 1.2 Wetting profiles of soft solids underneath a liquid droplet. (a) The 3D wetting ridge profile obtained using scanning interferometric microscopy (Adapted from ref.[30]). Copyright 1996 Springer Nature. **(b)** The LSCM images of a liquid drop on soft substrates with two different thickness of 104 μm (Top) and 8.5 μm (Bottom). The black dashed line is drawn based on the model of Rusanov and the solid black line is based on the simulation (Adapted from ref.[32]). Copyright 2009 Royal Society. **(c)** The measured surface deformation (blue circles) of u_z (perpendicular to the interface) and u_x (parallel to the interface) at the surface (left) and just below the surface (right). The dashed lines are for a finite-thickness elastic slab, and the solid lines are for a finite-thickness elastic slab with surface tension (Adapted from ref.[34]). Copyright 2011 American Physical Society. **(d)** X-ray image of the wetting ridge of soft solids underneath a water droplet (Adapted from ref.[40]). Copyright 2014 Springer Nature. **(e)** Confocal images of wetting ridge on soft solids with varying swelling ratio (left) and corresponding profiles (right) (Adapted from ref.[41]). Copyright 2021 Springer Nature.

1.2.2 Adhesive Contact on Soft Surfaces

What happens when two elastic solids are in contact? The simplest but strongest answer was developed by Heinrich Hertz during the Christmas vacation in 1880 [42]. To describe the real contact system (Fig. 1.3 and Fig. 1.4 (a)), the Hertzian contact radius was derived as a function of radii of two curvatures (R_1 and R_2), Young's moduli (E_1 and E_2), Poisson's ratios (v_1 and v_2), and the preload (F) (Fig. 1.4(b)): $a_{Hertz} = \left(\frac{3FR^*}{4E^*}\right)^{\frac{1}{3}}$ where $R^* = R_1R_2/(R_1 + R_2)$ and $1/E^* = [(1-(v_1)^2)/E_1 + (1-(v_2)^2/E_2]$. After about 100 years, in 1971, K.L. Johnson *et al.* introduced the modified adhesive Hertz theory (*i.e., the JKR theory*) [43]. The JKR theory describes the adhering two objects, driven by adhesion energy and opposed by elastic energy: $a_{JKR} = [3R^*/4E^*(F + 3\pi wR^* + \sqrt{6\pi wR^*F + (3\pi wR^*)^2})]^{1/3}$ where the work of adhesion, $w = \gamma_1 + \gamma_2 - \gamma_1\gamma_2$. Here, the Hertz theory can be recovered for $W = 0$. The JKR assumes no force outside of the direct contact and considers short-range attractive adhesion by a delta function (Fig. 1.4(c)). The JKR theory was developed for macroscopic contact systems, but it has also been widely used for microscopic systems and rough surfaces at the micro-scale [44]. A few years later, in 1975, another modified Hertz theory was developed by B.V. Derjaguin *et al*. assuming no adhesive force within the direct contact zone but considering long-range attractive force outside the direct contact area (*i.e., the DMT theory*) (Fig. 1.4(d)) [45]: $a_{DMT} = [3R^*/4E^*(F + 2\pi wR^*)]^{1/3}$. One year later, D. Tabor reconciled the two different theories by introducing a dimensionless parameter: $\mu_T = \left(\frac{R^*w^2}{E^{*2}\sigma^3}\right)^{\frac{1}{3}}$ where σ is the mean deviation of the asperity heights. The parameter expresses a balance between the adhesive force and elastic force. For contact systems with $\mu_T \geq 4.6$, the short-range attractive force, JKR theory predominates. For contact systems with $\mu_T \leq 0.1$, the long-range attractive force, DMT theory predominates [46]. In other words, for soft surfaces, large radius, and high adhesion energy, JKR model is more suitable, while for hard surfaces, small radius, and low adhesion energy, DMT theory is more suitable. The radius at the transition between the JKR and DMT models ranges from a few nanometers for E^* in GPa and a few micrometers for E^* in the order of

100 GPa. Later, the intermediate regime was filled by the Maugis-Dugdale(M-D)' general solution in 1991 (Fig. 1.4(e)). The M-D model assumes constant adhesion forces at the interfaces (the direct contact zone and outer extend of the attractive force interactions) [47]. In 1999, R.W. Carpick, D. F. Ogletree, and M. Salmeron developed an empirical equation that was a simpler general equation than the analytical solutions given in the M-D model (*i.e., the COS model*) [48]. In 2003, U.D. Schwarz validated the COS model with giving a physical explanation (Fig. 1.4(f)) [49]. As a result, the two different JKR and DMT regimes are smoothly connected with a single equation containing a dimensionless empirical transition parameter α: for the JKT theory, $\alpha = 1$ and for the DMT theory, $\alpha = 0$: $a_{Schwarz} = a_{F=0(\alpha)}\left[\left(\alpha + \sqrt{(1 - F/F_{c(\alpha)}}\right)/(1+\alpha)\right]^{2/3}$ where $a_{F=0(\alpha)}$ and $F_{c(\alpha)}$ are the contact radius at zero load and critical force, *i.e.,* the force required to separate two contacting bodies.

As the technologies developed, the direct observation of the contact zone became to be possible to validate the developed theories. In 1988, the depart of soft contact systems from the classical theories was observed under SEM by D.S. Rimai *et al.* (Fig. 1.5(a)) [50,51]. In the presence of capillary condensation, A. Fogden *et al.* proposed the modified Hertz theory accounting for the Laplace pressure [52]. R.W. Style *et al.* provided the modified JKR theory, and the applicable range of the theory was determined by the elastocapillary length (Fig. 1.5(b)) [44]. K.E. Jensen *et al.* visualized the phase-separated liquids out of the elastic network and described the force balanced at the four-phase contact zone (Fig. 1.5(c)) [53]. Also, the authors found that at the contact line, the curvature was reciprocal to the elastocapillary length. J.T. Pham provided the modified JKR theory incorporating the capillary pressure and the energy penalty by surface stretching [54]. A. Chakrabarti *et al.* flipped the sites of typical contact pairs, rigid-on-soft contact to soft-on-rigid contact using hydrogel spheres and fitted the experimental results using the simplified M-D model (Fig. 1.5(d)) [55]. When a rigid particle is atop a soft substrate, the contact system is analogous to a rigid particle floating on the fluid interface. H. Liang *et al.* simulated a rigid-on-soft contact system and found the higher rigidity of materials moved the direction of the elastic force to the vertical direction, and the bigger particles strengthened the elastic force [56]. H. Liang *et al.* showed that the surface stress presented a strain dependence when the substrate deformation reaches a length the same as that of stretched network strand without bond deformation [57]. J. D. Glover *et al.* proposed the modified Hertz theory, which balanced the capillary force of the free oil layer and particles' adhesion and surface tension forces (Fig. 1.5(e)) [58]. Z. Cai *et al.* described the contact ridge and phase-separated liquids based on the interfacial energy (the elastic energy and mixing energy (*i.e.*, *Flory-Huggins energy*)) [41]. This present thesis was performed to fill the knowledge gaps unresolved in the above-mentioned early studies. Detailed limitations of early works and methods are discussed in each chapter.

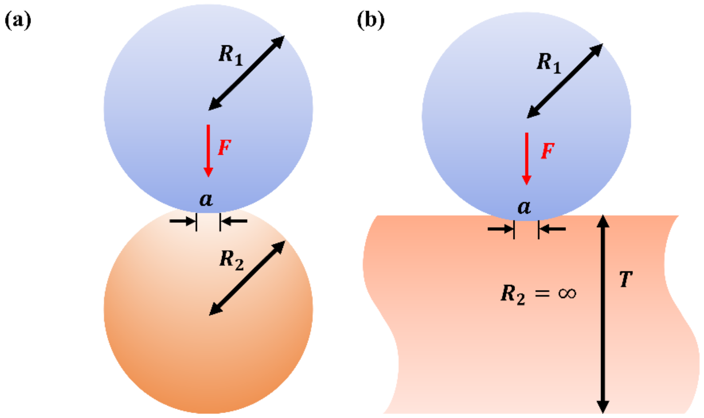

Figure 1.3 Schematic of representative contact of elastic solids with the contact radius (a) under the preload (F). (a) Solid sphere-on-solid sphere with different radii, R_1 and R_2, respectively. **(b)** Solid sphere-on-solid semi-infinite substrate. The underlying substrate has a thickness (T) larger than the radius (R_1).

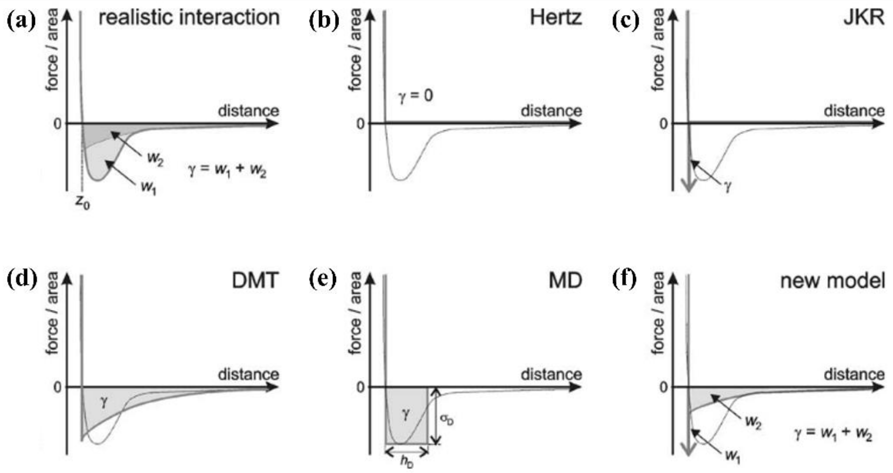

Figure 1.4 The interaction force in elastic solid contact. (a) Realistic interaction. **(b)** Hertz theory. **(c)** the Johnson–Kendall–Roberts (JKR) theory. **(d)** The DMT theory. **(e)** M-D model. **(f)** Schwarz model. (Adapted from ref. [49]). Copyright 2003 Elsevier.

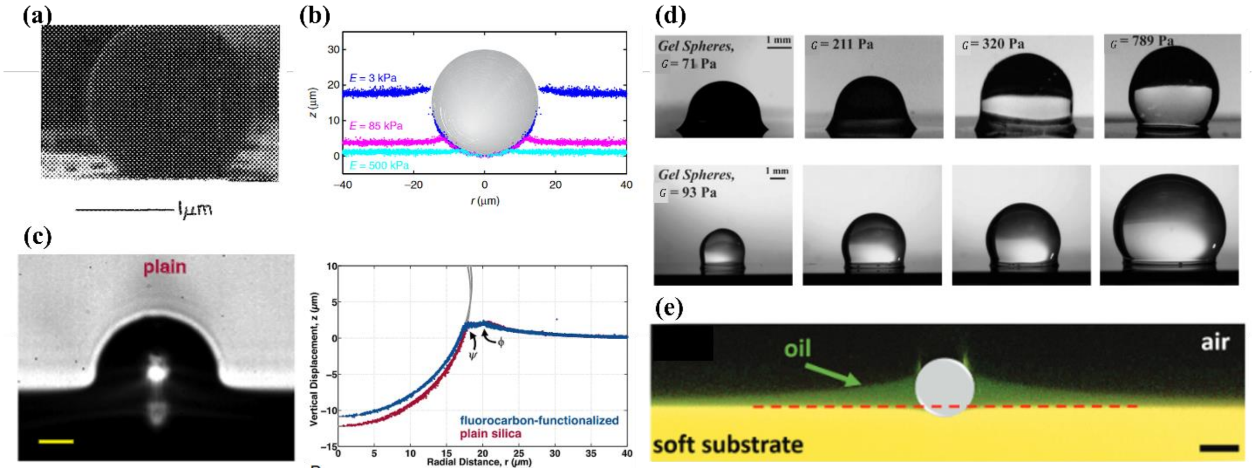

Figure 1.5 Soft contact in the equilibrium state. (a) An SEM Image of a polystyrene particle on a soft polyurethane substrate. The particle embed into the soft surface (Adapted from ref.[50]). Copyright 1989 AIP Publishing. **(b)** Surface indentation profiles of soft solids under a glass sphere. Surface stiffness is 3 kPa (blue), 85 kPa (magenta), and 500 kPa (cyan) (Adapted from ref.[44]). Copyright 2013 Springer Nature. **(c)** A side view of adhesive contact of a plain silica particle on a soft gel substrate (left) and the extracted soft surface profile under fluorocarbon-functionalized (blue) and plain silica particles (magenta) (Adapted from ref.[53]). Copyright 2015 National Academy of Sciences. **(d)** Equilibrium profiles of hydrogel beads with

different shear moduli (G) on untreated silicon wafers (top) and hydrogel beads with varying radii on silicon wafers (bottom) (Adapted from ref.[55]). Copyright 2018 American Chemical Society. **(e)** A fluorescent image of a glass particle on a dyed soft substrate. The polymeric network is dyed in yellow, and the oil phase is dyed in green fluorescent dye (Adapted from ref.[58]) Copyright 2020 Royal Society.

1.3 Dissertation Synopsis

In this section, a brief outline of each chapter is provided in this thesis. This dissertation researches the soft solids in different contact systems (in contact with sliding solids, static solids and gels, and flowing fluids) to reveal the root causes of soft solids' contact behavior (*e.g.,* surface deformation, resultant stress) and provide information in the design of practical technologies of using soft solids.

Chapter 2 presents detailed experimental results of the sliding friction between purely viscoelastic tribopairs. Particular attention has been paid to the interplay between viscoelastic hysteresis and the lubricating effect of the soft tribopairs at varying preloads and sliding speeds.

Chapter 3 shows the time-dependent surface evolution of thin gel films under interference microscopy. We especially focus on soft contact systems wherein the rigorous assumptions of the existing contact theories are not followed; the finite-size of underlying gel films and preload of macro-size glass spheres predominantly affect the surface deformation. Two distinct stages of surface deformation were shown until it was equilibrated. Predominant factors were discussed in each stage.

Chapter 4 investigate more dynamic systems involving soft solid in the form of soft wall channels under flowing Newtonian fluids. In departure from the classical Hagen-Poiseuille equation, here, the lubricating effect of residual free oligomers in the soft walls was exhibited by the reduced pressure drop of flowing fluids. Subtle diffusion of water into the soft walls was also found to possibly reduce the resistance at the interface between flowing fluids and soft walls.

In chapter 5, wetting and adhesive contact regimes were connected by modulating the viscoelasticity of two immiscible gels from a few Pa to MPa. Through a series of parameter studies, a scaling law was suggested between the contact radius and the dimensionless parameter, consisting of the work of adhesion, elasticities, and initial characteristic length scale of the two gels.

Finally, chapter 6 concludes this thesis by summarizing the highlights of each chapter and providing general suggestions on future directions.

Chapter 2

Viscoelastic Tribopairs in Dry and Lubricated Sliding Friction[†]

Soft contacts present different tribological responses compared to stiff materials, especially when soft materials exhibit viscoelastic behavior, as viscoelastic materials have intermediate mechanical properties between viscous liquids and elastic solids. In this work, we investigated the influence of viscoelasticity of soft materials on sliding friction in dry and lubricated conditions. To achieve this, soft tribopairs with varying viscoelasticity were obtained by tuning the weight ratios of polydimethylsiloxane (PDMS) base and curing agent. The real-time friction force and preload were observed over multiple conditions, with systematic control of lubricant viscosity, preload, and sliding velocity. Tribopairs with a higher proportion of viscous character had more oscillations in the friction force. They also presented a higher friction coefficient due to the increased contribution of viscoelastic hysteresis losses on friction. Through regression analysis, the models of the friction coefficient were found, which are in good agreement with experimental results. From the models, we found that in both dry and lubricated conditions, viscoelasticity of tribopairs, indicated as the loss modulus or loss tangent, plays a key role in determining the friction coefficient. This influence is particularly significant for dry contacts due to the direct interactions between surfaces of tribopairs. This study provides empirical proof and a focused analysis on the role of viscoelasticity in tribological contacts.

[†] This chapter is reproduced from A-Reum K. Aleksander C., Sushanta K. M., and Boxin Z., "Viscoelastic Tribopairs in Dry and Lubricated Sliding Friction." *Soft Matter*, 2020, vol. 16 (32). 7447-7457.

2.1 Introduction

Friction and lubrication between soft contacts, where one or both tribopairs have a low elastic modulus (typically with a Young's modulus around or below 100 MPa[59]), hold great importance in various fields. In biological systems, soft contacts can be found in animal skin,[60,61] joints and eyes,[62,63] and tongue-palate contacts during oral processing of foods[64]. In industrial systems, soft contacts can be found in rubber sealings, tires, and wiper blades[65,66]. Soft materials in contact with lubricants (either directly or with lubricants in between two soft materials acting as tribopairs) have also found broad use in applications such as artificial joints,[67,68] implantable medical devices,[69] and soft robots.[70,71]

Soft contacts display different tribological behavior from rigid contacts (*i.e.*, contact between hard solids), presenting a high friction coefficient (the ratio of preload (F) in the normal direction to friction force ($\mathrm{F_X}$) along the line of motion, x) due to viscoelastic deformation hysteresis[65,72]. Unlike conventional laws for the friction of rigid contacts, friction for soft contacts is dependent on both sliding speed and apparent contact area. Even though the distinctive features of soft contacts are known, the tribological behavior of soft materials remains partially undiscovered, with the effects of some parameters unexplored (such as viscoelastic behavior of tribopairs,[61] thickness of substrates,[73] etc.), and only a limited range of elasticities of soft materials have been experimentally tested.

In dry contact (without a lubricating liquid film), friction forces are ascribed to two main sources: 1) breaking of interfacial adhesive bonds (*i.e.*, interfacial friction) and 2) deforming the subsurface of the tribopairs under applied load (*i.e.*, internal friction)[74–76]. The internal (cohesive) friction is attributed to viscoelastic hysteresis losses; these deformation losses originate within the bulk of the soft materials under stress where the friction loss (*i.e.*, the absorbed energy) is dissipated as heat. For soft materials, both friction forces are crucial whereas for stiff materials, internal friction is negligible because of their high stiffness[74,77,78]. For lubricated contact, additional friction forces originate from shear stresses arising from the lubricant film between the tribopairs. It has been widely accepted that several different lubrication regimes exist: boundary lubrication, mixed lubrication, and hydrodynamic lubrication (Fig. 2.1). These regimes are described by the Stribeck curve, which is a plot of the friction coefficient (in vertical axis) against the viscous shear intensity (reduced velocity), $U\eta$ with units, $\mathrm{N \cdot m^{-1}}$ where U is the sliding velocity and η is the lubricant viscosity.[66,74,79] For sliding friction, this reduced velocity can be rewritten in a nondimensional form, the Sommerfeld number:[74]

$$\text{Sommerfeld number} = \frac{\eta U R}{F} \tag{2.1}$$

where R is the radius of the probe and F is the normal preload. The Stribeck curve was originally designed for lubricated hard contacts, but since an alternative model has not yet been developed, it has also been applied in the study of lubricated soft contacts. To take into account the influence of elasticity (E) of the substrate, we use the elastohydrodynamic (EHD) number instead of the Sommerfeld number,[64,74,80] which is defined as:

$$\text{EHD number} = \frac{\eta U E^{1/3} R^{5/3}}{F^{4/3}} \tag{2.2}$$

In addition to the three lubrication regimes in the conventional Stribeck curve, soft materials also demonstrate the iso-viscous elastohydrodynamic lubrication (EHL) regime. In this regime, hydrodynamic forces within the lubricant film between the tribopairs generate the friction force without direct surface interactions. The contact pressure is sufficiently high to deform compliant opposing bodies, but insufficient to change the lubricant viscosity, since it is lower than the pressure in hard contacts (which is why this regime is also called ‘the iso-viscous EHL’). The lubrication regime for a tribosystem can be determined by calculating the dimensionless film parameter, Λ, which is given as:

$$\Lambda = \frac{h_{min}}{((\sigma_1)^2 + (\sigma_2)^2)^{1/2}} \tag{2.3}$$

where h_{min}, is the minimum film thickness, and σ_1 and σ_2 are the surface roughness of the probe and the substrate, respectively[81,82].

In soft contacts, some parameters, such as the lubricant viscosity, sliding velocity, and preload, have already been explored. For instance, J. de Vicente *et al.*[83] studied lubricated contacts between steel balls and flat elastomer discs, focusing on the influence of lubricant viscosity and entrainment speed of tribopairs with a reduced elasticity of 10.9 MPa. They performed tests at a constant preload of 3.0 N. Their work addressed the different origins of friction (sliding and rolling friction) for lubricated soft contacts. J. H. H. A. Bongaerts *et al.*[81] investigated the role of surface characteristics (*e.g.,* hydrophilicity and roughness) on lubricated soft contacts at a fixed preload of 1.3 N. They tested polydimethylsiloxane (PDMS) spheres and PDMS discs, each with an elasticity of 2.4 MPa. They found that neither surface hydrophilicity nor surface roughness affected the friction coefficient in the EHL regime. For their experiments, they suggested an empirical equation for the friction coefficient in the Stribeck curve, which does not contain any direct terms for the mechanical properties of tribopairs. The influence of the elasticity of tribopairs on friction was studied by C. Myant *et al.*[65] Friction forces were measured between a steel ball and different substrates at preloads of 0.5 – 5 N; substrates used were PDMS, low-density polyethylene (LDPE), and polycarbonate (PC) with elasticities of 0.005, 0.227, and 2.38 GPa, respectively. They found that in the boundary and mixed lubrication regimes (*i.e.*, the overlap of the EHL and boundary lubrication), the friction coefficient decreased with increasing preload because the contact area was more dependent on elastic conformity than on plastic deformation. Their experimental results had good agreement with the regression relations of the friction coefficient fitted with the loss tangent at each loading frequency. However, the study was limited to higher values of tested elasticities (0.005 – 2.38 GPa). The same research group[84] used a different technique to investigate soft contacts, focusing on lubricant film thickness between an elastomer (with an elasticity of 2.8 MPa) and plain glass discs. A wide range of preloads from 0.001 – 1 N was tested, and the corresponding film thicknesses were measured by an optical interferometric technique. To study the effect of loading angles on soft substrates, T. Yamaguchi *et al.*[85] tested tribopairs with a complex shear elasticity of 118 kPa. The studied modulus was considerably lower than those of previous studies, but was the only modulus examined. N. Selway *et al.*[74] performed further intensive analysis on the role of lubricant viscosity and wettability using tribopairs of polytetrafluoroethylene (PTFE) balls-PDMS discs and PDMS balls-PDMS discs. They reported that the conventional model is limited in its ability to interpret tribological results when considering indirect viscosity effects, such as entrapment of lubricants among asperities of tribopairs.

In terms of rheological modeling, scaling laws were used to study the influence of viscoelasticity on the lubricated contact, but the studied contact area was confined to a cylinder-on-flat geometry[78,86]. In the case of ball-on-flat contacts, the regression relation of the lubricant film thickness for both hard and soft tribopairs was derived in the EHL regime, but regression analysis was not used to model the friction coefficient [87,88].

In summary, even though lubricated soft contacts have been studied, a wider range of elastic moduli, especially at the lower end (where viscoelasticities of the tribopairs are more critical for the contact surfaces), would better elucidate the behavior of soft tribopairs. Additionally, to the best of our knowledge, to date, no experimental study has reported the influence of the viscoelasticity of tribopairs on the friction coefficient in non-conformal contact (circular, also referred to as ball-on-flat). This is important because many soft materials demonstrate viscoelastic behavior, which could play an important role in soft tribology. However, the nature of this role has not yet been fully examined. Moreover, due to the lack of experimental work and analysis, soft contacts have been studied based on a theory originally designed for hard contacts[74,89].

This paper aims to examine the role of viscoelastic properties of tribopairs on friction, as well as to suggest experimental models to understand the complex behavior of compliant dry/lubricated contacts under various conditions. To accomplish this, we investigated the non-conformal sliding friction of PDMS-PDMS contact, wherein the viscoelasticity of PDMS substrates was modified and studies were performed for both dry (without any lubricating film – the tribopairs are exposed to ambient air) and lubricated contact. The friction force was measured as a function of several parameters (sliding velocity, lubricant viscosity, and preload). Each mode of friction traces and the conditions for stick-slip sliding were investigated through observing each friction trace. We then performed regression analysis to identify the relationships between the friction coefficient and the parameters. The regression results indicated that the loss modulus is primarily responsible for determining the friction force of soft tribopairs. The lubrication regime of the tribosystem was analyzed by fitting the friction coefficient against the EHD number.

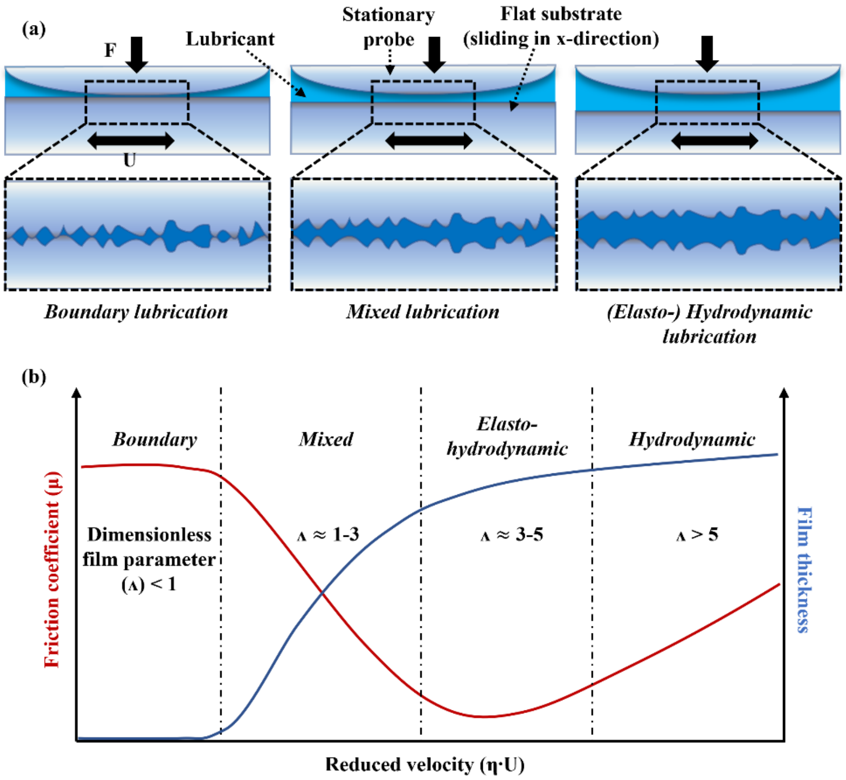

Figure 2.1 Different lubrication regime. (a) The schematic view of a typical tribosystem within each lubrication regime. **(b)** The Stribeck curve: the plot of the friction coefficient (μ) against the reduced velocity ($\eta \cdot U$) (or other nondimensional parameters). Film thickness is plotted in secondary y-axis. Each lubrication regime can be divided by the dimensionless film parameter (Λ).

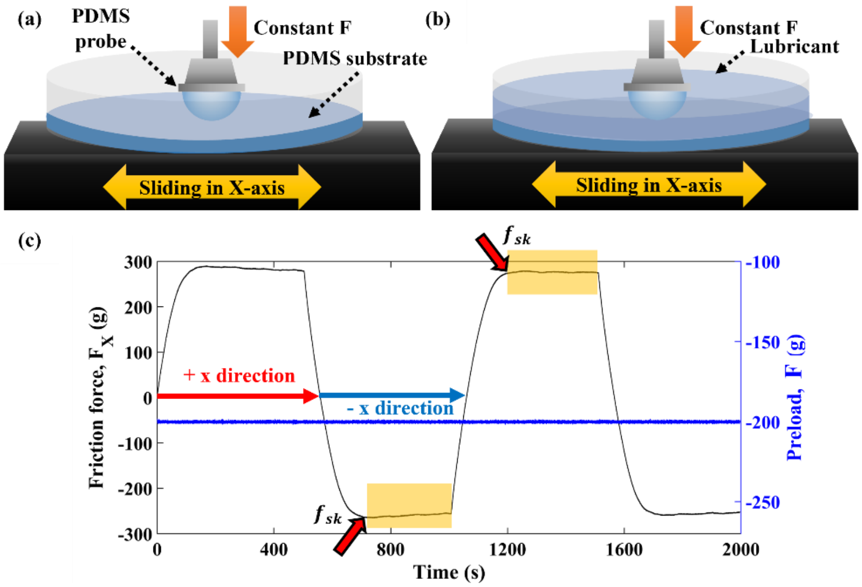

Figure 2.2 Sliding friction test. Schematic of the sliding friction test **(a)** in dry and **(b)** lubricated conditions at a constant preload (F) and a constant sliding velocity (U). Under the stationary PDMS probe, the bottom substrate travels laterally forward (+ x direction) and backward (- x direction), and the real-time friction force (F_X) and the preload (F) are measured during testing. For lubricated tests, a sufficient amount of lubricants was poured to immerse the PDMS probe with the depth of ~ 6.5 mm. **(c)** Representative cyclic friction traces between a PDMS probe-a PDMS 30:1 substrate at a preload of 1.962 N and a sliding velocity of 0.01 mm/s in dry condition. After the negligible initial peak of F_X (f_{sk}) (noted by a red arrow), the values of F_X were averaged. F_X denotes the friction force in the lateral travel direction. This region is called steady-state sliding (yellow coloured region).

2.2 Experimental

2.2.1 Preparation of Tribopairs

Tribopairs were fabricated using PDMS (Sylgard 184 elastomer kit, Dow Corning). PDMS has often been tested as one or both tribopairs in previous studies because of its easy fabrication process,[90–92] well-characterized material properties,[93,94] and broad applications (*e.g., in-vitro* diagnostic devices,[95–97] anti-biofouling coatings[6]). Additionally, its viscoelastic properties could be readily varied. PDMS prepolymer was prepared by mixing base and curing agent at each weight ratio using a planetary mixer (ARE-310, Thinky Corporation) for 20 minutes. PDMS 10:1 was cast in molds to prepare a PDMS hemispherical probe ($\mathrm{R_a} = 324$ nm) with a radius of ~ 2.9 mm following the fabrication method established by Zhang *et al.*[98] To explore the influence of viscoelasticity on friction, the flat bottom substrates, with a thickness of 2 mm, were fabricated with PDMS weight ratios of 10:1, 20:1, 30:1 and 40:1 ($\sigma_2 = 78$, 76.5, 78, and 78.33 nm, respectively). The upper limit of the weight ratio of PDMS base to curing agent was determined by the highest ratio in cured PDMS that was sufficient to maintain its original shape after repetitive sliding cycles. The prepolymer mixture was cured in a petri dish for 19 hours at 80 °C. Glass slides were also tested as bottom substrates replacing PDMS substrates in the petri dish. This configuration enabled us to verify the stability of our friction measurements and compare our results with those available in the literature for soft-hard tribosystem (See Appendix Fig. A.2.1). PDMS tribopairs were sufficiently rinsed with ethanol and ultra-purified water, then dried with nitrogen before use. Glass slides were cleaned ultrasonically with isopropanol and ultra-purified water successively, then dried with nitrogen.

Deionized (DI) water and glycerol (EMD Millipore Corporation) were utilized as lubricants because of their different viscosities and Newtonian behavior. Due to its hygroscopic nature, glycerol was exposed to ambient air for a day before testing. Tribopairs were fully immersed in the lubricants for at least 24 hours before testing. For lubricated sliding contacts, water or glycerol lubricant was poured into a petri dish containing the PDMS substrates, to a depth of ~ 6.5 mm, which was thicker than the radius of the probe (~2.9 mm) to ensure it was fully submerged during testing.

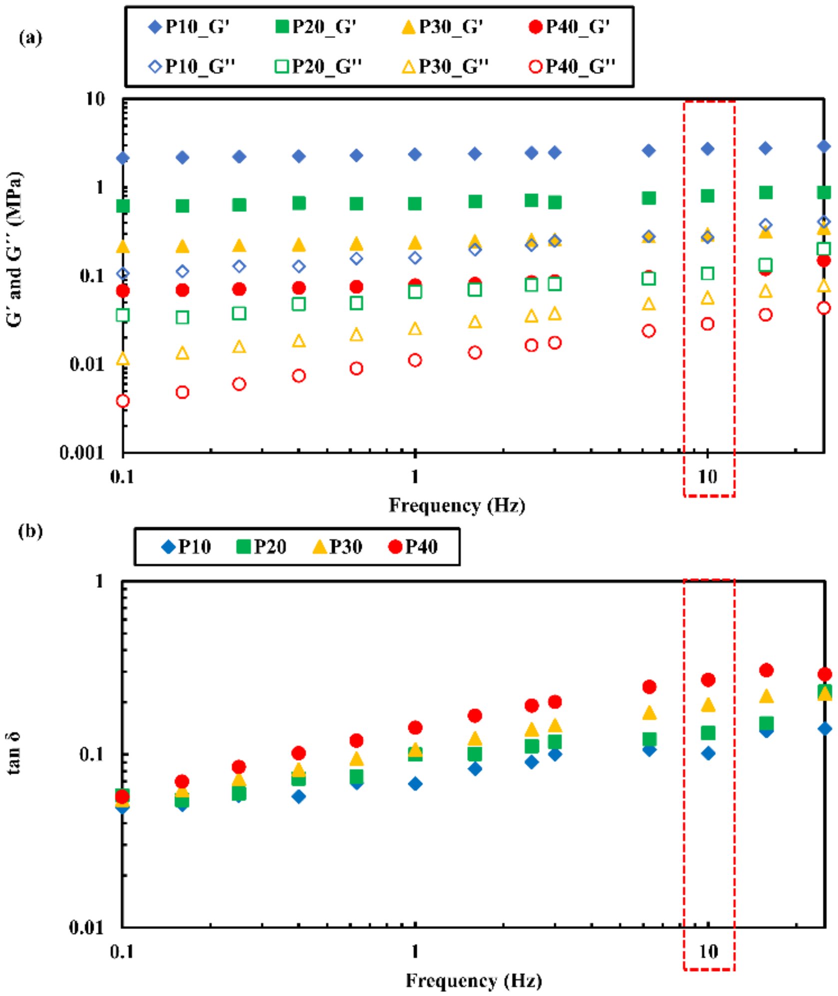

Figure. 2.3 Measured viscoelastic properties of PDMS: (a) the shear storage (G'), the shear loss modulus (G''), **(b)** the loss tangent (tan δ) obtained from the DMA over the frequency of 0.1 – 30 Hz. The values of G' and tan δ at 10 Hz have been marked with dashed red boxes, which are further used in the regression analysis, and the corresponding elastic storage modulus (E') was calculated using Eq. (2.4).

2.2.2 Measurement of Viscoelasticity of Tribopairs

Storage modulus (G'), loss modulus (G''), and loss tangent ($tan\delta$) were measured by a TA Q800 Dynamic Mechanical Analyzer (DMA, TA instruments) at 22 °C. PDMS samples were cut into rectangular shapes with dimensions $40\ \mathrm{mm}\ (\mathrm{L}) \times 10\ \mathrm{mm}\ (\mathrm{W}) \times 2\ \mathrm{mm}\ (\mathrm{T})$. The analysis was carried out using multi-frequency-strain mode at 0.1 – 30 Hz.[99] A 0.01 N preload was applied to the sample before testing. The storage (E') and loss modulus (E'') were calculated based on the measured values of G', G'', and $tan\delta$, using the following relationships:

$$E' = 2G'(1+\nu) \tag{2.4}$$

$$\frac{E''}{E'} = tan\delta \tag{2.5}$$

where ν is the Poisson ratio and δ is the phase angle.[100] The Poisson ratio of PDMS has different values in the literature, ranging from 0.39 – 0.48[93,101,102] and the specific Poisson ratio of PDMS from 10:1 to 40:1 was not available. Therefore, we employed an average value of 0.44 for all PDMS tribopairs. Here, the storage modulus can be considered to have the same value as Young's modulus for tensile tests. This assumption is reasonable because the applied preload was small when measuring the storage modulus, and Young's modulus is often calculated for small deformation, typically at a 0.2% offset.

2.2.3 Measurement of Friction

Sliding friction studies of dry and lubricated contacts were carried out on a universal macro-tribometer (UMT-2MT, Center for Tribology, Inc.).[98] A petri dish with a cured PDMS substrate (Figs. 2.2 (a) and (b)) was attached to the bottom plate of the UMT with double-sided adhesive tape. Under constant preload (W = 0.245, 0.981, and 1.962 N, which are 25, 100, and 200g, respectively), the bottom substrate traveled laterally forward ($+\ x$-direction) and backward ($-\ x$-direction) against the stationary PDMS probe at constant velocity (U = 0.005, 0.01, 0.05 and 0.1 mm/s). The minimum preload, 0.245 N, was selected because at preloads < 0.245 N, a significant amount of scatter was observed. The maximum preload, 1.962 N, was the maximum preload that did not break the PDMS hemispherical probe. The real-time friction force (F_X) and real-time preload (F) exerted on the probe were measured with a frequency of 200 Hz using a two-dimensional force sensor (~ 10 N) at 23 °C. Even though a constant preload was set to be applied initially to the tribosystem, due to viscoelastic deformation of tribopairs and interfacial adhesion between the contact surfaces, small deviations (< 0.5 % for steady-state sliding) from the initial preload were present. Therefore, the friction coefficient was calculated using the measured real-time friction force divided by the measured real-time preload. New PDMS substrates were used for each test case. Each experimental condition was repeated more than three times. Error bars were obtained from each value of the friction coefficient or the friction force. The average friction force was calculated in the steady-state sliding (the yellow region in Fig. 2.2(c)), which occurred after the initial peak of the friction force (the stiction spike, f_{sk}).[67,103]

2.3 Results and Discussion

Dry and lubricated friction forces of soft contacts were measured using the UMT under constant preloads at four different sliding velocities. Preloads higher than 1.962 N broke the PDMS probe due to the high resistance and interfacial adhesion with the contact surface, and the friction traces were unstable. Therefore, preloads of 1.962 N and below were studied. From here on, the PDMS weight ratios of 10:1, 20:1, 30:1 and 40:1 are labelled as P10, P20, P30, and P40, respectively.

2.3.1. Viscoelasticity of Tribopairs

Both the modulus and loss tangent increased until the frequency reached 10 Hz, then remained nearly constant at higher frequencies (Fig. 2.3). Therefore, the storage modulus and loss tangent measured at 10 Hz were used for overall regression analysis and the calculation of the elastic modulus. The elastic storage modulus of PDMS substrates was obtained using Eq. (2.4) (with ν = 0.44): for P10, E' = 7.805 MPa, for P20, E' = 2.306 MPa, for P30, E' = 0.846 MPa, and for P40, E' = 0.305 MPa. Due to the small amount of curing agent, P40 had the lowest storage and loss modulus, and hence the lowest stiffness. However, P40 has the highest loss tangent, meaning the highest ratio of energy dissipated to energy stored.

2.3.2 Characterization of Sliding Friction Traces: Smooth Sliding vs. Stick-slip

Different modes of friction traces are provided in Appendix (see Fig. A.2.2). During steady-state sliding, three different friction modes were observed: smooth sliding, irregular stick-slip sliding, and stick-slip sliding. Oscillations of the friction force and their behavior determine the corresponding mode of each tribosystem. The friction force is resolved into three different forces: the stiction spike (f_{st}), the kinetic friction force (f_k), and the static friction force (f_s). The stiction spike is the force that must be overcome before sliding begins. This force could be higher or lower than the static and kinetic friction force. The static friction force and kinetic friction force are the maxima and minima of the friction trace, respectively. In smooth sliding, both forces are equal ($f_s = f_k$) (Figs. A.2.2(a) and (d)). When the friction force oscillates between the static and kinetic friction forces with an irregular amplitude and frequency, the mode is irregular stick-slip friction (I s-s) (Figs. A.2.2(b) and (e)). When the oscillations are regular, the mode is stick-slip sliding (s-s) (Figs. A.2.2(c) and (f)).[104,105] Friction modes of each friction trace are given in Table A.2.1. Overall, stick-slip and irregular stick-slip phenomena occurred more frequently for P30 and P40 substrates lubricated with glycerol, suggesting that low modulus or viscous behavior could be responsible. At the same time, untethered oligomeric chains and dangling ends of P30 and P40 can affect stick-slip sliding in case when the lubricating film is sufficiently thin and some of the asperities on the PDMS surface are in contact[103].

While there was variance within the friction traces, in the following sections we focus on the average friction force (the friction coefficient) during the steady-state, as illustrated by the yellow region in Figure 2.2(c), to discuss the potential influence of viscoelasticity in soft contact.

2.2.3 Influence of Viscoelasticity and Lubricant Viscosity

The friction coefficient was plotted against the sliding velocity in a log scale for varying substrates and environments (Fig. 2.4). As sliding velocity increased, the friction coefficient was also observed to increase (Fig. 2.4 and Fig. A.2.4). While the P10 substrate possessed the lowest friction coefficient for all experimental conditions, P30 and P40 presented the highest friction coefficient; which was the highest depended on the sliding speed and presence of lubricant. In lubricated cases (Figs. 2.4(d)-(i)), viscoelastic hysteresis losses are primarily responsible for the increasing friction coefficient, based on two reasons: 1) the influence of lubricant viscosity is insignificant, which indicates that the lubricating film thickness is only a few nm[76] and the shear stress in the fluid film is negligible, and 2) the friction coefficient is lower in lubricated than dry conditions, which implies that the intervening fluid is still present between the tribopairs, preventing shearing between the adhered junctions at the interface. For dry conditions (Figs. 2.4(a)-(c)), P30 consistently presents a higher friction coefficient than P40 at 0.245 and 1.962 N. The experiments were repeated three to four times. We propose two potential explanations for this phenomenon. First, P40 contains a significant fraction of uncrosslinked monomers and oligomers, more than any other substrates in this work (Fig. 2.5). The disordered molecules are liquid-like, so without other lubricants present, the uncrosslinked molecules could behave as lubricants and reduce friction.[106,107] This friction decrease from the surface properties would be more noticeable at lower preloads (low contact pressure). Second, during tangential motion of the substrate in contact with the stationary probe, P40 substrates will exhibit less elastic resistance against the probe than P30.[108,109] For the high preload, the free chains in P40 are compressed and could

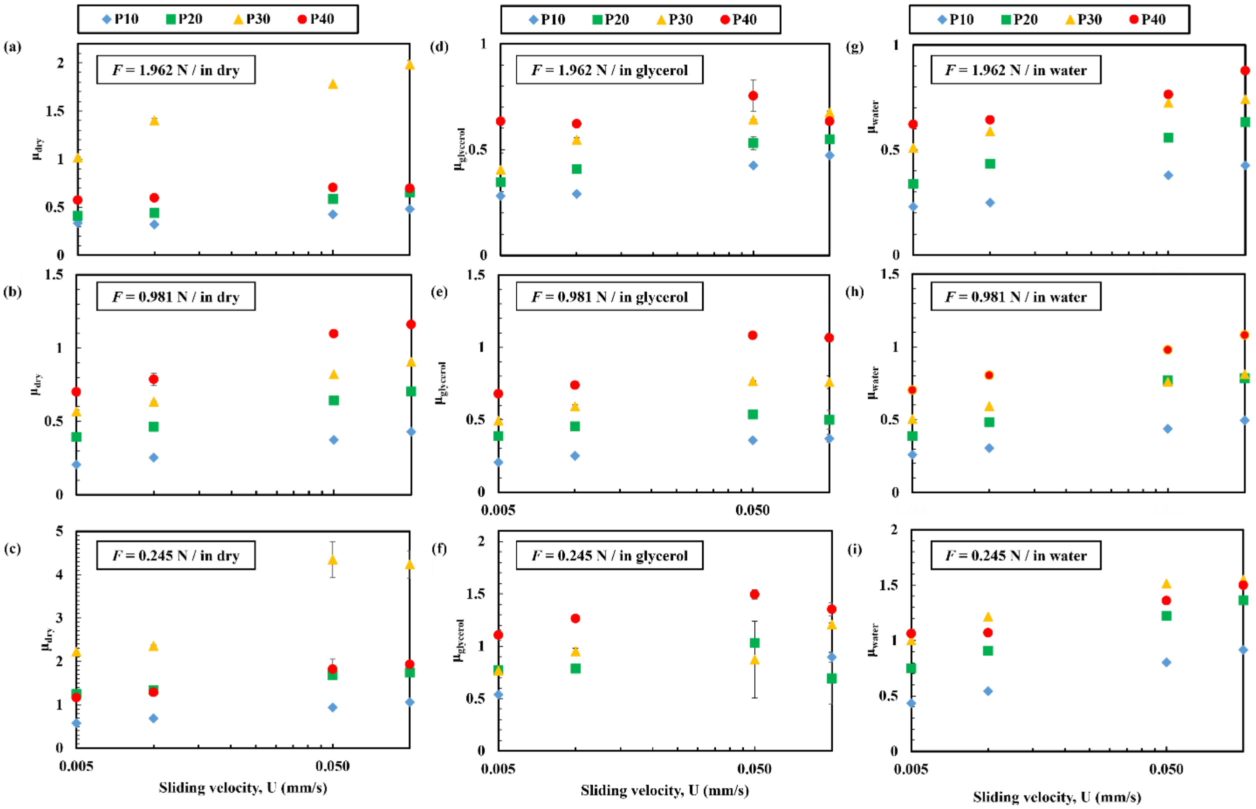

Figure 2.4 Friction coefficient *vs.* preload: The dry friction coefficient (μ_{dry}) under the preloads of **(a)** 1.962, **(b)** 0.981, and **(c)** 0.245 N. The friction coefficient in the glycerol ($\mu_{glycerol}$) at the preloads of **(d)** 1.962 **(e)** 0.981, and **(f)** 0.245 N. The friction coefficient in the water (μ_{water}) under the preloads of **(g)** 1.962, **(h)** 0.981, and **(i)** 0.245 N. Error bars represent standard deviations, though some are smaller than the size of the data point.

behave like a rigid solid, reducing the friction force[110]. These empirical results suggest that the relative influence of bulk material and surface properties should be considered depending on each tribosystem as appropriate. The intermediate mixing ratios of the substrate, P25 and P35 also were tested at the sliding velocities of 0.01 and 0.001 mm/s and the preloads of 0.245 – 1.962 N (Appendix Fig. A.2.3). P25 and P35 present close values to P40 in dry conditions, and P30 and P40 in lubricated conditions.

Assuming there is no adhesion between the surfaces, the theoretical Hertzian contact radii ($a_{Hertz}^3 = \frac{3RF}{4E^*}$) and indentation depths ($D_{Hertz} = \frac{a_{Hertz}^2}{R}$) are calculated. E^* is the reduced elastic modulus, defined as: $\frac{1}{E^*} = \frac{1-{v_i}^2}{E_i} + \frac{1-{v_{ii}}^2}{E_{ii}}$, where E_i, E_{ii}, v_i, and v_{ii} denote the Young's moduli and the Poisson ratios of the tribopairs, respectively (Table 2.1)[111]. Even though the Hertz theory is not ideal for soft tribosystems (adhesion $\neq 0$), Hertzian contact radii have been used to approximate the contact area when direct measurement is not available because of limited experimental apparatus[84,112]. The contact area and indentation depth increase as the elasticity of PDMS decreases. Since the viscoelastic hysteresis losses depend on the contact area,[63,77] this calculated Hertz contact area can be used in the tribosystem with an insignificant interfacial adhesion (*e.g.,* when thin lubricating film prevents the direct surface contact between soft tribopairs). In dry conditions, soft tribopairs can adhere to each surface and the contact area can increase more than the Hertzian contact area; the Hertzian contact area could not be the primary source of friction acting in the tribosystem. In terms of Hertz contact theory, more analysis will be given in the next section.

As mentioned above, the friction coefficient for the tribosystem is not significantly different between glycerol- and water-lubricated conditions (Figs. 2.4(d)-(i)). A study by B. Lorenz *et al.*[76] indicates that the influence of the bulk viscosity of lubricant is insignificant on friction if the lubricating film thickness is less than 10 nm. This suggests that, during sliding, the intervening fluid between the tribopairs is squeezed out and then escapes; at the same time, the softer body of the tribopairs deforms according to the surface contours of the counter body. As the preload increases, the probability also increases that the contact area percolates, and the lubricating film is confined between the deformed surfaces. Nevertheless, in comparison between dry and lubricated contacts, the friction coefficient is lower with lubricant, which indicates that the thin lubricant film is still present between the two surfaces.

Without directly measuring the film thickness or testing the whole lubrication regime, the corresponding lubrication regime can still be estimated based on the experimental results. First, from the insignificant influence of the lubricant bulk viscosity, the approximate lubricant film thickness is assumed to be less than 10 nm[76]. Second, the dimensionless film parameter (ʌ) is ~ 0.3 for all substrates, even when substituting values as large as 100 nm for h_{min} in Eq. (2.3) [113]. Together, these imply that this tribosystem is in the boundary lubrication regime.

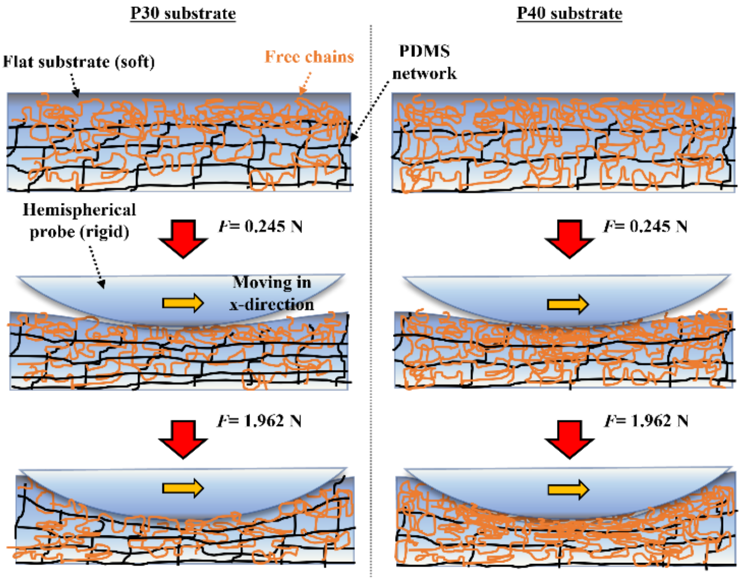

Figure. 2.5 A schematic view of the tribopairs when the probe reaches the stationary flat substrate (P30 and P40) at different preloads: F = 0.245 N (low preload) and 1.962 N (high preload) in dry conditions. The probe is P10 and also has PDMS networks, but for clarity, it was not drawn. P40 substrate (right) presents more free chains and fewer networks than P30 substrate (left). At a constant preload, the substrate travels laterally (in *x*-direction).

2.3.4 Influence of Preload

The influence of preload on the friction coefficient of compliant tribocontact is shown in Figs. 2.6 and 2.7. In dry conditions, the coefficient of friction is proportional to $\sim F^{-0.451}$ (Figs. 2.7(a)-(d)). Unlike Amontons' laws of friction, in many tribosystem, especially for compliant contact, the real area of contact plays a crucial role in determining the friction[110]. When the friction force, F_X is proportional to the theoretical

Hertzian contact area (πa_{Hertz}^2), $\sim F^{2/3}$, the coefficient of friction is proportional to $F^{2/3}/F = F^{-1/3}$, assuming negligible interfacial adhesion[112]. The exponent, -0.451 is lower than the exponent, $-1/3$, from the Hertz contact theory. Therefore, in dry conditions, asperities on the surface adhere at the interface, and a significant portion of the friction originates from outside the Hertzian contact area due to the high Coulombic (interfacial) friction between the tribopairs.

In lubricated contacts, the friction coefficient is proportional to $F^{-0.326}$ for glycerol (Figs. 2.7(e)-(h)) and $F^{-0.34}$ for water (Figs. 2.7(i)-(l)). These exponents, -0.326 and -0.34, are very close to the exponent $-\frac{1}{3}$ from the Hertz contact theory. Even if the lubricating film is too thin for the viscosity difference of the lubricants to affect the friction, this intervening film reduces direct physical contact between the tribopairs, helping the tribosystem to fit the conditions of the Hertz theory. Accordingly, in lubricated conditions, the contact area with lubricants will be similar to the Hertzian contact area (Table 2.1).

Table 2.1 The theoretical Hertzian contact radii and indentation depth of each substrate.

	Preload (N)	P10	P20	P30	P40
a, radii (mm)	0.245	0.479	0.623	0.826	1.136
	0.981	00.761	0.989	1.311	1.803
	1.962	0.959	1.246	1.652	2.272
D, indentation depth (mm)	0.245	0.079	0.134	0.236	0.445
	0.981	0.200	0.337	0.593	1.121
	1.962	0.317	0.535	0.941	1.780

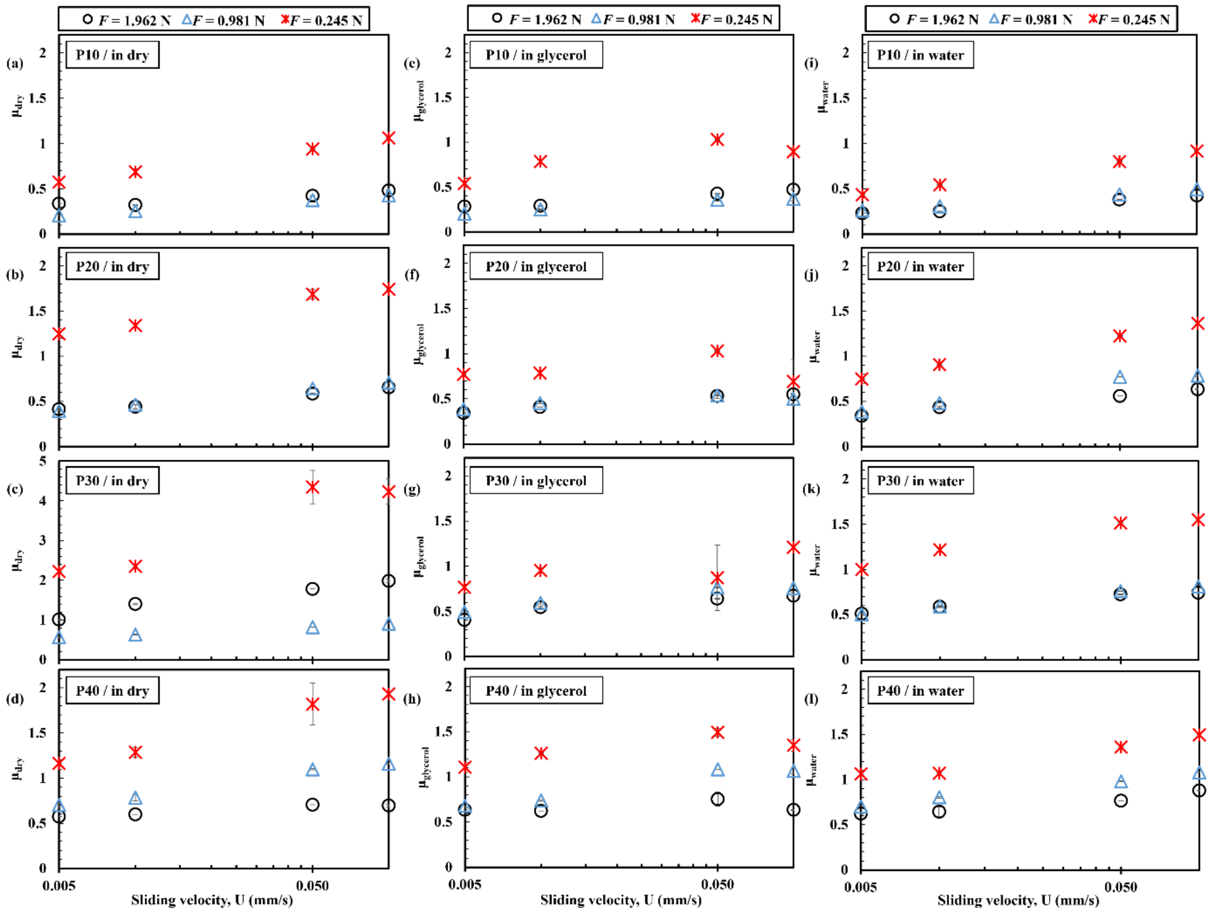

Figure 2.6 Plot of the friction coefficient against the sliding velocity in a log scale with focus on the preload. The dry sliding friction (μ_{dry}) on **(a)** P10, **(b)** P20, **(c)** P30, and **(d)** P40. The friction coefficient in the glycerol ($\mu_{glycerol}$) and in the water (μ_{water}) on **(e)** and **(i)** P10, **(f)** and **(j)** P20, **(g)** and **(k)** P30, and **(h)** and **(l)** P40, respectively. Error bars represent standard deviation, though some are smaller than the size of the data point.

2.3.5 Regression Analysis

The friction coefficient is affected by multiple variables, and the relationship between them is complex. Therefore, in this work, a regression analysis between the empirical friction coefficient (a dependent variable) and various independent variables (sliding velocity, preload, lubricant viscosity, and viscoelasticity of tribopairs) was used to pinpoint the quantitative correlation between the friction coefficient and these variables. Regression analysis has often been used to develop the equations for lubricant film thickness (*e.g.*, the Hamrock and Dowson equations[87,88]). In the full film region, different regression relations of the friction coefficient were introduced depending on its origins: Poiseuille and Couette shear stress in the lubricant film between counter bodies, and elastic deformation losses[77,112]. In this article, regression relations of the friction coefficient for both dry and lubricated conditions was found. Information on lubricant viscosity is given in Appendix (Fig. A.2.5). For dry contact, the regression analysis gives the scaling relationship is given by:

$$\mu_{dry} \sim \frac{E^{*3.293} U^{0.175}}{E'^{3.733} (tan\delta)^{3.801} F^{0.45}} \tag{2.6}$$

It is clear that the loss modulus dominates the friction coefficient, such that μ_{dry} depends on $\sim E'^{3.733}(tan\delta)^{3.801}$ which has the highest exponent among the parameters. In other words, the viscoelastic behavior of the substrates has a significant effect on the friction force in dry sliding contacts. The friction coefficient is also proportional to the reduced elastic modulus (E^{*}) of the tribopairs, calculated based on Hertzian contact theory rather than the singular elasticity of the substrate[111].

In case of lubricated sliding contact with glycerol and water, the scaling relationship is:

$$\mu_{lubricated} \sim \frac{U^{0.151}}{(E' tan\delta)^{0.312} \eta^{0.011} F^{0.333}} \tag{2.7}$$

Here, the friction coefficient appears to depend on $F^{-0.333}$, which is similar to μ scaling with $\sim F^{-0.333}$ in the thin lubricant film within Hertzian contact region[77]. The loss modulus is revealed as the second critical factor, $\mu_{lubricated} \propto (E' tan\delta)^{0.312}$. The loss tangent (or the loss modulus), a rheological parameter, indicates energy loss in the system. This is analogous to the friction force in tribological systems, which is the amount of dissipated energy (as the form of heat)[77,110]. The friction coefficient only scales with the lubricant viscosity with an exponent of 0.01, which agrees with earlier results that showed the viscosity of the thin lubricant film has a negligible effect on the friction coefficient. The regression relations were also obtained using the material properties of the tribopairs at 0.1 and 1 Hz, which are given in Appendix (Table A.2.2). The specific values of the exponents varied depending on the applied oscillation frequencies, but the loss modulus still plays a crucial role in determining the friction coefficient, and the discussion given above is valid. The friction coefficients calculated from the regression relations (*y*-axis) are plotted against the empirical friction coefficients from our results (*x*-axis) in a log-log scale, presenting a high agreement with an adjusted R^2 (based on reduced parameters) of 0.813 and 0.895, respectively (Fig. 2.8). In dry contact, the adjusted R^2 is lower than in lubricated contact because the friction test was relatively less stable due to high Coulombic friction. Therefore, the friction between PDMS-PDMS tribocontacts with varying elasticity, especially at the lower end, was not examined in previous research[65,74,81,83]. However, in our research, to clarify the role of viscoelasticity on friction, we focused on the low range of elasticity and examined the tribological behavior.

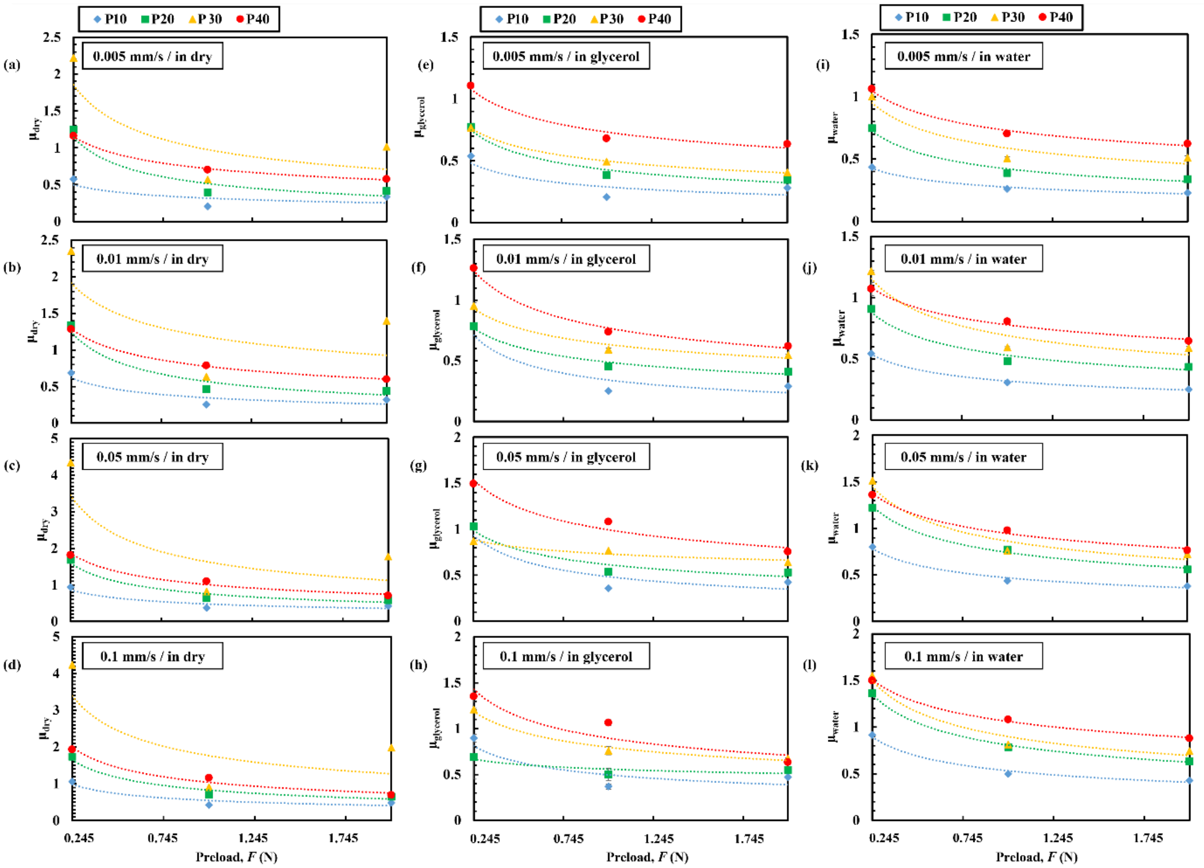

Figure 2.7 Plot of the friction coefficient against the preload at each sliding velocity. The dry sliding friction (μ_{dry}) at sliding velocities of **(a)** 0.005, **(b)** 0.01, **(c)** 0.05, and **(d)** 0.1 mm/s. The friction in the glycerol ($\mu_{glycerol}$) and in the water (μ_{water}) at sliding velocities of **(e)** and **(i)** 0.005, **(f)** and **(j)** 0.01, **(g)** and **(k)** 0.05, **(h)** and **(l)** 0.1 mm/s. The power law fits are $\mu = aF^b$ where a and b are the constant and index, respectively for each experimental condition. Error bars represent standard deviation, though some are smaller than the size of the data point.

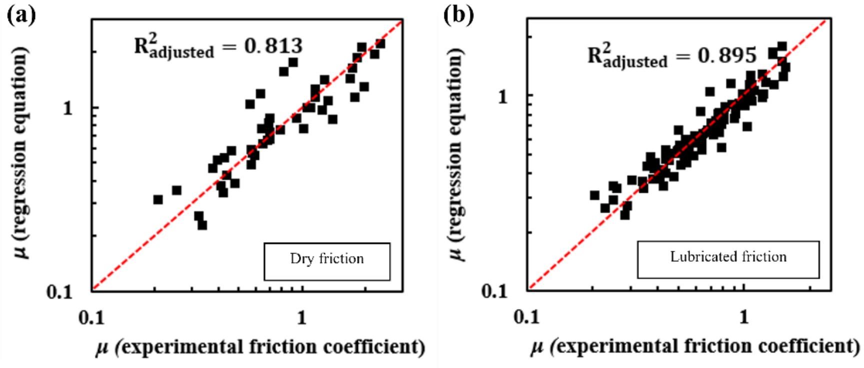

Figure 2.8 Regression analysis against the experimental data. (a) Compliant PDMS contacts in dry conditions: the friction coefficient calculated with the regression relation, Eq. (2.6) (*y*-axis) against the experimental friction coefficient (*x*-axis). The red dotted line is $y = x$. **(b)** Compliant PDMS contacts with lubricants: the friction coefficient calculated with Eq. (2.7) (*y*-axis) against the experimental friction coefficient (*x*-axis): the red dotted line is also $y = x$. Both graphs are plotted in a log-log scale.

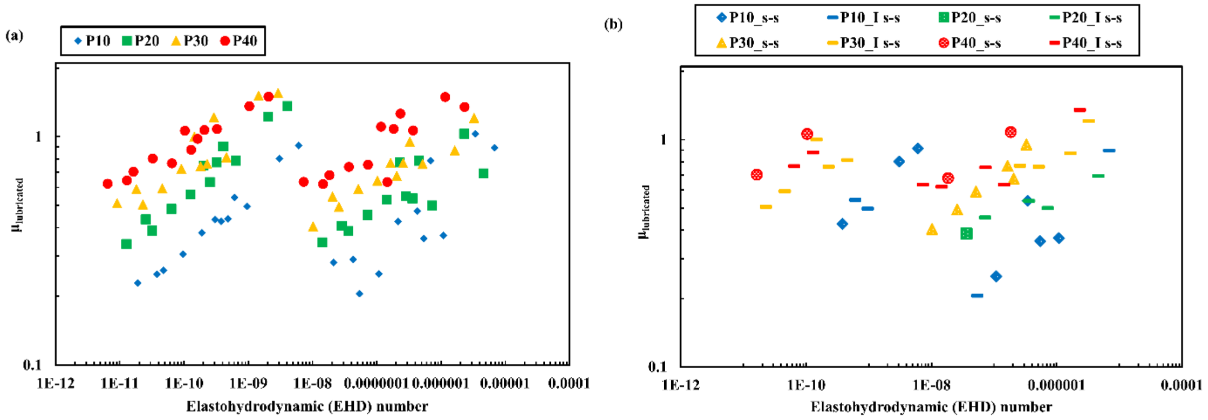

Figure 2.9 The Stribeck curve fitting. (a) The experimental friction coefficient ($\mu_{lubricated}$) (y-axis) versus the elastohydrodynamic (EHD) number (x-axis) in a log-log scale. **(b)** The different modes of steady-state sliding versus the EHD number: "s-s" refers to stick-slip friction, and "I s-s" refers to irregular stick-slip friction.

2.3.6 The Stribeck Curve

Viscoelastic behavior of tribopairs in sliding contacts can also be seen in Stribeck curve fitting. For this fitting, the friction coefficient is plotted against the EHD number (calculated using Eq. (2.2)) in a log-log scale (Fig. 2.9(a)). The EHD number was used because the tested tribosystem has varying values of elasticity, preload, sliding velocity, and lubricant viscosity, and the EHD number is the only nondimensional parameter group which describes these various parameters. Originally, the Stribeck curve was designed for rigid contact, and the EHD number was developed for small elastic deformations in the regime prior to the fully hydrodynamic lubrication regime[64,74,80,114]. However, since an alternative does not currently exist, a Stribeck curve was formed by plotting the empirical data against the EHD number. This approach highlights the need for an alternative form of the Stribeck curve and the EHD number for analyzing highly compliant contact over the whole lubrication regime.

The friction coefficient increases with the EHD number; however, for substrates with different viscoelasticity, there is no collapse of the data onto a single Stribeck curve (Fig. 2.9(a)), as the friction coefficient also increases with the loss tangent of the substrates. Also, two clusters of the friction coefficient can be seen, which originates from the different viscosities of glycerol and water. The two clusters present a similar range of the friction coefficient, further reinforcing the negligible scaling of friction force with viscosity. Overall, the Stribeck curve is different from the conventional model (Fig. 2.1) and the EHD number does not nondimensionalize the tested tribosystem.

In Fig. 2.9(b), the friction coefficients for tested conditions with irregular stick-slip and stick-slip sliding are plotted against the EHD number in a log-log scale. Results with smooth sliding motion are not marked, with the difference can be seen by comparing Figs. 2.9(a) and (b) simultaneously. Stick-slip friction mostly occurs in glycerol-lubricated sliding systems (the right-side cluster in Fig. 2.9). P20 possesses the smoothest sliding friction profiles, while P30 shows the most fluctuations of the friction coefficient. Overall, the lack of distinct pattern suggests that stick-slip friction is not determined by a single experimental condition. It is the combined influence of the key parameters (sliding velocity, viscosity, preload, and the mechanical properties of tribopairs) that generates stick-slip sliding.

2.4 Conclusions

The role of viscoelasticity of tribopairs in a dry and lubricated sliding contact has been explored experimentally. Friction forces between a P10 probe (PDMS 10:1) and P10 – P40 (PDMS 10:1 – 40:1) substrates were measured, controlling other key parameters (sliding velocity, lubricant viscosity, and preload). In comparison to previous studies, the tested moduli were significantly lower, 0.305 – 7.805 MPa, and the substrates had a significant viscous portion (shown by the loss tangent: 0.101 – 0.269). P30 and P40 substrates demonstrated more oscillations in the friction force and the highest friction coefficient in steady-state sliding. Based on the insignificant influence of viscosities, as well as the estimated dimensionless film parameter, this tribosystem was determined to be in the boundary lubrication regime. The effect of viscoelasticity of the tribopairs was clearly seen in regression analysis. In both dry and lubricated conditions, the regression relations of the friction coefficient were in good agreement with the experimental results because they took the loss modulus into account. In dry conditions, the influence of the loss modulus ($\mu_{dry} \sim {E'}^{3.733}(tan\delta)^{3.801}$) is around six times higher than that of lubricated conditions ($\mu_{lubricated}{\sim}(E' tan\delta)^{0.312}$). Interestingly, for lubricated systems, the friction coefficient scales with the preload with the same exponent as the friction in the lubricant film within the Hertzian contact region. This similarity could indicate that there is reduced interfacial adhesion between the PDMS tribopairs due to a thin lubricant film between them. Because of the lack of a suitable dimensionless number or model, the measured friction coefficient is plotted against the elastohydrodynamic (EHD) number in the conventional Stribeck curve. The data does not collapse onto a single line and two clusters are presented due to the thousand-fold difference in viscosities of the lubricants. This work presents the importance of the influence of viscoelasticity on friction, providing information for the design of soft material-based devices as well as insight to deepen understanding of tribological responses of highly compliant materials in both dry and lubricated conditions.

Chapter 3

Capillary Pressure Mediated Long-term Dynamics of Thin Soft Films[†]

The conventional solid-solid contact is well studied in the literature. However, a number of practical applications, such as adhesive patches and biomimetic surfaces, require a much deeper understanding of soft contact where there is a distinct time-dependent adhesion behavior due to the dual-phase structure (solids and liquids). To understand this, currently existing solid-solid contact behavior is extrapolated to soft contact, wherein the size-effect of the gel film and the preload are typically neglected. When introducing the finite-size effect and preload, gels could experience distinctive long-term contact dynamics in contact with another material. We reconstruct the evolving surface profile of the gel films intercalated between a glass sphere and glass slide using dual wavelength-reflection interference contrast microscopy. The macro-sized glass sphere compresses the gel. The indentation depth is comparable to the gel film thickness, wherein the conventional contact theories are inapplicable. The gel surface experiences two deformation stages. The natural preload and elastic force develop the contact area in the early state. In the later state, the viscous free molecules of the gel develop the ridge. We discover that the residual surface stress relaxes over 85 hr. Our findings on the long-term gel deformation provide a new perspective on soft adhesion, from developing soft adhesives to understanding biological tissues.

[†] This chapter is reproduced from A-Reum K., Sushanta K. M., and Boxin Z., "Capillary Pressure Mediated Long-Term Dynamics of Thin Soft Films." *Journal of Colloid and Interface Science*, 2022, vol. 628. 788-797.

3.1 Introduction

Viscoelastic gels have been widely applied in biomedical and engineering fields, ranging from tissue-mimicking materials [14,15,117–119], pressure-sensitive adhesives [120,121], *in-vitro* model studies [1,10,16], soft robotics [12,70,122–124], and anti-biofouling coatings [125,126]. In these applications, gels are all in contact with other materials (soft or hard), experiencing a significant surface deformation. Thus, understanding and controlling how the contact behavior of gels affects the performance of their applications (*e.g.*, adhesion, friction, lubrication) garners great attention. Nevertheless, a number of unresolved issues related to gel-surface interaction remain. Unlike ordinary rigid solids, gels in contact with rigid solids experience a local stretching at the contact boundary (often referred to as ridge formation). Gels present unusual behavior in the ridge because they are semi-solids, in other word, diluted cross-linked systems, composed of at least two different components. One of the components is a substantial amount of liquid phase, which diffuses through a three-dimensional elastic network. The liquid phase does not flow in the steady state. The elastic network gives gels solid-like structures [30,44,91,127–132]. When gels undergo compression, the incompressible liquid molecules are partially extracted from the elastic network. Meanwhile, the elastic network is compressed and then expanded in the direction normal to the compressive load to accommodate the deformation [133]. However, conventional contact theories, such as the Hertz, Johnson–Kendall–Roberts (JKR), and Derjaguin-Muller-Toporov (DMT) theories [134,135], have been unable to explain the surface deformation of the gels in use with non-rigid materials. This is largely because these theories do not account for the significant surface stretching and capillary pressure of the liquids within contact pairs, which play vital roles in the soft contact case.

In recent years, lots of progress have been made to capture and explain the contact behaviors of gels. The adhesion between rigid and soft components and additional energy penalty were considered to develop modified contact theories [44,58]. Such studies include dispensing controlled thickness of silicone oil on a silicone substrate in contact with a glass sphere to study the role of the capillary pressure by the oil film and hence to calculate the total force acting on the contact zone [58]. In addition to building theories on the soft contact with gels, visual observation of the phase-separated free liquids was achieved using fluorescent particles [53]. Because of the gels' incompressibility, the volume conservation law was the basis for analyzing the gels' ridge and the displaced volume of the gel by a contact counterpart (*e.g.,* glass spheres). In most previous studies, the characteristic length scale of the contact parts (*e.g.,* contact radius) was smaller than or close to the elastocapillary length, where the external force (*e.g.,* gravitational force) is negligible compared to the surface stress [30,53,58,136,137]. A further limitation is that most studies have emphasized the ideal geometry of contact pairs (*e.g.,* a semi-infinite thickness of underlying soft substrate) [44,53,58,134,135,137]. Thus, one of the critical assumptions to be incorporated into conventional contact theories is that the effect of soft substrate thickness (H) is negligible compared to the contact radius (a) (or the radius of a contact component (R)); a/H or $R/H \sim 0$, as shown in Table 3.1 and Figure 3.1(a). However, in real applications, we often encounter soft contact systems where external forces are naturally involved, and the size of contact pairs are finite (*e.g.,* pressure-sensitive adhesives, gel-based climbing robots), as illustrated in Figure 3.1(b) [12,121,138–140].

Here we investigate the soft contact system, wherein the external force and finite-size effect predominantly affect the contact behavior of gels. Our study concentrates on the time-dependent development of ridges of intercalated silicone gels between a macro-sized glass sphere and a glass slide using dual wavelength-reflection interference contrast microscopy (DW-RICM) at 488 and 561 nm. The studied contact system has a characteristic length scale (the radius of the glass sphere R = 2.6 mm, the contact radius a = ~ 350 – 480 μm) larger than the elastocapillary length, $L_{ec} = \gamma/E$ = ~ 3.6 μm, where γ and E are the surface energy and elasticity of the gel, respectively. Thus, the external force (here, the weight of the glass sphere) is prevalent. The radius of the glass sphere and the contact radius is ~ 74 – 130 and ~ 14 – 18 times larger than the gel thickness, respectively. We compared this soft contact pair with two different scenarios: a glass sphere in contact with a glass slide and a glass sphere in contact with an elastomer film spin-coated on a glass slide. DW-RICM technique is proven to be a unique tool for reconstructing both the in-plane and out-of-plane deformation of transparent objects in static and dynamic conditions [141–143]. By using DW-RICM imaging, we can image the surface of interest without adding fluorescent particles or a dye. This method allows us to avoid any inherent image distortion and unwanted contact signature changes due to micro/nanoparticles. Our findings show that the contact between the glass sphere and glass slide and between the glass sphere and elastomer film follows the Hertz theory. However, the contact between the glass sphere and gel film does not obey the conventional or modified contact theories. We discuss the associated forces on the contact zone between the glass sphere and gel film and a contact ridge development in two separate stages, *i.e.*, before and after the contact radius is invariant. The residual stress of the compressed gel surface is relaxed over ~ 85 hr. It is observed that when the contact radius increases, the external force predominates, and the gel displaced by the glass sphere forms a ridge on the free gel surface. The final indentation depth by the glass sphere is very close to the finite thickness of the gel film (~ 20 – 35 μm). Phase-separated liquids in the ridge are witnessed due to the capillary imbalance while the viscous flow spreads the ridge base on the free gel surface.

Table 3.1. Representative contact pairs and experimental conditions studied in existing literature and the current work. E: Elasticity. H: Thickness of a substrate. R: Radius of a sphere. G: Shear elasticity. Y: Yield strength. In all literature, the contact radius (a) was not given. Therefore, for consistency, we compare each R/H.

	Contact pairs			Instrument
	Underlying component	Top component	R/H	
D.S.Rimai *et al.* (1994) [135]	Polyurethane rubber (E: 45 kPa, H: ~ 500 μm)	Glass sphere (R: 4 – 105 μm)	0.008 – 0.21	Scanning electron microscopy (SEM)
R. W. Style *et al.* (2013) [44]	Silicone gel (CY 527-276, E: 3 kPa, H: 150 μm; Sylgard 184, E: 85, 250, 500 kPa, H: 70 – 72 mm)	Glass sphere (R: 3 – 30 μm)	0.02 – 0.43	Confocal microscopy
K. E. Jensen *et al.* (2015) [53]	Silicone gel (DMS-V31, E: 5.6 kPa, H: 300 μm)	Glass sphere (R: 7 – 32 μm)	0.02 – 0.11	Confocal microscopy
A. Chakrabarti *et al.* (2018) [55]	Glass slide	Spherical polyacrylamide hydrogel bead (R: 1.2 – 3.8 mm, G: 61 – 789 Pa)	N/A	CCD camera
D. S. Rimai *et al.* (2000) [134]	Polished silicone, plasticized polystyrene, and polyurethane substrate (H >> 11 μm)	Polystyrene sphere (R: ~ 0.2 – 0.35 μm, Y: 10 MPa) and glass sphere (R: ~ 2 – 5 μm)	~ 0.02 – 0.45	Field emission scanning electron microscopy (FESEM)
J. D. Glover *et al.* (2020) [58]	Silicone gel (Sylgard 184 60:1, E: 3.5 kPa, H: 90 μm) coated with silicone oil with a thickness of 3 - 40 μm	Glass sphere (R: 9 – 13 μm)	0.1 – 0.14	Inverted confocal microscopy
Current work	Silicone gel (DMS-V31, E: 5.6 kPa, H: ~ 20 – 35 μm), elastomer (Sylgard 184 10:1, E: 1.43 MPa, H: ~ 35 μm), glass slide	Glass sphere (R: 2.6 mm)	~74 – 130	Dual-wavelength reflectopm interference confocal microscopy (DW-RICM)

3.2 Experimental

3.2.1 Preparation of the Contact Pairs

Glass spheres (McMaster-Carr, 8996K24) and glass slides (Microscope slides, Sail Brand, dimensions: 76.2 mm × 25.4 mm × 1 mm) were thoroughly washed using acetone, IPA, and then DI water before testing. The radius of the glass spheres was measured using a handheld digital microscope (Dine-Lite, AM73915MZT Edge) camera (Fig. B.3.1(a)). Glass spheres and glass slides have an average surface roughness of R_q = 0.39 nm (scanned area: 2 μm x 2 μm) and 7.96 nm (scanned area: 1 μm x 1 μm), respectively (Figs. B.3.1(b) and (c)), which are low enough to have a negligible effect on the contact. We prepared two soft films, elastomer and gel films. For elastomer films, PDMS base and curing (Molecular weight: 27kg/mol, Dow Corning, Sylgard 184) agent were mixed in a weight ratio of 10:1 using a planetary mixer (Thinky Corporation, ARE-310) for 8 minutes. The elastomer films had Young's modulus (E) of 1.4 MPa, measured by tensile testing. This value corresponds to our previous work's measured elasticity by dynamic mechanical analysis (DMA) test [144]. The surface energy of the elastomer film is 20.6 mN/m [145]. For gel films, we used two components: Part A consisted of the base, divinyl-terminated polydimethylsiloxane (PDMS) (M_w: 28kg/mol, Gelest, DMS-V31) with 0.05 wt% of the catalyst (M_w: 474.68 g/mol, Gelest, SIP6831.2), and Part B consisted of the base with 10 wt% of the curing agent (M_w: 1.95 kg/mol, Gelest, HMS-301). Parts A and B were mixed in a weight ratio of 9:1 using the planetary mixer for 3 minutes. The gel has Young's modulus $E = 5.6$ kPa [53]. In the study of soft contact, the gel is often used as a representative of other soft materials (*e.g.,* cells (E: 0.001 – 0.1 MPa) and hydrogels (E: ~ 0.1 MPa)) because of its inertness and similar elasticity [55,111,146]. 1 ml of each base was spin-coated on a clean glass slide at 900 – 20,000 rpm for 45 seconds. After the prepolymer was cured at 80 °C for 12 – 14 hours, the gel formed 20, 30, and 35-μm-thick smooth films, and the elastomer base formed a 35-μm-thick smooth film. The fabricated films were composed of cross-linked polymers containing the same free liquid, silicone oil, which is likely a mix of linear, cyclic, and branched chains of unknown molecular weight [147]. The elastomer and gel films have a Poisson's ratio v of 0.48 – 0.5 [53,148]. After removing the films from the oven, each film rested at 22 – 24 °C for 1 – 2 days. Soft films coated on a glass slide were used without further treatments and placed on a microscope stage. According to solvent extraction, the elastomer and gel film contained 4.9 and 62 wt. % of free liquids in the network, respectively. Experimental details are included in Appendix B. Tested glass spheres were not used again due to the potential contamination from contact with the gels.

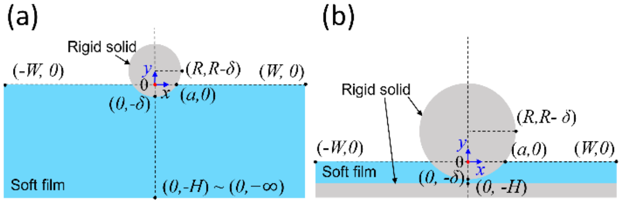

Figure 3.1 Geometries in the study of soft adhesion between a rigid sphere and gel film. (a) Semi-infinite gel film thickness. $(0, -H)$ can be considered as $(0, -\infty)$ because the contact radius (a), glass sphere radius (R), and indentation depth (D) are significantly smaller than the gel film thickness (H), wherein the film thickness effect is negligible. ($a/H, R/H,$ and $D/H \sim 0$). **(b) Finite gel film thickness.** The contact radius and glass sphere radius are larger than the gel film thickness. The indentation depth is comparable with the gel film thickness. (a/H and $R/H \;>>\; 1, D \sim H$). In both geometries, the width of the soft films $(2W)$ is significantly larger than a and R $(R/W, a/W \sim 0)$.

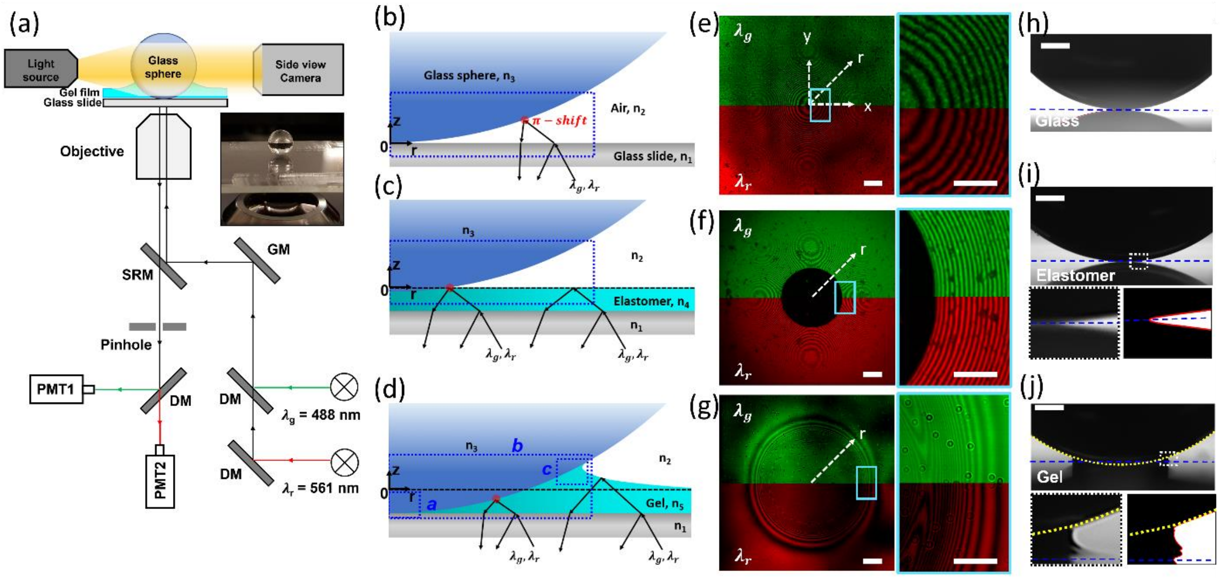

Figure 3.2 Experimental schematics of configurations and imaging of contact pairs. (a) Experimental set-up of dual wavelength-reflection interference contrast microscopy (DW-RICM) and side-view observation. Two monochromatic lights are utilized (*viz.*, λ_g: 488 nm, λ_r: 561 nm). SRM: semi-refractive mirror, GM: galvanometric mirror, DM: dichroic mirror, PMT: photomultiplier tube. **(b-d) Schematic view of contact pairs: (b)** glass sphere-glass slide contact, **(c)** glass sphere-elastomer film-glass slide contact, and **(d)** glass sphere-gel film-glass slide contact. Dotted blue boxes indicate focused areas using the DW-RICM. In the glass-gel film-glass contact, three different locations, *a*, *b*, and *c* are observed. Local points where π-shifts occur are highlighted as red circles. The refraction and reflection angles are not scaled. **(e-g) Unprocessed interferograms of each contact pair with each inset (250 μm scale bar): (e)** glass-glass contact, **(f)** glass-elastomer-glass contact, and **(g)** glass-gel-glass contact. x and y coordinates determine the radial distance (white dotted lines). Along the *r*-axis, the raw light intensities are measured. The interferograms obtained using the two monochromatic lights in the same region are merged. Scale bar: 100 μm. **(h-j) Side view of the contact: (h)** glass-glass contact, **(i)** glass-elastomer-glass contact (original, cropped, and cropped binarized image in anti-clockwise direction), and **(j)** glass-gel-glass contact (original, cropped, and cropped binarized image in anti-clockwise direction). Scale bar: 500 μm.

3.3 Results and Discussion

3.3.1 Reconstruction of the Adhesive Contact Profile

We used glass slides and two soft films (elastomer and gel) as underlying parts and 2.6-mm-radius plain glass spheres as upper contact parts. Three different contact pairs are named 'glass-glass', 'glass-elastomer-glass', and 'glass-gel-glass' contacts. A glass sphere was placed on the underlying films, allowing its weight (1.24 mN, measured using a scale) to apply pressure on the underlying films. The contact geometry was observed using DW-RICM and a side-view camera, as illustrated in Figure 3.2(a).

In DW-RICM, we raster-scanned the surface of interest (glass spheres or each underlying film) simultaneously with two focused beams of monochromatic lights with wavelengths λ_g = 488 nm and λ_r = 561 nm (g = green, r = red). The imaged areas are approximately marked as dotted blue lines in Figures 3.2(b)-(d). In the glass-glass contact, interference occurred between the light reflected at the glass slide-air interface and the air-glass sphere interface (Fig. 3.2(b)). For the contact with soft films, the light rays reflected at the glass slide-soft film interface and the soft film-air interface (Figs. 3.2(c) and (d)). Representative interferograms of each contact pair are given in Figures 3.2(e)-(g). Each half of the observed area using λ_g and λ_r is attached to compare fringes with each magnified view near the contact boundary. Alternated constructive and destructive interference leads to bright and dark fringes, creating concentric circular Newton rings. Interferograms of λ_g and λ_r present different bright and dark fringes positions, enabling us to validate the surface profile independently. Along the radial direction (r-axis), the raw light intensities (I_r) of interference were measured and then normalized according to Equation (A.1) to eliminate the background noise. The 1D coordinate along the radial direction is given by $r = \sqrt{(x - a_x)^{2} + (y - a_y)^2}$ where a_x and a_y are the center of the contact. The reference plane is the free (unperturbed) surface of each substrate (where h = 0), and the origin is decided as the center of the sphere

(a_x, a_y). The surface profile was reconstructed based on the normalized intensity maxima and minima using Equation (A.13). Analysis was performed using MATLAB. A detailed description of the data analysis is given in Appendix B. The glass-glass and glass-elastomer-glass contact formed non-conformal contact (Figs. B.3.2(h) and (i)). In contrast, the glass-gel-glass contact created a significantly bigger contact area and a contact ridge (Fig. 3.2(j)).

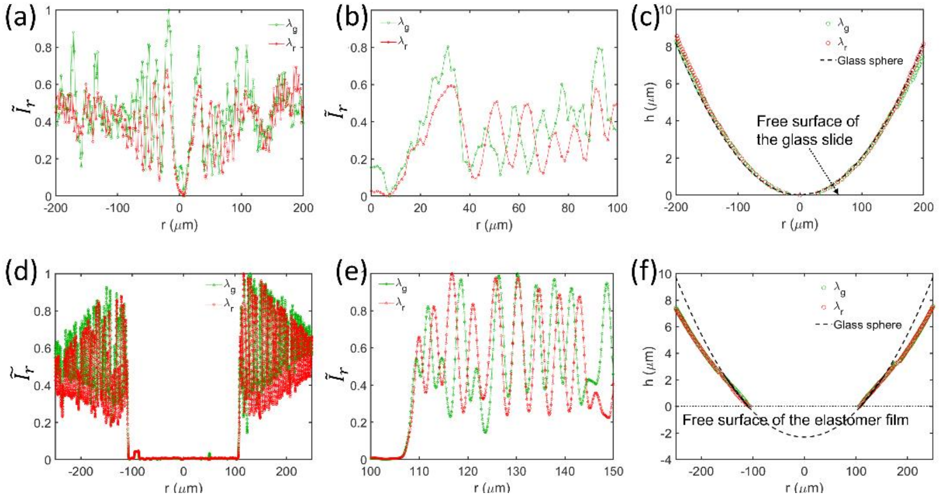

Figure 3.3 (a-c) Glass-glass contact: the normalized light intensities $(\widetilde{I_r})$ for λ_g and λ_r as a function of radial distance over **(a)** from – 200 μm to 200 μm and **(b)** from 0 μm to 100 μm, and **(c)** the calculated gap distance (h) and the actual profile of the glass sphere, plotted according to $h(r) = 2600 - \sqrt{2600^2 - r^2}$. The surface of the glass slide is on $h = 0$. **(d-f) Glass-elastomer-glass contact**: the normalized light intensities $(\widetilde{I_r})$ for λ_g and λ_r as a function of radial distance over **(d)** from – 250 μm to 250 μm and **(e)** from 100 μm to 150 μm, and **(f)** the calculated gap distance (h) and the ideal profile of the glass sphere, plotted according to $h = 2597.57 - \sqrt{2600^2 - r^2}$. The free surface of the elastomer film is on $h = 0$. The origin of the r-axis is the center of the glass sphere.

3.3.2 Glass-glass Contact

We used the glass slide and sphere to validate our experimental and theoretical approach. The resultant raw light intensities were normalized using Equation (A.1) (Fig. 3.3(a)). The frequencies of λ_g are higher than λ_r due to the shorter wavelength (Fig. 3.3(b)). Since the glass sphere and glass slide have the same refractive indices, the light intensity is ~ 0 at the contact point (r = 0). In Figure 3.3(c), the calculated profile of the glass sphere using Equation (B.3.13) agrees well with the actual profile of the glass sphere, $h(r) = 2600 - \sqrt{2600^2 - r^2}$ obtained based on the side view (Fig. 3.2(h)). The measured radius (R = 2.6 mm) from Figure 3.2H agrees well with the measured radius from the top view of the glass sphere (see Appendix Fig. B.3.1(a)).

3.3.3 Glass-elastomer-glass Contact

The same technique and analysis were applied to find the profile of the intercalated elastomer film between the glass sphere and glass slide. A glass sphere was placed at the center of the elastomer film. The raw intensities were normalized (Figs. 3.3(d) and (e)), and the elastomer surface profile was reconstructed (Fig. 3.3(f)). After direct contact with the glass sphere, the elastomer film recovers its initial free surface as adhesion outside direct contact does not predominate. In the direct contact region, the light intensity is ~ 0 because the glass sphere and elastomer film have a lower refractive index mismatch than the elastomer film and air. Half of the distance with the light intensity ~ 0 is 106.9 µm, which is consistent with the experimental contact radius (a_M) of 106.9 µm, calculated based on the contact area (Fig. B.3.4). The local contact radius between the glass sphere and elastomer film might vary in the radial direction (Fig. B.3.4(b)). Hence, we extracted the average contact radius from the contact area (Figs. A3.4(c) and (d)). The Hertzian contact radius (a_H) [149] is 105.54 µm, calculated as:

$$a_H^3 = \frac{3FR^*}{4E^*} \tag{3.1}$$

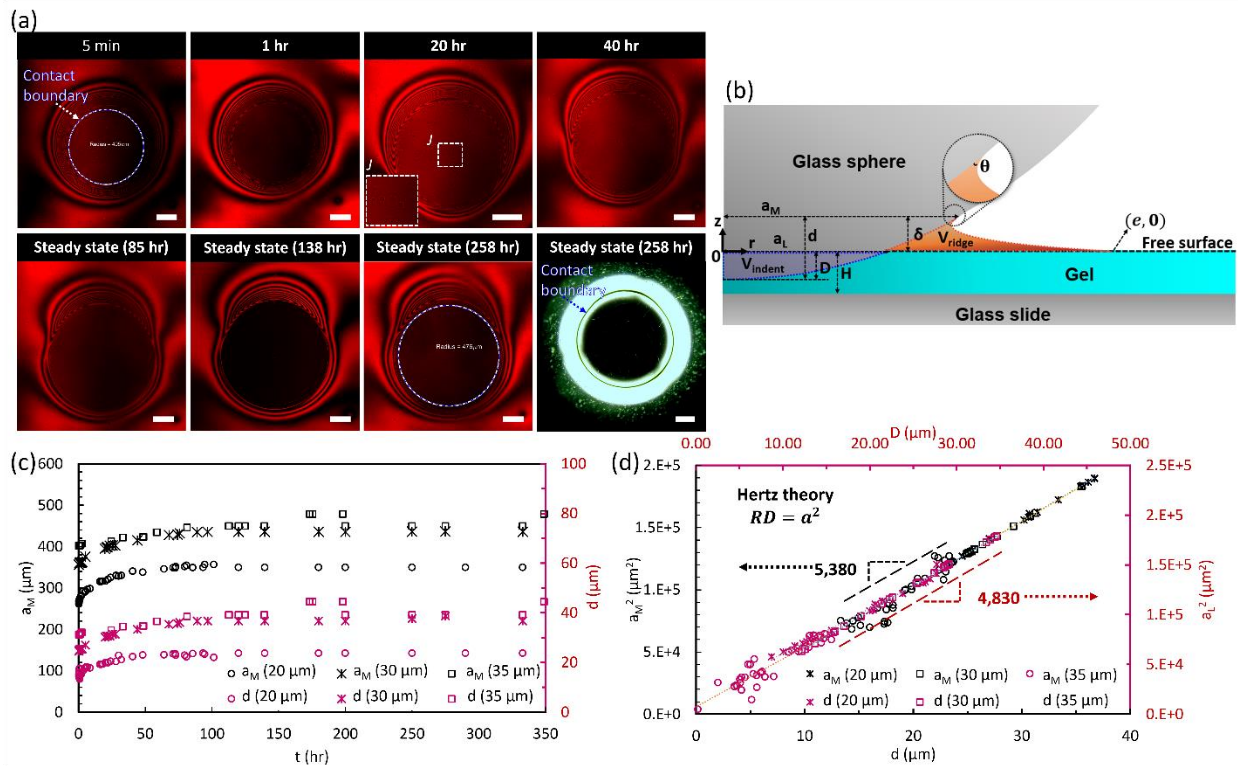

Figure 3.4 Time-dependent surface deformation of the gel thin film. (a) Interferograms of glass-gel (thickness: 35 µm)-glass contact at 5 min, 1 hr, 20 hr, 40 hr, 85 hr (steady state), 138 hr (steady state), and 258 hr (steady state), and the optical microscopic bottom view of the contact area. Scale bar: 200 µm. **(b)** Schematics of the contact zone. V_{ridge} includes the volume of the phase-separated liquids and elastic network. **(c)** The contact radius (a_M) and the submerged depth (d) against the time (t) for the gel films with the thickness of 20 – 35 µm. **(d)** Each square of the contact radii (a_M^2 and a_L^2) against the submerged depth (d) and indentation depth (D) for the gel films with the thickness of 20 – 35 µm, respectively.

where F is the applied normal load (1.24 mN), R^* is the reduced radius, $R^* = \left(\frac{1}{R_1} + \frac{1}{R_2}\right)^{-1} \approx R_1$ where R_1 and R_2 are the radius of the glass sphere (2.6 mm) and each film (∞), and E^* is the composite elastic modulus: $E^* = \left(\frac{1-v_1^2}{E_1} + \frac{1-v_2^2}{E_2}\right)^{-1} \approx \left(\frac{1-v_1^2}{E_1}\right)^{-1}$ where E_1 (64 GPa) and E_2 (1.43 MPa) are the elasticities of the glass sphere and elastomer, and v_1 and v_2 denote their respective Poisson's ratio, which is both ~ 0.5 [41,150,151]. The Hertzian indentation depth (D_H) is 4.74 µm (Equation B.3.18). The subscript, H of a_H and D_H means the Hertz theory. The ratio of the contact radius to the film thickness (a/H) is > 3, which is bigger than the assumption of the Hertz theory $(a/H \sim 0)$. The modified Hertz theory was introduced when the underlying film reduced in thickness, wherein the film cannot be considered as an elastic-half space [138]. The finite-size effect was incorporated into the conventional Hertz theory, introducing the parameter a/H. The modified theory is applicable in $0 < a/H < 5$. In the modified theory, the calculated contact radius is 80 µm (see Appendix Eq. B.3.21), which is only ~ 75 % of a_M. Even if a/H is in the range of the modified Hertz theory, the conventional Hertz theory is still applicable to the glass-elastomer-glass contact.

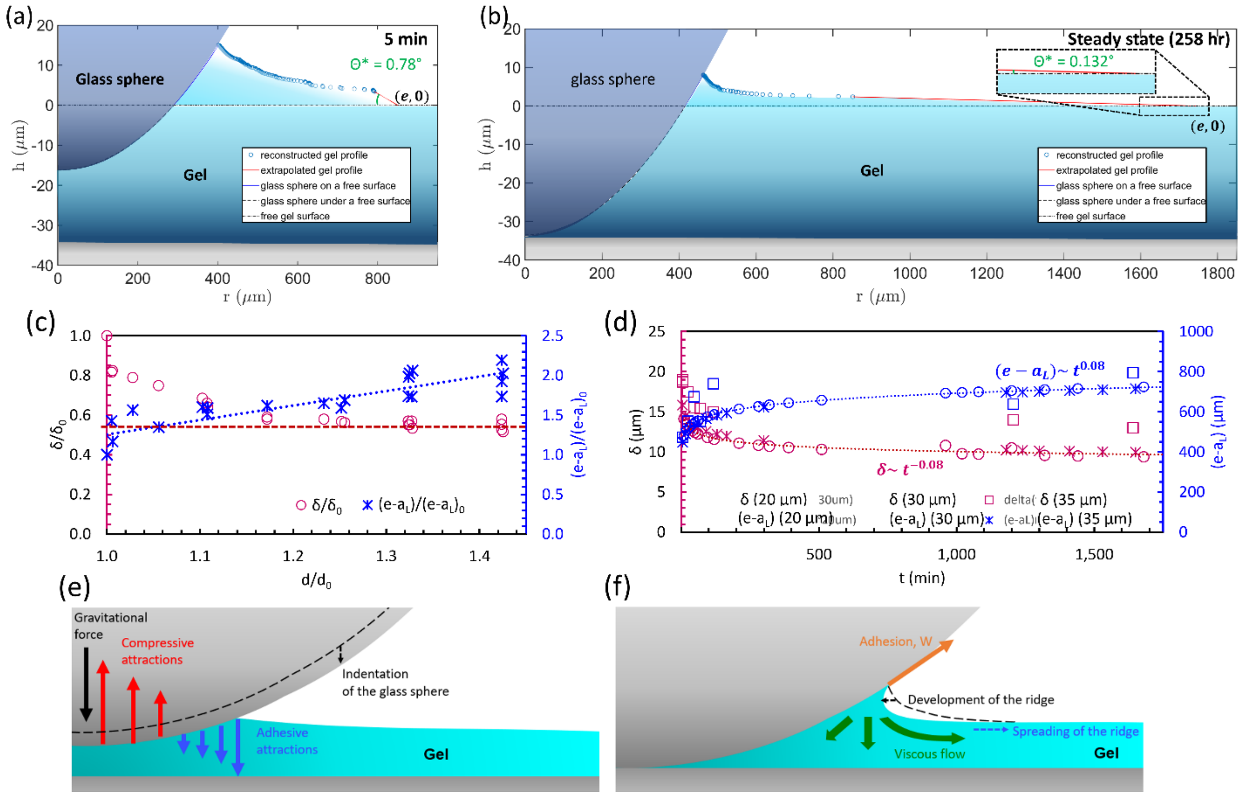

Figure 3.5 Two separate stages in the evolution of the gel thin film. (a) Representative initial surface deformation of the gel (thickness: 35 μm) after 5 min contact. The end of the perturbed gel surface has an angle (θ^*) of 0.78 ° compared to the free surface. **(b)** Representative steady state of the gel surface (thickness: 35 μm). The end of the perturbed gel surface spreads on the free gel surface with an angle (θ^*) of 0.13 °. **(c)** The normalized ridge height (δ/δ_0) and the normalized ridge width $(e - a_L)/(e - a_L)_0$ against the normalized submerged depth (d/d_0) of the gel film (thickness: 35 μm). **(d)** The plot of δ and $e - a_L$ against the time (t) of the gel films (thickness: 20 – 35 μm). δ is proportional to $t^{-0.08}$ and $e - a_L$ is proportional to $t^{0.08}$. **(e)** Associated forces in the early stage. **(f)** Spreading of the ridge in the later stage wherein the indentation depth is comparable to the gel film thickness. The geometries of each component are not scaled.

3.3.4 Glass-gel-glass Contact

We observed the intercalated gel film deformation between the glass sphere and glass slide, focusing on three regions, a, b, and c, as illustrated in Figure 3.2(d). In region a (scanning area: 200 μm × 200 μm), clear Newton rings are observed (Fig. B.3.5(a)). The reconstructed gel profile corresponds to the profile of the glass sphere, indicating direct contact between the glass sphere and gel film. (Fig. B.3.5(b)). In region b (scanning area: 1.83 mm × 1.83 mm), we found time-dependent deformation of the gel film of different thicknesses. Representative interferograms with the gel film of 35-μm-thickness are shown in Figure 3.4(a) and Figure B.3.6. Interferograms of the 20 and 30-μm-thick gel films are presented in Figures B.3.7 and B.3.8. The direct contact zone corresponds to the clear region without fringes (Figure 3.4(a) (5 min)). The first interferogram was taken after ~ 5 min in contact because of the ~ 5 min frame time. The origin of the r-axis was decided based on the Newton rings, as shown in the magnified view, J in Figure 3.4(a) (20 hr). Here, we define the steady state as the state in which no further surface deformation of the gel occurs. a_M and the calculated submerged depth (d) from the contact radius increase gradually until they reach a nearly constant value (Figure 3.4(b)). a_M and d of each gel film are 349.97 μm, 23.7 μm (the 20-thick-gel film), 435.58 μm, 39.13 μm (the 30-thick-gel film), 478.50 μm, and 44.41 μm (the 35-thick-gel film), respectively, after 85 hr (Fig. 3.4(c)); $d = 2600 - \sqrt{2600^2 - a_M^2}$. The 30 and 35-μm-thick-gel-films have a similar contact radius and submerged depth, while the 20-μm-thick-film presents a much smaller contact radius and submerged depth than that of thicker films. At the steady state, the contact radius measured using DW-RICM agrees well with the contact radius measured using an inverted optical microscope. Optical microscopic bottom views of 20 and 30-thick-gel films are shown in Figure B.3.9. Hence, we ascertain that the interferogram shows the correct contact radius despite the profile's limited measurable slope (see Appendix Equation B.3.3). In the glass-gel-glass contact, a/H is ~ 13.6 – 17.5. The schematic of the contact zone in Figure 3.4(b) is drawn based on the interferogram and the side-view (Figure 3.2(j)). It is worthwhile to mention that d is not the same as the indentation depth (D) and a_M is different from the contact radius on the free surface (a_L). In cases when the adhesion between two contact parts is negligible (such as glass-elastomer-glass contact), d and a_M are smaller than D and a_L, respectively (Fig. B.3.4(a)). When the adhesion dominates the contact and the upper component indents into the underlying substrate, d and a_M are larger than D and a_L, respectively (Fig. 3.4(b)).

At the magnification of 10×, the resultant light intensities are insufficient to reconstruct the gel profile (Fig. B.3.6(a)). Therefore, we focused on the smaller area, region c (Fig. 3.2(d)) at the higher magnification 40×, by dividing the whole contact zone into four sub-sections over 450 – 640 mm × 450 – 640 mm (Fig. B.3.6(b)). The resultant light intensities were collected in the sub-sections and then averaged to reconstruct the gel profile. As the contact time increases, the number of interference rings near the contact boundary increases. In contrast, the opposite trend is displayed when far from the contact boundary, implying that the gradient $\partial h/\partial r$ of the contour increases closer to the contact boundary. The observable area at one time is limited, so the reconstructed profile does not cover the whole gel deformation (Fig. B.3.10(a)). The rest of the gel profile was reconstructed by extrapolating the known gel profile (Fig. B.3.10(b)). The gel is incompressible, so the end of the perturbed gel surface $(e, 0)$ was determined based on the volume conservation between the indented volume of the glass sphere (V_{indent}) and the ridge volume (V_{ridge}), as illustrated in Figure 3.4(b) [53]. V_{ridge} includes all the vertically lifted gel volume which includes the elastic network and free liquids of the gel [44,53,152]. a_L can be calculated because we know the glass sphere radius (R), a_M, and the ridge height (δ) from the reconstructed surface profile of the gel film. D is simply calculated according to $D = d - \delta$. The 3D view of the contact zone is shown in Fig. B.3.10(c). The analysis is performed in MATLAB, as described in Appendix B.

As expected, a_M is smaller than a_H of 785 μm (based on Equation (3.1)) and the conventional JKR contact radius (a_{JKR}) of 1,000 μm because of the finite film thickness. a_{JKR} is calculated as [153]:

$$a_{JKR}^3 = \frac{3R^*}{4E^*}\left(F + 6\gamma_{12}\pi R^* + \sqrt{12\gamma_{12}\pi R^* F + (6\gamma_{12}\pi R^*)^2}\right) \qquad (3.2)$$

where γ_{12} is the interfacial tension in contact (~ 44 mN/m, see Appendix B). The conventional JKR theory was built based on the balance between the adhesion and elastic stresses, assuming the semi-finite film thickness. The fact that the glass-gel-glass contact is accompanied by a large adhesion contribution from the stretched surface is demonstrated by plotting a_M^2 and a_L^2 against d and D, as shown in Figure 3.4(b). If the contact pairs do not form adhesive contact, a slope of the data points would be close to the sphere radius of 2.6 mm; based on the correlation, $RD = a^2$ [149]. However, the slope is ~ 5 mm for both contact radii, a_M^2 and a_L^2. It is worth mentioning that the gel's shear elasticity used to calculate the Hertzian and JKR contact radius is invariant in the studied contact because at shear strains in the range of 10^{-2} to 10^{2}, the shear stress has a linear correlation with the shear strain [146]. Here, the maximum strain rate is ~ 1 %, a relative length ratio of the stretched gel surface after the contact to the original gel surface before the contact. Note that the gel surface was unlikely to have any plastic deformation during the indentation of the glass sphere in our system, as shown in Figure B.3.11(b). We measured the force while moving the glass sphere toward the gel film. For comparison, we tested the elastomer film together. The measured force and theoretically calculated force (based on Hertz theory) showed that the surface deformation of the elastomer and gel film was within the elastic deformation regime.

We looked for other applicable theories for the contact mechanics of the glass-gel-glass contact. The modified JKR theory for the finite-size effect (also called a generalized version of the JKR theory while the conventional JKR theory is called a standard version) was unsuitable because of the limited applicable range of $0 < a/H < \sim 5$ [138]. In the modified JKR theory for the finite-size effect, the glass sphere is still fully indented, while the underlying glass slide (where the soft film is coated on) provides restrictions on the indentation. However, here, the film thickness of the gel is insufficient for a full indentation, restricting the indentation of the glass sphere directly. Hence, the indentation depth of the glass sphere is close to the gel film thickness. The film thickness determines the contact radius. The modified JKR theory [44] for incorporating the role of the surface tension was not suitable because the characteristic length of the current contact was larger than the elastocapillary length (L_{ec} ~ 3.6 μm).

3.3.5 Development of the Ridge in the Glass-gel-glass Contact

In the previous section, we have found that the glass-gel-glass contact does not follow the above-mentioned conventional [149,153] or modified contact theories [44,138]. In this section, we discuss the mechanisms of ridge formation and dominating factors that make the glass-gel-glass contact different from the previously studied systems.

The representative 2D reconstructed profiles of the gel film are shown in Figures 3.5(a) and (b). Here, the characteristic length scale of the contact system is larger than the capillary length of 1.5 mm, calculated as $L_c = \sqrt{\frac{\gamma}{\Delta\rho g}}$ where $\Delta\rho$ is the density difference of the gel and air, and g is the gravitational acceleration. Therefore, the external preload (the gravitational force) dominates the contact. Right after the glass sphere is placed on the gel film, the displaced volume of the gel by the glass sphere creates the ridge on the free gel surface. For the gel films of three different thicknesses, the ridge has a small but noticeable slope with an angle (θ*) of 0.78 ° (20-μm-thickness), 0.79 ° (30-μm-thickness), and 0.76 ° (35-μm-thickness) at the intersection $(e, 0)$ between the perturbed and free gel surface. A constant preload of the glass sphere continuously compresses the gel surface, and the sphere is indented into the gel, broadening the ridge base and decreasing the ridge height. At the steady state, the angle (θ*) decreases to 0.13 ° (20-μm-thickness), 0.12 ° (30-μm-thickness), and 0.11 ° (35-μm-thickness). On average, θ* at the steady state corresponds to 17 % of the initial angle. The small deviations among different thicknesses tell that the gel film thickness does not affect the slope of the ridge base close to the free surface.

As shown in Figure 3.5(c), for the 35-μm-thick-gel film, the normalized height of the ridge $\left(\frac{\delta}{\delta_0}\right)$ becomes nearly invariant with a value of 0.53 as the normalized submerged depth $\left(\frac{d}{d_0}\right)$ approaches 1.2, while the normalized ridge width $\frac{e-a_L}{(e-a_L)_0}$ increases continuously. The steady state values of $\left(\frac{\delta}{\delta_0}\right)$ and $\left(\frac{d}{d_0}\right)$ decrease as the gel film thickness decreases due to the smaller indentable depth, as shown in Figure B.3.12.

For the 20-μm-thick-gel film, $\left(\frac{\delta}{\delta_0}\right)$ and $\left(\frac{d}{d_0}\right)$ reach 0.66, 1.51. For the 30-μm-thick-gel film, $\left(\frac{\delta}{\delta_0}\right)$ and $\left(\frac{d}{d_0}\right)$ approach 0.55, and 1.71. In Figure 3.5(d), the ridge height (δ) and width ($e - a_L$) are proportional to the observation time $t^{-0.08}$ and $t^{0.08}$, respectively. The absolute value of the exponents ($= 0.08$) is smaller than the exponent ($k = 0.59$) in the power-law rheology correlation of the gel: $G^*(\omega) = G'\left(1 + (i\omega\tau_c)^k\right)$ where G^*, G', ω, and τ_c are the complex shear elasticity, shear storage modulus, frequency, and viscoelastic time scale, respectively [154,155]. The surface deformation takes a much longer time than the viscoelastic time scale $\tau_c \sim 0.09\ s$, because of the large contribution of the external preload in the system.

The surface deformation of the gel film continued over a couple of days within the elastic deformation regime due to the finite thickness of the gel and the external preload. The long-term evolution was observed for the three different gel thicknesses. The viscoelastic gel might also be poroelastic because of the migration of the un-crosslinked liquids in the reticulated polymer network. Long-term and large-scale deformations are typical features of poroelasticity [152]. The effect of poroelasticity was found at the contact boundary. The poroelastic diffusion of liquids makes the contact system follow the Young-Dupré law with balancing the interfacial energies, as shown in ref. [53]. We confirmed the phase-separation of free liquids from the gels' network using the contact angle measurement. DW-RICM cannot provide a separate profile of the free liquids and elastic network in the ridge due to their similar refractive indices. The gel profile near the glass sphere is also over the measurable limit $\left(\frac{dh}{dr}\Big|_{max} = 0.079\right)$ of DW-RICM (see Appendix B). Hence, we measured the contact angle between the glass sphere and gel ridge instead to confirm the liquid phase at the contact boundary. The angle between the gel base (free liquids) and glass slide (~ 4 °) (Fig. B.3.13) is close to the contact angle between the glass sphere and gel ridge ($\theta =$ ~ 4 °) (Fig. B.3.16), implying the phase-separation of the liquids. To mimic the glass-gel-glass contact system using materials with a known phase (liquid or solid), we dispensed a droplet of silicone oils with the surface tension of $\gamma =$ ~ 21 mN/m (Fig. B.3.14) between the glass sphere and elastomer film (Fig. B.3.17). The surface tension of silicone oils is close to that of the gel base (~ 20 mN/m) but 10 – 20 times less viscous than the gel base. Therefore, the silicone oils instantly formed a capillary bridge and reached its steady state in a minute. The average contact angle between the glass sphere-silicone oil-elastomer film is ~ 6.9 °, close to that between the glass sphere and gel ridge, implying the phase-separation of the free liquids.

The possible contribution of poroelasticity on the ridge's overall evolution was evaluated using the indentation test to check whether the gel deformation depends on the observation scale (Fig. B.3.15). Detailed test methods are given in Appendix B. While pressing a gel surface using a glass indenter, the resultant force ($F(t)$) was measured. The resultant force was normalized and plotted against the observation time (t) and scaled time $\left(\frac{t}{RD}\right)$ where $\sqrt{RD}$ is the diffusive length scale; R and D are the indenter radius and indentation depth, respectively. The normalized force is collapsed onto a single line against t, not $\frac{t}{RD}$, indicating the size-independent characteristic of the measured force. Hence, it can be concluded that the viscoelasticity of the gel dominates the overall ridge development rather than the poroelasticity.

Based on the observed contact behavior of the gel surface, it was found that the ridge development of the gel film with a finite thickness shows two distinctive stages. In the early stage, the external preload by the glass sphere enlarges the contact radius at the cost of elastic strain. In this stage, the ridge is not fully developed (see Fig. 3.5(e)). Once the contact radius reaches a constant value (the later stage), the ridge width increases to accommodate the replaced volume of the gel by the glass sphere. The ridge height is nearly invariant as approximately half of the initial height, but the ridge width increases until the steady state. The surface deformation in the later stage accompanies the viscous flow of the liquid phase in the elastic network to evolve the profile (see Fig. 3.5(f)).

3.4 Conclusions

We have shown how the gel film with different finite thicknesses can deform in contact with a glass sphere over the long term with being intercalated between a macro-sized glass sphere and glass slide (glass-gel-glass) using dual wavelength-reflection interference contrast microscopy (DW-RICM), in comparison with two different contact pairs: glass sphere-glass slide (glass-glass) and glass sphere-elastomer film-glass slide (glass-elastomer-glass). DW-RICM observations provide the interference light intensities to accurately reconstruct the contact area and the relative surface profile of interest. We capture the evolution of the gel surface right after placing the glass sphere on the underlying gel, unlike previous literature, which set aside contact pairs to relax residual stresses on the surface [53,134,135]. An external preload (here, the weight of the glass sphere) compressed the elastomer and gel films. The ratio of the contact radius (a) to the elastomer or gel film thickness (H) was ~ 3 or ~14 – 18, respectively, and the ratio of the glass sphere radius (R) to H is ~ 74 – 130. In either case, the ratio is greater than the ratio used for the conventional contact theories $(a/H$ or $R/H \sim 0)$. Nevertheless, the glass-elastomer-glass contact follows the conventional Hertz theory, like the glass-glass contact. In the glass-gel-glass contact, the indentation depth (D) is close to the gel film thickness after ~ 85 hr, forming a ridge at the contact boundary. In the early stage, the contact radii $(a_M$ and $a_L)$ and D (or the submerged depth (d)) increase due to the external compressive force. Due to the elastic restoring force, the displaced gel volume by the glass sphere creates the ridge above the unperturbed surface. The ridge height becomes nearly invariant as approximately half of the initial ridge height and scaled as $t^{-0.08}$ and the ridge width scaled as $t^{0.08}$. The absolute value of the exponents (0.08) is smaller than the exponent of the shear rheology model of the gel $(k = 0.59)$, implying that a single factor, viscoelasticity, does not predominate the system. The ridge evolution originates from the coupling effect of the external preload, finite-size effect, and viscoelasticity. The contact radius, indentation depth, and ridge height do not vary in the later stage, while the ridge width increases until the steady state.

The long-term dynamics of gel were not investigated in prior studies [41,50,53,54,58,155]. In most previous literature, the underlying gel film was prepared to have sufficient thickness to neglect the finite-thickness effect of the gel [41,53,155]. Jensen *et al.* found the liquid-phase separation in contact between micron-sized glass spheres and gel film, wherein the gravitational force was negligible. Hence, the curvature of the ridge was scaled with the elastocapillary length [53]. We found a similar liquid phase at the contact boundary. Karpitschka *et al*. developed a theoretical framework to analyze the wetting ridge based on the rheological models of gel [155]. The gel was in contact with a water droplet, and the surface stress was relaxed within the relaxation time (< 1 s). Cai *et al.* also investigated the contact between gel and water droplets on a scale smaller than the capillary length [156]. They found that the phase-separation of liquids occurred due to the balance between the elastic restoring force, surface tension, and osmotic pressure. Since they prepared a swollen gel using additional silicone oil, they analyzed the phase-separation using Flory-Huggins energy of mixing; this situation is different from our work as we did not add additional oil to the gel. Also, even though the mitigation of liquids occurs similar to our work, the contact angle of the ridge cusp (71.65 °) is far larger than ours, possibly due to the limited resolution of their system using fluorescent dyes.

The observations from our study may have profound implications for engineering silicone gels as well as hydrogels. Silicone gels and hydrogels are similar as they possess a dual-phase structure composed of free liquids in cross-linked networks, but they are different in the dynamic response to the external contact pressure. Hydrogels contain water as a liquid. The water molecules with a lower molecular weight (18 g/mol) are more responsive to external stimuli than heavy silicone molecules. Therefore, although different factors affect the contact behavior of gels, such as cross-link density and concentration of the solvent, in most cases, hydrogels would reach a steady state faster than silicone gels. For example, in fitting the Chasset-Thirion equation, polyacrylamide hydrogel with a similar elasticity (G: 1.1 kPa) to that of the silicone gel (G: 1.87 kPa) has a >100 times shorter intrinsic time scale of 1.87×10^{-4} s than the silicone gel's time scale of 0.09 s [154,157]. Also, hydrogels are more susceptible to compression and phase-separation of free liquids due to the higher compressibility and higher surface tension [158,159]. Our findings might be critical in developing novel pressure-sensitive adhesives for drug delivery, sensors, and suture-free wound closure patches. These adhesives possess a finite thickness and create significant adhesion without chemical bonding by wetting a surface at the molecular level under compressive pressure [121,139,160–162]. Similarly, our findings can provide invaluable insights into fabricating gel-based (silicone gel or hydrogel) soft robots with a particular functional enhancement in their adhesion [12,70,122–124,140,163]. In detail, the long-term evolution of the contact zone can affect the stability of the adhesive contact and the maximum adhesion force between gel surfaces and counter rigid surfaces [164]. Soft robots like climbing robots and grippers might come into contact with protrusions. Such surface asperities lead to intense indentation of gel-based soft robots. Understanding the contact mechanics of gels gives information on fatigue failure from intense expansion and contraction of the gel-based bodies of soft robots [165,166]. Analogies of mechanical properties between biological tissues and gels allow gels to be used instead of living cells to study tissue mechanics [1,14–17], which would enable the possibility of long-term observations due to the inertness of these gels. Macroscopic properties (*e.g.,* surface tension, elasticity, and viscosity of cells and cultivation conditions (*e.g.,* Petri dishes, culture media)) might help explain configurational changes of cells under the law of energy minimization, similar to the soft adhesion of gels.

Chapter 4

Reduced Pressure Drop in Viscoelastic Polydimethylsiloxane Wall Channels[†]

Polydimethylsiloxane (PDMS) is an important viscoelastic material that finds applications in a large number of engineering systems, particularly lab-on-chip microfluidic devices built with a flexible substrate. Channels made of PDMS, used for transporting analytes, are integral to these applications. The PDMS viscoelastic nature can induce additional hydrodynamic contributions at the soft wall/fluid interface compared to rigid walls. In this research, we investigated the pressure drop within PDMS channels bounded by rigid tubes (cellulose tubes). The bulging effect of the PDMS was limited by the rigid tubes under flowing fluids. The PDMS viscoelasticity was modulated by changing the ratio of base to crosslinker from 10:1 to 35:1. We observed the pressure drop of the flowing fluids decreased with the increased loss tangent of the PDMS in the examined laminar regime (Reynolds number (*Re*)~23-58.6 for water and *Re*~0.69-8.69 for glycerol solution). The elastic PDMS 10:1 wall channels followed the classical Hagen Poiseuille's equation, but the PDMS walls with lower crosslinker ratios and thicker walls decreased pressure drops. The friction factor (f) with the two working fluids is approximated as $f = 47/Re$. We provide a correlation between the pressure drop and PDMS viscoelasticity based on experimental findings. The research findings appear to be unexpected if only considering the energy dissipation of viscoelastic PDMS. We attributed the reduction in the pressure drop to a lubricating effect of the viscoelastic PDMS in the presence of the working fluids. Our results reveal the importance of the subtle diffusion of the residual oligomers and water from the bulk to the soft wall/fluid interface for the observed pressure drop in soft wall channels.

[†] This chapter is reproduced from A-Reum K., Sushanta K. M., and Boxin Z., "Reduced Pressure Drop in Viscoelastic Polydimethylsiloxane Wall Channels." *Langmuir*, 2021, vol. 37 (49). 1429-14301.

4.1 Introduction

Soft wall channels are of great interest in various research areas; they are actively being studied to improve mass transfer in laminar fluid flows and treat gels in channels to control friction and prevent biofilm formation (anti-biofouling) [6,178,179]. Soft wall channels with flowing fluids are also utilized as ideal flow models of cardiovascular systems for *in-vitro* studies, since the vessels in a human's body are made of viscoelastic tissues [20,180,181]. Soft wall channels are commonly made of soft polymers, which induce fluid-structure interactions due to the dynamic nature of these materials. Therefore, to design the most appropriate soft channels for each application, the viscoelasticity of soft polymers needs to be considered in addition to the conventional factors of fluidic channels such as the dimensions of the channel (hydraulic diameter and length), flow rate, and fluid characteristics [179,182–184].

Lahav *et al.* [183] investigated soft wall channels made of an aqueous polyacrylamide with a glass backing layer and found that the measured volumetric flow rate is lower than the calculated flow rate corresponding to a glass tube at the Reynolds number (Re) < 500. They attributed this observation to the oscillations of the soft wall under the continuous shear stress caused by the turbulent boundary layer near the wall. They introduced a correction factor to quantify the reduced volumetric flow rate, the degree of shear deformation: $\zeta = (D_G/4LG')\Delta P$, where D_G is the outer diameter of the soft wall, L is the channel length, ΔP is the pressure drop, and G' is the shear storage modulus. The material property of the soft wall and its thickness become critical in soft wall channels, unlike rigid channels. Nevertheless, the calculated volumetric flow rate with the correction factor α was still different from the experimental value. Krindel *et al.* [185] tested a wider range of Re ~ 20 – 4,000 using the soft wall channel introduced in ref [183]. They found that at the transition Re value, the flow rate depends on the geometric parameter (the ratio of the outer diameter to the average inner diameter = D_G/D_i). Yang *et al.* [182] provided a modified expression for the flow rate ratio, Q/Q_{rigid}, where Q and Q_{rigid} are the volumetric flow rate of a soft wall tube (measured value) and a rigid tube (calculated value), respectively, by considering the shear storage modulus and the pressure gradient.

They explained that the reduction of volumetric flow rate, which was observed in refs. [183,185] , is caused by the kinetic energy end effects from the underdeveloped flows within a resultant tapered channel geometry.

In recent years several researchers have used polydimethylsiloxane (PDMS)-based soft wall channels and characterized the fluid flow in terms of flow transition and pressure drop. Verma *et al.* [186] compared rigid and soft wall channels with the same dimensions to determine the onset of flow instability at Re ~ 100 – 10,000. They found that the flow transition is caused not by the geometrical change but by the wall flexibility. The wall flexibility can lower the transition Re by up to 500 (G': 17 kPa) within channels of diameter 800 μm, with this change being proportional to $\Sigma^{5/8}$ (the dimensionless wall elasticity parameter, $\Sigma = \rho G' D_{avg}^2 / 4\eta^2$, where ρ and η are the density and dynamic viscosity of the test fluid, respectively). Raj M. *et al.* [179] examined the pressure drop in soft rectangular wall channels without a rigid backing layer for the range Re ~ 0 – 125. They observed the enlargement of the cross-section of the channel by the pressure inside. They provided a modified expression for the velocity profile considering the flexural deflection of the soft wall with a different width-to-thickness ratio. The resulting pressure drop was lower than in rigid channels. Gervais *et al.*[187] investigated PDMS-based rectangular channels without a rigid backing layer. PDMS had elasticities of 1 and 3 MPa. The authors found that the flow rate through the soft channels was higher than in the rigid channel, which is the opposite of refs. [183,185]. Also, the flow rate had a non-linear correlation with the applied pressure drop due to the expansion of the free wall of the channels.

The interior surface displacement of a soft coating in a rectangular rigid channel was investigated but mainly for turbulent flows. Benschop *et al.* [188] investigated the role of soft coating properties (*e.g.,* thickness, viscoelasticity) on the surface displacements. They studied three different soft coatings (G' ~ 1.38 – 14.59 kPa and the shear loss modulus, G'' ~ 0.38 – 0.8 kPa) and they found that the loss angle (δ, in the loss tangent, tan δ) of the soft coatings predominated the surface displacement when resonances occurred. Rosti *et al.* [189] investigated the drag penalties near the hyper-elastic soft surface using numerical simulations at *Re* = 2800. They found that the surface friction increased with the shear elasticity, but the role of the shear loss modulus was negligible. Thus, the surface displacement of the soft coating was mainly affected by the flowing fluids. The interactions between soft coatings and turbulent flow (an aqueous sodium iodide solution) were experimentally examined by Wang *et al.* [190] The surface displacement of the soft coating with a thickness of 5mm was imaged using interferometry. They observed an increased value of the skin-friction coefficient. However, an opposite trend of reduced skin friction has also been reported for a turbulent flow [23,191]. For instance, Choi *et al.* [23] tested soft walls with different elasticities of 1.7 and 2.8 MPa, and the loss tangent varied from 0.08 to 0.3. They found 7 % drag reduction at the flow velocity of 2 – 6 m/s because of the upward shift of the velocity profile in the flowing fluids and the resultant decrease in the momentum thickness of the boundary layer. Note that all the above studies used rigid rectangular channels with only one of the interior channel walls coated with soft materials and considered turbulent flow only.

In comparison with rigid channels, flowing fluids across the soft wall channels might lead to a lower pressure drop when the bulging effect of the soft wall predominated the system in the laminar regime or a higher pressure drop due to the wall oscillations or the drag friction of channels. The current understanding of the fluid flowing in soft channels is still very limited. This present research investigated the pressure drop in PDMS soft wall channels, where the wall deformation was limited by fabricating incompressible PDMS walls inside backing tubes (cellulose tubes). A series of experimental studies were performed to measure the pressure drop in the PDMS wall channels with different viscoelasticity of the PDMS walls (G':2.358 – 0.106 MPa and G'': 0.16 – 0.014 MPa) in the regime of laminar flow with negligible inertial influence. The PDMS viscoelasticity is modulated by adjusting the ratio of the PDMS base and the crosslinker from 10:1 to 35:1. We correlate the pressure drop reduction ratio to the loss tangent of PDMS walls. To the best of our knowledge, there have been no prior reports to directly relate the pressure drop to the viscoelasticity of the PDMS when the bulging effect is limited. By doing so, we circumvent the need for measuring the soft wall deformation, which has been the focus to date in quantifying the pressure drop in PDMS wall channels. According to the literature, we had expected an increased pressure drop of flowing fluids compared to rigid channels because of the oscillations of the PDMS wall as examined in refs.[186,192,193]. However, the measured pressure drop turned out to be lower than that of rigid channels, indicating that less energy is consumed across the soft wall channel in our fluidic system. The change in the cross-sectional area of the channels was not presented because the outer backing tube confined the deformation of the PDMS walls. Hence, the reduced pressure drop across the PDMS wall channels indicates a possible lubricating effect of the viscoelastic PDMS walls in the presence of the working fluids. This work provides insights towards a deeper understanding of the hydrodynamic behavior of the soft wall channels, aiding in developing soft wall channels.

4.2 Experimental

4.2.1 Channel Fabrication

PDMS (Sylgard 184 elastomer kit, Dow Corning) was used to fabricate soft walls inside the confinement tubes due to its easily adjustable material properties. The PDMS prepolymer was prepared by mixing base and curing agent at seven different weight ratios (10:1, 15:1, 20:1, 23:1, 25:1, 30:1, and 35:1) using a planetary mixer (ARE-310, Thinky Corporation) for 15 minutes. After degassing the silicone mixture in a vacuum chamber for 40 minutes, it was poured into rigid cellulose tubes (inner diameters: 3.175 mm and 6.35 mm; length: 40 mm) with hardness R78 and tensile strength of 43.44 MPa (8565K33, McMaster-Carr). The use of two different diameter tubes produced two different thicknesses of the soft channel walls, *viz.*, 1.334 mm and 2.921 mm, respectively. The length of the channel was designed to be longer than the hydrodynamic entry length (0.015 – 1.5 mm). A 25 G needle (outer diameter: 0.508 mm) was positioned concentrically inside the cellulose tube as a template. Then both ends of the tube were sealed with caps. The tube

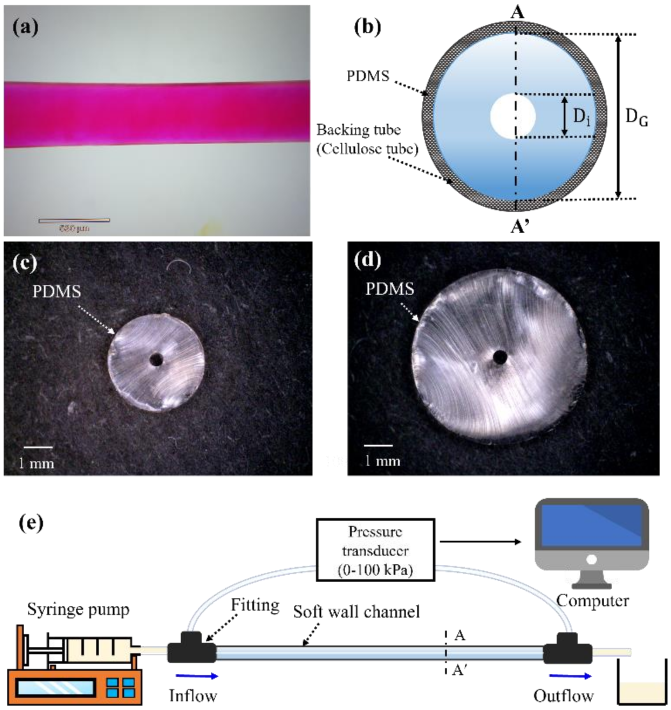

Figure 4.1 Fabrication of PDMS soft wall channels and experimental set-up. (a) An image of a PDMS 10:1 channel showing the flow of DI water mixed with a red dye (scale bar: 530 μm). **(b)** A schematic of the cross-sectional view (A-A′) of the soft wall channel, where D_i = 0.5 mm and D_G = 3.175 mm and 6.35 mm, respectively. Cross-sectional views of PDMS 10:1 soft wall channel with **(c)** 1.334 mm and **(d)** 2.921 mm wall thickness (scale bar: 1 mm). **(e)** A schematic view of the fluidic system with soft wall channel: the pressure drop across the soft wall channel is measured using a pressure transducer at a constant flow rate. The outlet is open to the atmosphere.

filled with PDMS prepolymer was stored at room temperature for 12 hours and then cured at 80 °C for ~ 24 hours. After fully curing the PDMS, the needle was pulled out, and then DI water was injected through the channel to prevent the channel from collapsing due to cohesion. For PDMS with low concentrations of cross-linking agent, we froze the channel at –18 °C for 15 minutes, then pulled the needle out. A microscopic image of the soft wall channel and a schematic cross-sectional view of the soft wall channel are given in Figures 4.1(a) and (b), respectively. Figures 4.1(c) and (d) are the cross-sectional views of soft walls without the cellulose tubes. DI water was filled through the fabricated channels for 4 days to equilibrate any potential surface changes during testing.

4.2.2 Viscoelasticity of PDMS

The shear modulus was measured by a TA Q800 Dynamic Mechanical Analyzer (DMA, TA instruments) at 25 °C. PDMS films were cast in a petri dish and then cut into rectangular shapes with dimensions 40 mm (L)×10 mm (W)×1 mm (T). The analysis was carried out using Multi-frequency-strain mode at 0.1 – 15.8 Hz. A 0.01 N preload was applied to the PDMS where the PDMS are in a linear-viscoelastic region (LVE). The measurements were repeated four times.

4.2.3 Surface Roughness of Soft Wall

We measured the soft walls and needles' roughness using a 3D measuring laser microscope OLS5000. The arithmetic mean derivation (R_a) of PDMS walls and needles were 0.256 ± 0.01 μm and 0.15 ± 0.05 μm, respectively. Thus, the ratio of the average roughness and the inner diameter is ~ 0.0005 in all our tests, which is negligible on the pressure drop measurements.

4.2.4 Pressure Drop Measurements

A differential pressure transducer (Omega, PX409-005DWUV) was used for measuring the pressure difference between the inlet and outlet of the soft wall channel at the sampling rate of 260 Hz (Fig. 4.1 (e)). The pressure transducer was connected to a data acquisition system (cDAQ-9171, National Instruments) linked to an analog voltage and current sensing module (NI-9207, National Instruments). The sensing module was interfaced with the PC running NI Measurement & Automation Explorer (NI MAX, National Instrument) software. The pressure drop measurement using the current set-up is capable of three decimal place accuracies. Constant flow rates (0.1 – 1.25 ml/min.) were generated to attain laminar flow (*Re*: 0.69 – 58.6) with a syringe pump (Nexus Fusion 4000, Chemyx). The low range of Reynolds number was selected to focus on the role of viscoelastic soft walls on the pressure drop without generating the transient or turbulent flows. Due to the working principle of the syringe pump, back pressure could be caused in the flowing fluid, which is exerted from the resistance of a liquid against the forward motion[194]. To minimize this back pressure and create a stable and constant flow rate, we used syringes with a large inner diameter (58.4 mm) and attached a rubber plunger that fits tightly in the syringe. Also, while testing, the syringe pump did not stall, which indicates that the syringe pump did not reach the programmed maximum back pressure of 107.94 kPa. Here, *Re* is calculated using the following definition $Re = \rho V D_i/\eta$, where V is the flow velocity. For all experiments, DI water (η: 0.89 mPa·s, ρ: 996.89 kg/m^3)[115] and water-glycerol mixture (47.5 v/v % glycerol, η: viscosity: 6.85 mPa·s, ρ: 1140 kg/m^3) were employed. The 47.5 v/v % glycerol viscosity was measured with a dynamic shear rheometer (Kinexus Rotational Rheometer, Malvern Instruments) from 0.01 to 100 shear rate at 25 °C. Three to four individual channels with the same mixing ratio were tested at a 0.1 – 1.25 ml/min constant flow rate. The outlet of the channel was open to the atmosphere (Figure 4.1(e)).

4.3 Results and Discussion

4.3.1 Viscoelasticity of PDMS

Seven different mixing ratios of PDMS base and crosslinker were used to fabricate the soft wall channels. The cross-linking density decreases with decreasing the crosslinker, leaving more (partially) un-crosslinked polymers in the cross-linked networks. A list of the fabricated PDMS and their viscoelastic parameters are tabulated in Table 4.1. The shear storage (G') and loss modulus (G'') were measured using the DMA, and the loss tangent was calculated using the measured shear storage and loss modulus, according to $tan\delta = G''/G'$. The parameter δ is in radians, indicating phase lag between the applied shear strain and the resulting shear stress. From this point, PDMS 10:1, 15:1, 20:1, 23:1, 25:1. 30:1 and 35:1 are abbreviated as P10, P15, P20, P23, P25, P30, and P35, respectively. The shear storage and loss modulus decrease by decreasing the concentration of the crosslinker in the mixture while the loss tangent increases.

4.3.2 Pressure Drop Determination

Flowing fluids across the channel encounter a sudden contraction and expansion, *i.e.,* minor losses (Fig. 4.2). The inner diameters of the soft wall channel and fittings are 0.5 mm and 4.926 mm, respectively. The pressure drop from the minor losses is calculated as [195]:

$$P_{loss} = \frac{\rho V^2}{2}\left(\sum_i K_{L,i}\right) \tag{4.1}$$

Table 4.1 The viscoelastic properties of PDMS with the different ratios of base and crosslinker.

	P10	**P15**	**P20**	**P23**	**P25**	**P30**	**P35**
$\boldsymbol{G'}$ **(MPa)**	2.358	0.797	0.727	0.362	0.341	0.239	0.106
$\boldsymbol{G''}$ **(MPa)**	0.160	0.066	0.065	0.033	0.033	0.025	0.014
$\boldsymbol{tan\ \delta}$	0.068	0.083	0.089	0.091	0.097	0.105	0.132

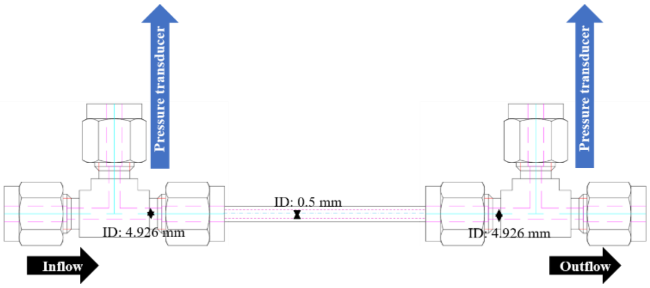

Figure 4.2 The cross-sectional view of the soft wall channel and the fittings: the inner diameter of fittings = 4.926 mm and the inner diameter of the channel = 0.508 mm.

where $K_{L,i}$ is the loss coefficient in a soft wall channel. For a sudden contraction and expansion, we use $K_{L,i}$= 0.5 and 1, respectively, referring to refs. [195,196]. The total minor losses are calculated to be in the range of 0.05 – 8.6 Pa, depending on the applied flow rate and fluids density. The final pressure drop is determined by deducting this calculated minor loss from the measured pressure drop. It is to be noted that the current set-up can reliably measure the pressure drop up to Re ~ 0.69 and 12 for the water and glycerol mixture as working fluids, respectively. When water is used as a working fluid, the pressure drop measured at Re < 12 is lower than the minimum limit of the pressure transducer, which is approximately 40 Pa.

4.3.3 Network Structures and Surface Wettability of PDMS

The surface wettability of the interior wall of soft wall channels can influence the pressure drop of flowing fluids through the soft wall channel. Hence, we looked into the possible lubricating effects of mobile and non-crosslinked monomers and oligomers at the contact interface between the soft interior wall and flowing fluids. P10 has a higher cross-linking density with a lower mobile component fraction than P35 (Fig. 4.3). Even after fully curing, 5 wt. % and 33 wt. % of the residual un-crosslinked oligomers were left in the P10 and P35 networks, respectively, as measured by solvent extraction (see Fig. C.4.2). The un-crosslinked oligomers are mobile in the network, leading to the lower shear modulus and the higher loss tangent. The untethered free oligomer with low molecular weight tends to migrate to the air-PDMS interface. In addition to such freely diffusive oligomers, dangling chains (also called pendant chains) affect the surface properties of PDMS wherein one end is connected covalently to the network while the other end is free [53,131,197,198]. Such mobile components could play a role in lubricating the interface [3,197].

Furthermore, the diffusion of water through the PDMS wall might affect the frictional properties of the PDMS wall when water is used as a working fluid, as illustrated in Figure 4.3 ($\mathrm{P10_{water}}$ and $\mathrm{P35_{water}}$). The water diffusion was confirmed using flat PDMS films. After 4 days immersed in water, the surface and cut cross-section of PDMS films became opaque (Fig. C.4.3(a)), and the weight of P10 and P35 films increased by ~ 0.27 % and 0.29 %, respectively (Fig. C.4.3(b)). This diffusion of water in PDMS networks or similar organic polymeric materials has been reported in earlier research, attributed to a random thermal effect [199,200].

Static and dynamic contact angle (CA) analysis evaluated the influence of non-crosslinked components and the diffusion of water through the soft wall on the surface frictional properties. We prepared P10 and P35 films with the highest and lowest concentrations of the crosslinker, respectively, in three different conditions (bare: right after curing, air: left in air for 4 days, and water: immersed in water for 4 days) (Fig. 4.3). The detailed experimental conditions and results are given in Appendix C. P10 and P35 had the static CA, 115 ° and 130 °, respectively (see Fig. C.4.4(a)) [201]. However, P35 had significantly lower receding CAs, on average 55 °, than P10; but the advancing CA of P35 was higher ~ 16 ° than that of P10 (Figs. C.4.4 and 5). The static and dynamic CAs of P10 correspond to the values given in [202,203]. This implies that soft wall channels made of P35 are substantially more hydrophilic than P10 because of the diffusion of water into P35, which might reduce the interfacial friction between the interior wall of P35 and flowing water [201].

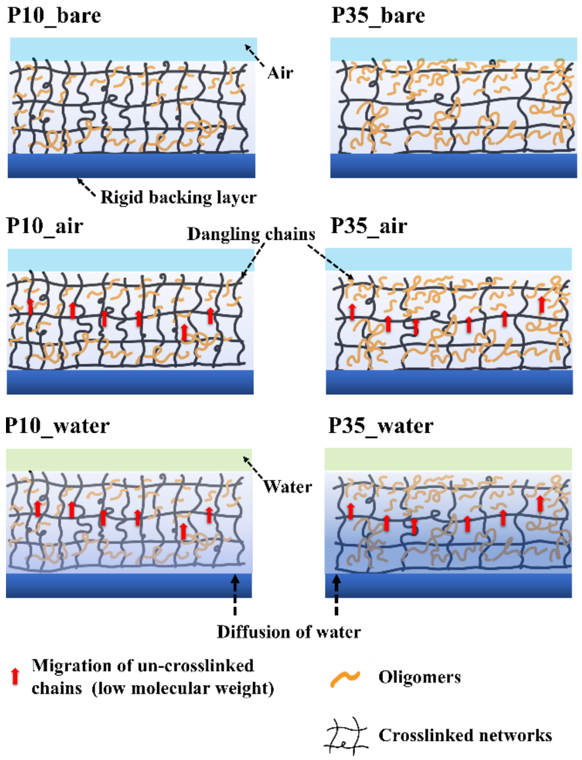

Figure 4.3 Schematics of P10 and P35 network structures in three conditions: right after curing (P10$_{\text{bare}}$ and P35$_{\text{bare}}$), left in air for 4 days (P10$_{\text{air}}$ and P35$_{\text{air}}$), and submerged in water for 4 days (P10$_{\text{water}}$ and P35$_{\text{water}}$). The top surface is exposed to the air or water, and the bottom surface is attached to a rigid backing layer. P35 has more free oligomers and dangling chains due to the smaller amount of the crosslinker. In P10/P35$_{\text{air}}$ and P10/P35$_{\text{water}}$, free oligomers migrate to the air/water-PDMS interface. In P10$_{\text{water}}$ and P35$_{\text{water}}$, diffusion of water occurs.

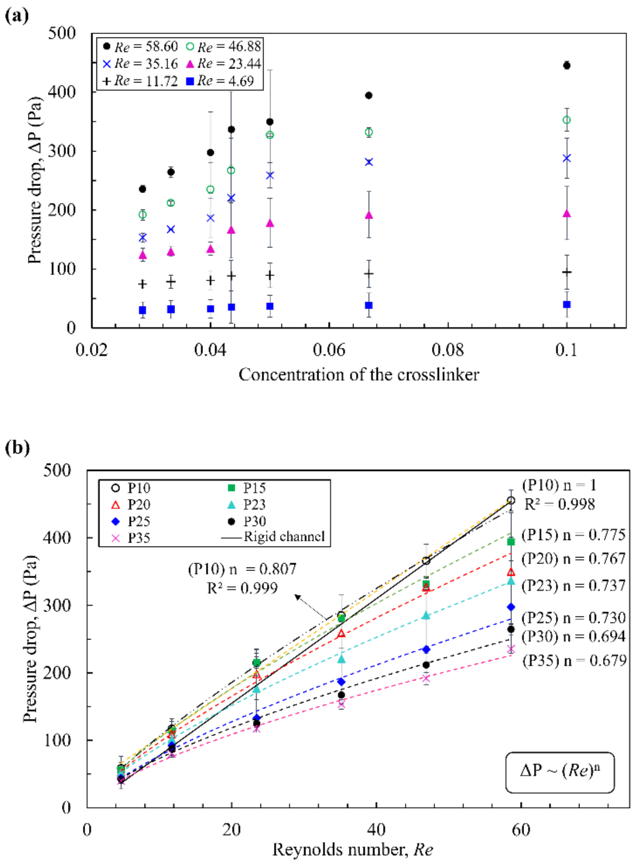

Figure 4.4 The pressure drops of liquid water in the soft wall channel (soft wall thickness: 1.334 mm): as a function of **(a)** the crosslinker concentration and **(b)** the Reynolds number (*Re*). The trend lines in **(b)** indicate the power law fitting, except in case for the rigid channel and P10 channel in **(b)**. The black solid line in **(b)** indicates the pressure drop corresponding to Hagen Poiseuille's equation (solid wall channel). The linear trend line (orange dotted line) of P10 in **(b)** is based on a linear fitting, suggesting its similarity with the solid wall channel. Error bars are the standard deviations of three to four measurements.

4.3.4 Effect of Viscoelasticity on the Pressure Drop

The pressure drop ΔP along the flow channel with soft wall thickness 1.334 mm is plotted against the corresponding crosslinker concentration and *Re*, respectively, in Figure 4.4. The error bars in Figure 4.4 are the standard deviations of the experimental results about the mean value. An abrupt change of the pressure drop near 0.04 concentration of the crosslinker, corresponding to P23 and P25, was observed, indicating a possible change in the polymer network where the polymer chains start to form a fully-connected network instead of a loose network. The P10 soft wall channel has the highest pressure drop, which is close to the calculated value for a rigid channel using Hagen Poiseuille's equation $\{\Delta P = (64/Re)(L/D_i)(\rho V_{avg}^2)/2 = (32\mu^2 L/\rho D_i^3)Re\}$ (the solid black line in Fig. 4.4(b)). We measured the volumetric flow rate at the outlet to calculate the outlet velocity (see Fig. C.4.1). The inlet velocity was calculated based on the inlet diameter of the soft wall channel and the applied volumetric flow rate. In the following analysis, we used the initial flow velocity as the average velocity (V_{avg}) because the outlet and inlet flow rates were almost the same (See Appendix C).

As mentioned earlier, in the case of water, the data corresponding to $Re < 12$ may not be reliable due to the limited measurable range of the pressure transducer. However, at $Re \geq 12$, the observed pressure drops in P10 channels match well with the calculated pressure drop (solid black line). Also, even at $Re < 12$, the calculated pressure drop is still within the standard deviations of the measured pressure drop across the P10 channels. Therefore, herein, we have kept our discussions for values corresponding to $Re \geq 12$ for water in our subsequent analyses. However, for glycerol, the data collected are applicable for *Re* up to 0.69.

The pressure drop in the P10 channels has $R^2 = 0.998$ for a linear (n = 1) fit with *Re*; for all other soft channels, the pressure drop ΔP is proportional to $(Re)^n$ where n is the power index, whose values are provided in Figure 4.4(b) for different ratios of the crosslinker. Based on literature [179,184,187,204] and our observations, P10 is considered a rigid channel, and the other channels are regarded as soft wall channels. The pressure drop decreases gradually from P10 to P35, showing a non-linear dependence of the pressure drops on Re (n < 1). The power index decreases from 0.775 to 0.679 as the crosslinker concentration decreases from P15 to P35. On average, the power fitting curves for P15 – P35 soft wall channels have $R^2 = 0.996$. In refs.[186,192,193], an opposite trend was reported, as mentioned earlier. Fluids flowing across soft wall channels might consume more energy than rigid channels when the oscillations of soft walls are caused by a sufficiently low elasticity and the high shear stress from flowing fluids, where the transition from laminar flow to turbulent flow occurs. However, the wall oscillations might not be dominant factors in our current because we measured the pressure drop within the laminar regime. There are significant effects of mobile oligomers and water diffusion, as discussed before.

The measured pressure drops in Figure 4.4 are converted to the scaled pressure drop ($P^* = \Delta PL/\eta$) and then re-plotted against the corresponding viscoelastic properties (the shear storage modulus, the shear loss modulus, and the loss tangent) in Figure 4.5. All the data collapse onto a single trend line in Figure 4.5. For P10 (rigid channel), the calculated scaled pressure drop (P^*) is 198,400. The scaled pressure drop is proportional to $G'^{0.191}$ and $G''^{0.238}$ with $R^2 = 0.833$ and $R^2 = 0.82$, respectively. However, the loss tangent is inversely proportional to the scaled pressure drop with an exponent of – 0.9 and $R^2 = 0.84$. By introducing the loss tangent as the horizontal axis (see Fig. 4.5(c)), we demonstrated the combined influence of soft walls' elastic and viscous properties on the pressure drop. There are some overlaps among the pressure drops between P23 and P25 (Figs. C.4.5(a) and (b)) due to the slight difference ($\sim$ 0.02 MPa) in the shear storage modulus and the shear loss modulus. This small difference is not from the limitation of the DMA because the minimum measurable modulus of the DMA is as low as 1 kPa. Since the shear storage modulus and the shear loss modulus change together as the concentration of the crosslinker in the PDMS is tuned, it might be reasonable to use the loss tangent to represent the combined effect of the storage modulus and loss modulus on the pressure drop.

Note that the reduced pressure drop of flowing fluids across the soft wall channels was often attributed to the flexural deformation of the soft walls [20,179,180,184,187]. However, the studied soft wall channels are made of PDMS, an incompressible rubber (ν ~ 0.5) [150,192,205], and the PDMS soft wall channels are fabricated within a cellulose backing tube. Therefore, no noticeable deformation of the soft wall was observed under flowing fluids (see Appendix Fig. C.4.6). Such conditions enable us to focus on the viscoelasticity of soft walls on the pressure drop. In refs.[183,185], soft channels with a glass backing tube were fabricated. However, the authors used polyacrylamide gel-based soft wall channels. The hydrogel is easily deformable, with a low Poisson's ratio ~ 0.457 [158]. To make the argument clear, we considered the case when P35 is assumed compressible (ν < 0.5) and calculated the corresponding wall deformation for the measured pressure drop to compare the experimental observations. The pressure drops of a rigid channel (calculated) and P35 (measured) are 453.978 Pa and 235.456 Pa, respectively. The pressure drop is calculated as:

$$\Delta P = \frac{128\mu Q L}{\pi D_{avg}^{4}} \tag{4.2}$$

where D_{avg} is the average inner diameter of the channel as a function of the length of the channel. Therefore, the normalized diameter of P35 channels can be written as $\Delta P_{rigid}/\Delta P_{P35} = \left(D_{P35}/D_{rigid}\right)^{\frac{1}{4}} = 1.178$ where D_{P35} and D_{rigid} are the average inner diameters of P35 soft channel, and a rigid channel, respectively. This normalized ratio is relatively higher than the observations given by R. Neelamegam, *et al* [193]. The authors found that the highest deformation ratio of the inner diameter is only 1.03 near the inlet of a tapered channel at *Re* = 500. On average, the ratio is ~ 1.01, which is a function of the length of the channel. This normalized ratio is significantly small considering that they did not have any rigid backing layer of soft wall channels. The shear storage modulus of the studied soft walls was 21 – 608 kPa.

As a result, in this work, the reduced pressure drop in the soft wall channels unlikely originated from the deformation of the soft walls, and the role of viscoelasticity might have dominated the reduced pressure drop.

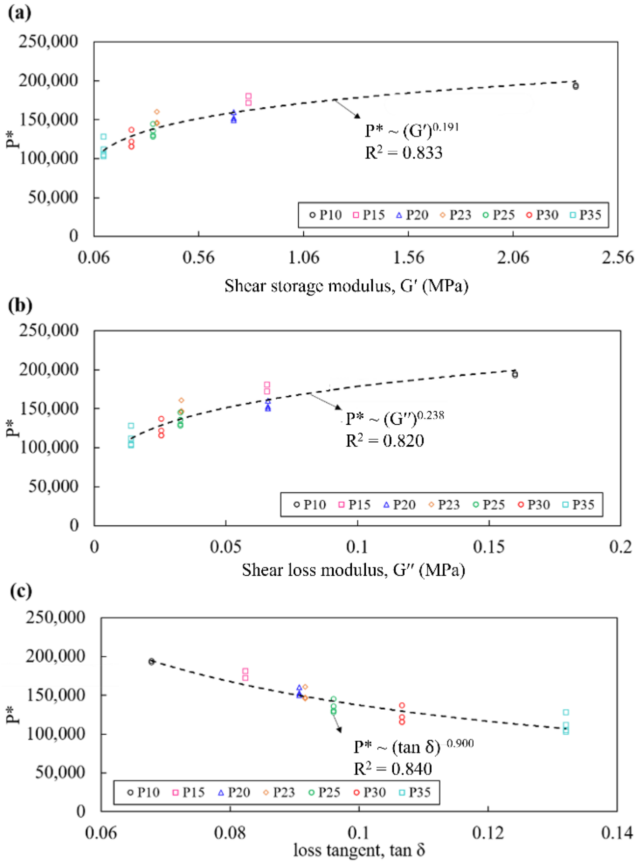

Figure 4.5 The scaled pressure drop ($P*$) of liquid water in the soft wall channel (soft wall thickness: 1.334 mm): as a function of **(a)** the shear storage modulus (G'), **(b)** the shear loss modulus (G''), and **(c)** the loss tangent ($tan\ \delta$). Each experimental condition was repeated 3 – 4 times. Error bars are omitted to improve readability of the data.

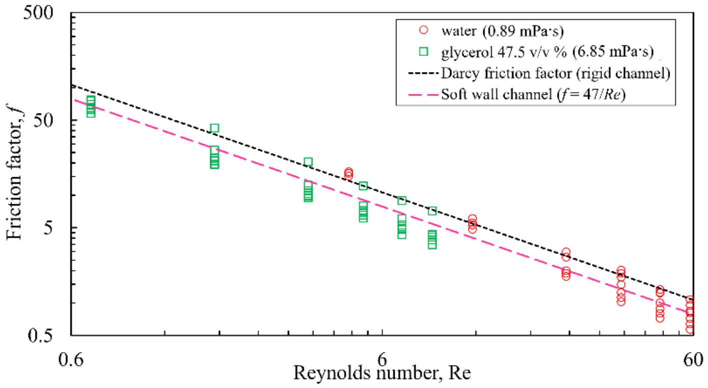

Figure 4.6 The friction factor (*f*) of the PDMS wall channel (the PDMS wall thickness: 1.334 mm) with flowing DI water and 47.5 v/v% glycerol *vs.* the Reynolds number (*Re*) in a log-log scale. The black dotted line indicates the theoretical Darcy friction factor, and the magenta dotted line is the fitting between *f* and *Re* in soft wall channels with two working fluids. Error bars are not presented together to improve readability of the data.

4.3.5 Effect of Fluid Viscosity on the Friction Factor

In addition to liquid water (η: 0.89 mPa·s), we have also tested a 47.5 v/v % glycerol mixed in DI water (η: 6.85 mPa·s) as the working fluid to achieve smaller *Re* (~ 0.6). Figure 4.6 shows the friction factor (*f*) of the soft wall channels at each *Re*. The friction factor of soft wall channels is calculated by rearranging the measured pressure drop into the following form:

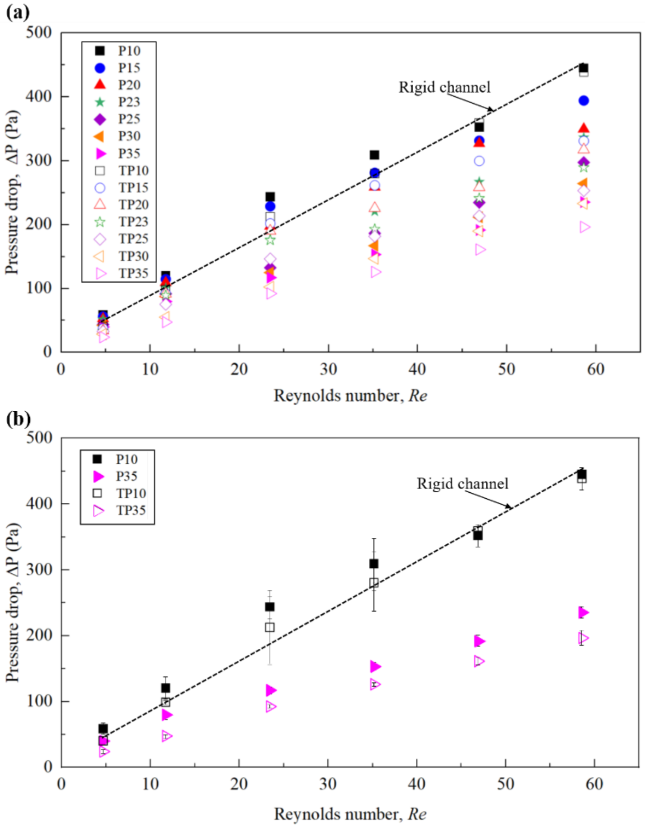

Figure 4.7 The influence of two different wall thickness (P10 – P35 with thickness 1.334 mm and TP10 - TP35 with thickness 2.921 mm): the pressure drop ΔP *vs.* the Reynolds number (*Re*) **(a)** in the PDMS wall channels with seven different mixing ratios and **(b)** in the PDMS channels with two different mixing ratios (P10/TP10 and P35/TP35). The black dotted lines indicate the calculated value of the pressure drop corresponding to a rigid channel using Hagen Poiseuille’s equation.

$$f = \frac{2\Delta P D_i}{L\rho V_{avg}^2} \tag{4.3}$$

which is valid for all types of fully developed internal flows in a rigid tube [195]. The dotted line in Figure 4.6 is the Darcy friction factor, $f = 64/Re$ which corresponds to a fully developed laminar flow in a circular rigid tube. For soft wall channels, the friction factor is overall lower than the Darcy friction factor. The friction factor with the two working fluids in the PDMS wall channel is fitted with $f = a/Re$ where a is the fitting coefficient. a is approximated as 47 with 95 % confidence bounds (the magenta dotted line); that is $f = 47/Re$. The fitting is based on the seven different mixing ratios of PDMS. It is to be noted that this new friction factor correlation is not a universal one, as we have tested with only two different viscosities of the working fluids. Nevertheless, we demonstrate a decrease in the pressure drop across the soft wall channels compared to their rigid counterparts through this correlation. Similar experimental results, the reduction in the friction factor, were reported in hydrogel-based soft wall channels with a glass backing tube [185]. On the other hand, in soft channels without confinement, the friction factor was higher than the Darcy friction factor due to the deformation of the inner diameter [186].

4.3.6 Effect of Soft Wall Thickness on the Pressure Drop

The pressure drop in PDMS soft wall channels with different PDMS wall thicknesses, *viz.*, 1.334 mm, and 2.921 mm, is plotted against Re (Fig. 4.7). Soft wall channels with a wall thickness of 2.921 mm are labelled as TP10, TP15, TP20, TP23, TP25, TP30, and TP35 to distinguish them from the channels with a wall thickness of 1.334 mm (P10 – P35).

P10 channels present almost the same pressure drop as the rigid channel regardless of wall thickness, as demonstrated in other literature[184,193]. In Figure 4.7, the theoretical pressure drop in a rigid tube (the black dotted lines) is within the range of the standard deviations of the measured pressure drop in the P10 channels. However, as the ratio of the curing agent decreases and the soft wall thickness increases, the pressure drop deviates more from the P10 (rigid channel). On average, between P15 and TP15, the pressure drop reduces by 15%, but this reduction increases to almost 25% as the weight ratio of base to curing agent is adjusted to 35:1. By comparing P10 and P35, it is clear that TP35 induces a lower pressure drop than P35 instead of comparing P10 and TP10 (Fig. 4.7(b)).

4.3.7 Correlation of the Pressure Drop

In the above sections, we have examined how the pressure drop is affected by the fluid viscosity (η), shear modulus (G', G''), the outer and inner diameters of the soft wall (D_G, D_i), and the flow velocity (V). Here, we examined their combined effect on the pressure drop reduction ratio ($\Delta P/(\Delta P_{rigid}$) as a function described below, using dimensional analysis.

$$\frac{\Delta P}{\Delta P_{rigid}} = f(\eta, G', G'', D_G, D_i, V) \tag{4.4}$$

The dimensionless forms of the key parameters in Eq. (4.4) are tabulated in Table 4.2, in terms of the three basic dimensions, mass (M), length (L), and time (T).

Table 4.2 Dimensions of dependent and independent variables.

$\left[\frac{\Delta P}{\Delta P_{rigid}}\right]$	$[\eta]$	$[G']$	$[G"]$	$[D_G]$	$[D_i]$	$[V]$
$M^0L^0T^0$	$ML^{-1}T^{-1}$	$ML^{-1}T^{-2}$	$ML^{-1}T^{-2}$	$M^0L^1T^0$	$M^0L^1T^0$	M^0LT^{-1}

The shear storage modulus, the inner diameter, and the fluid velocity are selected as the core variables. We found three dimensionless groups, *i.e.*, the three scaled forms of the fluid viscosity, the shear loss modulus, and the outer diameter of PDMS walls:

$$\frac{\Delta P}{\Delta P_{rigid}} = f(\eta^*, G''^*, D_G^*) = f\left(\frac{V}{G'D_i}, \frac{G''}{G'}, \frac{D_G}{D_i}\right) \tag{4.5}$$

Here, the scaled form of the fluid viscosity $\left(\frac{\eta V}{G'D_i}\right)$ is the dimensionless stress (τ)[178,206]. The dimensionless term of the shear loss modulus $\left(\frac{G''}{G'}\right)$ is the loss tangent *$(tan\ \delta)$* of the PDMS walls. The last term $\left(\frac{D_G}{D_i}\right)$ is the thickness ratio between the outer and inner diameter of the PDMS walls. Through multiple linear regression (MLR), a quantitative expression that relates the pressure drop reduction ratio to the independent variables is statistically found (with $R^2 = 0.8$), which can be expressed as:

$$\begin{aligned}\frac{\Delta P}{\Delta P_{rigid}} &= 0.053\left(\frac{\eta V}{G'D_i}\right)^{-0.1339}\left(\frac{D_G}{D_i}\right)^{-0.1618}\left(\frac{G''}{G'}\right)^{-0.391} \\ &= \frac{0.053}{\tau^{0.1339}\left(\frac{D_G}{D_i}\right)^{0.1618} tan\ \delta^{0.391}}\end{aligned} \tag{4.6}$$

To study the applicable range of the correlation, Eq. (4.6) is rewritten simply as:

$$\begin{aligned}\frac{\Delta P}{\Delta P_{rigid}} &= 0.053\left(\frac{\eta V}{G'D_i}\right)^{-A}\left(\frac{D_G}{D_i}\right)^{-B}\left(\frac{G''}{G'}\right)^{-C} \\ &= \frac{0.053(D_i)^{A+B}(G')^{A+C}}{(\eta V)^A(D_G)^B(G'')^C} = \left[\frac{0.053(D_i)^{A+B}}{(\eta V)^A(D_G)^B}\right]\left[\frac{(G')^A}{(tan\ \delta)^C}\right]\end{aligned} \tag{4.7}$$

where A = 0.1339, B = 0.1618, and C= 0.391. The plot between the experimental $\Delta P/\Delta P_{rigid}$ and the calculated $\Delta P/\Delta P_{rigid}$ using Eq. (4.7) is given in in Figure C.4.7. We discuss three limiting cases of the correlation presented in Eq. (4.7). These are: $D_G \gg D_i$, $G'' \gg G'$, and $G'' \ll G'$. Herein, we specify the applicable range of the correlation as $1.84 \leq D_G/D_i \leq 2.84$ based on the experimentally studied diameter ratio and discuss the pressure drop in each limit of D_G/D_i quantitatively. In the case of $D_G \gg D_i$, when the outer diameter becomes significantly thicker than the inner diameter, the soft wall can be considered an infinite medium. In that limit, the energy dissipation rate in soft wall channels could become independent of the diameter ratio and the wall material properties, as the energy dissipation is dominated by the flowing fluid [207]. Under such extreme conditions, the ratio $\Delta P/\Delta P_{rigid}$ will not approach zero. In the range of the diameter ratio that we experimentally examined; the soft wall thickness still plays a critical role in determining the pressure drop. In the case of $G'' \gg G'$ where $tan\ \delta \to \infty$, $\Delta P/\Delta P_{rigid}$ converges to zero according to Eq. (4.7). In this limit, the soft wall behaves more like a viscous liquid than an elastic solid. Thus, it will be challenging to fabricate the soft wall channel and maintain a stable channel structure under flowing fluid. Furthermore, early onset of transition from laminar to turbulence could be demonstrated at the lower shear modulus because of dynamical instability at the fluid-wall interface (oscillations of the soft walls) [206,208,209], which is beyond the scope of this current study. For $G'' \ll G'$ where the soft wall loses viscous properties and becomes more rigid, $\Delta P/\Delta P_{rigid} = \infty/0 = \infty$ based on Eq. (4.7), indicating that the pressure drop in the soft wall channel is much higher than the rigid channel. This is opposite to what we have found experimentally. Therefore, we limit the applicable range of the correlation as $G'^{A}/tan\delta^{C} \leq 20.4$ obtained using the material properties of PDMS 10:1. In the case of $G'^{A}/tan\delta^{C} > 20.4$, when the channel is made of more rigid materials than P10, the pressure drop reduction ratio does not converge to 1 using Eq. (4.7). Therefore, one can conclude that this correlation is valid for $G'^{A}/tan\delta^{C} \leq 20.4$. Eq. (4.7) quantifies the relative influence of each parameter on the pressure drop reduction ratio. In particular, the loss tangent predominates the pressure drop reduction ratio with the highest value exponent at 0.391, following the experimental results.

4.3.8 Origin of the Reduced Pressure Drop

A reduced pressure drop of flowing fluids was experimentally observed in the viscoelastic PDMS wall channels, which means that less energy is dissipated in the fluidic system. The dimensionless analysis found that the loss tangent predominated the pressure drop reduction ratio; and the pressure drop decreased with the loss tangent. The decrease of pressure drop with the loss tangent is related to the un-crosslinked mobile molecules. The mobile molecules increase the loss tangent and might also induce a lubricating effect to reduce wall friction in fluidic channels. P35 has fewer cross-linked networks than P10, exposing more free monomers and oligomers, and dangling chains at the contact interface. Such mobile polymers have been considered as ‘the solvent’ or ‘the oil layer’ in literature [53,210,211] because of their lubricating ability. Untethered polymers can even migrate into the liquid in contact or transport to other contact surfaces [3,210]. Therefore, we could assume that the mobile free polymers work as a lubricating layer and reduce the pressure drop of flowing fluids across viscoelastic PDMS wall channels. This lubricating effect can also explain the lower pressure drop in PDMS wall channels with a thicker wall due to the relatively large amount of the free oligomers compared to the PDMS wall channels with a thinner wall. In addition to the lubricating nature of free oligomers on the surface, it was found that the P35 tends to absorb more water than P10, which in turn made the surface of P35 more hydrophilic, which further reduces the overall wall friction in our case.

4.4 Conclusions

PDMS wall channels fabricated inside rigid backing tubes have been used to study the role of viscoelasticity on the reduced pressure drop. Thus, the flexural deformation of the PDMS wall was prevented while maintaining a constant PDMS wall thickness under flowing fluids. PDMS walls with seven different mixing ratios of the base to crosslinker (PDMS 10:1 (P10) – PDMS 35:1 (P35)) were tested along with two

Newtonian fluids (DI water and 47.5 v/v % glycerol mixture) at varied flow rates (0.1 – 1.25 ml/min) within the laminar regime. P10 wall channels followed Hagen Poiseuille's law like a rigid channel. However, P15 – P35 presented reduced pressure drops. For a first approximation, the friction factor (f) is expressed as f = 47/Re for soft wall channels with the two working fluids as opposed to the well-known Darcy friction factor of 64/Re for rigid wall channels. Since the PDMS wall deformation was limited due to rigid backing tubes, we focused on the viscoelastic properties of the PDMS walls to investigate the origin of the reduced pressure drop in P15 – P35 wall channels. The scaled pressure drop is found to be proportional to (shear storage modulus, $(G')^{0.191}$), (shear loss modulus, $(G'')^{0.238}$), and (loss tangent, $(tan\ \delta)^{-0.9}$) using dimensionless analysis. The pressure drop variation with loss tangent is likely due to the dual roles of the un-crosslinked mobile molecules in soft PDMS walls, which increase the viscous component while inducing a lubricating effect, leading to the reduced pressure drop. The wetting experiments verified the lubricating effect, where a considerably lower receding contact angle of water droplets on P35 was observed compared to P10, especially when the PDMS surface is already wet. This higher wettability could lubricate the PDMS surface and reduce the wall friction. The correlation and the experimental observations could be exploited as a potential guideline to design soft wall channels, thereby broadening the practical application. For instance, our findings can be applied to investigate *in-vitro* studies of the vascular system because blood vessels are viscoelastic to sustain millions of cyclic motions in animal bodies. The typical elasticity of blood vessels is in the range of 0.2 – 3 MPa [181,212,213], which is close to the elasticity of PDMS in this study (0.1 – 2.4 MPa), and PDMS is also known to have similar hydrophobicity to vascular endothelial cells [214].

Chapter 5

Connecting Adhesion and Wetting with a Hydrogel Bridge[†]

Raindrops falling on windowpanes spread upon contact, whereas hail can cause dents or scratches on the same glass window upon contact. While the former phenomenon resembles classical wetting, the latter is dictated by contact and adhesion theories. The classical Young-Dupré law applies to the wetting of pure liquids on rigid solids, whereas conventional contact mechanics theories account for rigid-on-soft or soft-on-rigid contacts with small deformations in the elastic limit. However, the crossover between adhesion and wetting is yet to be fully resolved. The key lies in the study of soft-on-soft interactions with material properties intermediate between liquids and solids. In this work, we translate from adhesion to wetting by experimentally probing the static signature of hydrogels in contact with soft PDMS of varying elasticity of both the components. In doing so, we reveal previously unknown phenomenology and scaling law which smoothly bridges adhesion of glass spheres with total wetting of pure liquids.

[†] This chapter is reproduced from A-Reum K., Surjyasish M., Sudip S., Sushanta K. M., Boxin Z. “Connecting Adhesion and Wetting with a Hydrogel Bridge.” *Submitted.*

5.1 Introduction

Contact between two elastic surfaces dates back to the seminal work by Hertz elucidating the morphology of the contact zone [149]. Briefly, for two surfaces with radii, elastic moduli, and Poisson's ratios R_1, E_1, ν_1 and R_2, E_2, ν_2, the contact radius scales as, $a \sim (3RF/4E^*)^{1/3}$, where F is the applied load. Here, $R = (1/R_1 + 1/R_2)^{-1}$ and $E^* = [(1-\nu^2)/E_1 + (1-\nu^2)/E_2]^{-1}$ are the effective radius and effective elastic modulus, respectively (Hertz, 1882). Though Hertz theory successfully explains non-adhesive contacts, it fails where adhesion is present. Taking adhesion between the contacting surfaces into account, Johnson-Kendall-Roberts (JKR) [43] and Derjaguin–Muller–Toporov (DMT) [45] proposed modified theories with almost similar results. Considering adhesion, using JKR model, the modified contact radius can be expressed as $a \sim \left[(3R/4E^*)\left(F + 3\pi wR + \sqrt{6\pi wRF + (3\pi wR)^2}\right)\right]^{1/3}$, where $w = \gamma_1 + \gamma_2 - \gamma_{12}$ is the work of adhesion [43]. Here, γ_1 and γ_2 are the surface tensions of the individual contacting pairs, whereas γ_{12} is the interfacial tension. Both JKR and DMT theories have been successfully adopted to explain contacting surfaces [44,216–219]. However, they possess limitations too [54,216,217,220]. For contacting surfaces with large contact radius, the Maugis model has been found to provide more accurate description of the contact zone [220,221]. Further, recent experiments involving glass spheres on very soft gels have demonstrated how the JKR theory breaks down due to the dominant role of solid surface tension [44,54]. Also, soft gels in contact with a glass sphere can often undergo long-term deformation dynamics which disrupts our conventional understanding of contact mechanics [222]. It appears that a universal model is lacking to explain contact between any two surfaces.

On the other extreme, wetting of liquids [223–225] essentially corresponds to $E^* = 0$. Existing literature has attempted to bridge contact mechanics with a finite E^* to wetting with $E^* = 0$ using theoretical treatment [226–231]. However, the problem has been less explored experimentally. Most experiments consider rigid-on-soft [44,50,53,54,135,176,216,222,229–232] or soft-on-rigid [55,217,226,233,234] contacts. Hence, the effective elastic modulus $E^* = E_1/(1 - \nu_1{}^2)$ (or $E_2/(1 - \nu_2{}^2)$), *i.e.*, always becomes a function of only one of the elastic moduli, and thus fails to provide a holistic picture. Soft-on-soft systems provide the ideal playground to tune the effective elastic modulus E^*, taking into account elasticity of both the surfaces and provide an excellent platform to investigate the transition. At the same time, many biological [17] and artificial materials [234] represent soft-on-soft contact systems. Understanding such systems is key to interpreting natural phenomena like cell adhesion [13,14,17] as well as in developing advanced technologies like soft robotics [70,109,235], medical diagnostic chips [3], sensors [69,236], contact lenses, and artificial organs [109].

5.2 Experimental

5.2.1 Fabrication of Hydrogels and Soft Substrates

The chemicals used in this work were purchased from Sigma-Aldrich, if not specified. To synthesize hydrogels, we used acrylamide (AAm) as a monomer, N,N'-Methylene-bis-acrylamide (BIS) as the crosslinker, and 2,4,6-tri-methyl benzoyl- diphenylphosphine oxide (TPO) nanoparticle as the initiator. TPO nanoparticles were synthesized by dissolving 2.5 wt. % of diphenyl (2,4,6-trimethylbenzoyl) phosphine oxide (M_w = 348.48), 3.75 wt. % of polyvinylpyrrolidone, and 3.75 wt. % of dodecyl surface sodium salt (SDS) in DI water. After mixing the ingredients with a sonicator for 5 min at 95 °C, we obtained 10 wt. % of TPO nanoparticles in DI water. Pregel solutions were prepared by diluting the monomer (2.5 – 13 wt.%), 1 wt.% of the crosslinker (based on the monomer), and 2.5 wt. % of TPO nanoparticles (based on the monomer) in 0.5 mM $NaIO_4$ solution (oxygen scavenger). The hydrogel beads were prepared by suspending 4 μL of the pregel solution in a beaker containing n-octane and a silicone oil (phenylmethylsiloxane-dimethylsiloxane copolymer, 500 cSt, Gelest). The volume ratio between n-octane and the silicone oil is maintained as 1:2. Spherical shapes of the hydrogel were achieved due to the density gradient between n-octane (density ρ = 0.71 g/cm^3) and the silicone oil (ρ = 1.08 g/cm^3). Each pregel solution was exposed to UV light (~ 365 nm) for 20 min. The cured hydrogel beads were washed with heptane multiple times before each use.

Soft substrates were prepared using polydimethylsiloxane (PDMS, Sylgard 184 and Sylgard 527). First, the base and curing agent of Sylgard 184 and 527 were mixed in the weight ratio of 10:1 and 1:1, respectively as per manufacturer specifications. Consequently, each prepolymer of Sylgard 184 (10:1) and Sylgard 527 (1:1) were mixed together in different weight ratios of 1:0, 1.5:1, 1:1, 1:4, 1:15, and 0:1 to modulate the elastic properties. The mixture was then thoroughly stirred, vacuumed to eliminate trapped bubbles, and cured at 85 ˚C for 12 hours and then kept at room temperature for 2 hours before each use. Using this technique, we prepared 2 mm-thick-soft substrates by controlling the prepolymer volume in a petri dish. Mixing Sylgard 184 (10:1) and 527 (1:1) maintained the stoichiometry of each PDMS while decreasing the elastic modulus from a few MPa to kPa. Alternatively, to decrease the elastic modulus, a lower curing agent ratio of each PDMS can be used. However, this method might leave a significant free non-crosslinked PDMS, creating an oil layer on the PDMS surface.

5.2.2 Characterization of Hydrogels and Soft Substrates

For rheology measurements, each PAAm hydrogel and silicone gel was polymerized in a 60 mm-diameter-petri dish with a thickness of 2 mm. Detailed fabrication steps are illustrated in the previous section. The cured hydrogels and silicone gels were cut into 25 mm-diameter using a cutter. The shear storage and loss modulus of the materials were measured by performing a frequency sweep test on a dynamic shear rheometer (AR 2000, TA Instruments) from 0.01 to 100 Hz at a strain rate of 1 % and a normal force of 1 N (see Appendix. Figs. D.5.4-6). A constant temperature was maintained at 25◦C, and the test adopter is a 25 mm diameter plate. The measurement is taken after waiting for 10 min to stabilize the polymer. Each measurement was repeated three times.

The shear viscosity of PAAm 2.5 wt.% was analyzed from 0.01 to 100 Hz using a dynamic shear rheometer (Kinexus Rotational Rheometer, Malvern Instruments) at 25◦C. Since the monomer ratio was very low, the cured PAAm 2.5 wt. % was still liquid, having less than 1 Pa of the shear storage modulus. As a result, we measured the shear viscosity of PAAm 2.5 wt.% instead of the shear elasticities like other hydrogels. A cup and bob geometry (C14:CP14) was used, with a rotating cylinder inserted inside the cup. The cured hydrogel was poured into the geometry, and then the temperature was equilibrated for 5 min before testing. The shear rates from 0.01 to 100 Hz were applied. The measurement was repeated three times.

The surface tension of each prepolymer solution was measured using the pendant drop method under ambient condition of 25°C on a drop-shape analyzer (Krüss, DSA30). The droplet volume was increased using at the tip of a needle (diameter: 0.8 mm) right before it dropped. The surface tension was measured based on the Young-Laplace equation programmed on the ADVANCE software (Krüss, DSA30). Each measurement was repeated three times (Appendix Table. D.5.1). The surface energy of silicone gel was assumed to be equal to the measured surface tension of silicone prepolymer because of the small strain.

Further, we examined the effect of plasma treatment on PDMS surface roughness using atomic force microscopy (AFM) (MFP-3D BIO, Asylum Research). Each PDMS substrate was prepared as mentioned earlier, and treated with air plasma for 5 min. For comparison, the surface roughness of pristine PDMS and bare glass slide were also measured. The average root mean square height (R_q) and arithmetic mean roughness (R_a) of a bare glass slide are 0.54 ± 0.01 nm and 0.43 ± 0.01 nm, respectively. Representative AFM results of plasma-treated PDMS with the elasticity 6855 kPa are shown in Appendix Figure D.5.7. On average, R_q and R_a of PDMS are 0.48 ± 0.05 nm and 0.31 ± 0.03 nm before air-plasma, respectively. After air plasma treatment, R_q and R_a values increase marginally as 0.66 ± 0.03 nm and 0.52 ± 0.03 nm, respectively.

Lastly, we probe any possible diffusion between hydrogels and PDMS. The potential diffusion effect of PAAm hydrogel into PDMS substrate was examined under a Tensor 27 Attenuated Total Reflectance-Fourier Transformed Infrared (ATR-FTIR) spectrometer (Bruker). The measurements were obtained at a 1.92 cm^{-1} resolution from 124 scans. We placed 2 mm thick, cured hydrogel films ($E_1 = 106.65$ kPa) on 2 mm thick PDMS substrates ($E_2 = 3$ kPa and $E_2 = 6855$ kPa). After 1 hour, we removed the hydrogel films and cut the PDMS substrates to scan the cross-section of the PDMS. The FTIR spectra were collected at the nearest section of the surface where the hydrogel film was in contact. Regardless of the hydrogel contact, all the spectra overlap (Fig. D.5.8). As shown in Fig. D.5.8, the main absorption peaks of PDMS were observed at wavenumber of 2964 cm^{-1} (C-H stretching in CH_3), 1257 cm^{-1} (CH_3 symmetric bending in Si-CH_3), 1251 cm^{-1} and 1010 cm^{-1} (Si-O-Si), and 787 cm^{-1} (CH_3 rocking in Si-CH_3). The typical absorption peaks of PAAm hydrogel were not observed: at wavenumber of 1625 cm^{-1} (C-O stretching), 1599 cm^{-1} (N-H bending), and 1452 cm^{-1} and 1325 cm^{-1} (the scissoring and twisting vibrations of CH_2). Also, the spectra did not manifest the IR absorption of water at wavenumber of 3500 cm^{-1} (O-H stretch) and 1635 cm^{-1} (O-H-O scissors bending).

5.2.3 Side-view Imaging

The side view of the static contact was imaged using FASTCAM Mini AX high-speed camera (Photron) coupled to the Resolv4K lens (Navitar). A 4x objective lens (Olympus) was additionally attached to attain the spatial resolution of 3 – 4 µm/pixel. Hydrogels were placed on the silicone gels using a PTFE-coated stainless steel dispensing needle. The captured side view images were subsequently processed using custom MATLAB routines and ImageJ. The contact line was located where the gray scale intensity presented the maximum slope. Within the detected boundary of the hydrogel profile, the maximum circle was fitted, and the corresponding radius, wetting foot, wetting ridge height, macroscopic contact angle, and contact radius were measured. For each pair of hydrogels and soft substrates, three to five static measurements were performed. Care was taken to perform imaging as soon as equilibrium configuration was reached to minimize dehydration of hydrogels. As control experiments, static measurements of water droplets and glass beads were also performed on bare glass slides and the soft substrates.

For static configuration where the side view shadowgraphy provides inadequate resolution or clarity (for *e.g.,* glass sphere contacts), we use bottom-view bright-field measurements at a magnification of 10x providing a resolution of 1 µm/pixel (Appendix Fig. D.5.9).

5.2.4 Measurement of Adhesion

For measuring the work of adhesion between hydrogel and PDMS, we used a cantilever-based force probe [237]. A polymeric capillary tube of diameter 410 µm and spring constant, $k = 305 \pm 6.1$ nN/µm is used as the cantilever probe. A hydrogel sphere/droplet is attached to the tip of the probe and the PDMS substrate (affixed to a linear actuator) is made to approach the probe at a prescribed velocity. Once, contact is established, there is a hold time after which the PDMS substrate is made to retract. The adhesion induced interaction between PDMS and the hydrogel probe causes deflection x of the cantilever. Consequently, the maximum deflection Δx is measured, and the corresponding peak adhesion force is calculated using, $F = k\Delta x$ (Appendix Fig. D.5.10). The work of adhesion is calculated using the relation for critical pull-off force: $F \approx 4\pi R_0 \gamma cos\theta^* + \pi\gamma(a^2 + b^2)/b + 4\pi a w$, where b is the vertical height of the hydrogel. Here, the first term reflects the capillary force from the hydrogel foot [216], the second term reflects the capillary force from the spherical cap profile [226], and the last term represents the hydrogel-PDMS adhesion force [217,218]. For example, for the experiment shown in Appendix Fig. D.5.10, we obtain the peak (pull-off) force $F = 1.6$ mN. Consequently, using $\gamma = 61.9$ mN/m, $a \approx 0.48$ mm, $b \approx 1.97$ mm, $R_0 \approx 1$ mm, and $\theta^* \approx 70°$, we calculate $w \approx 124.5$ mN/m.

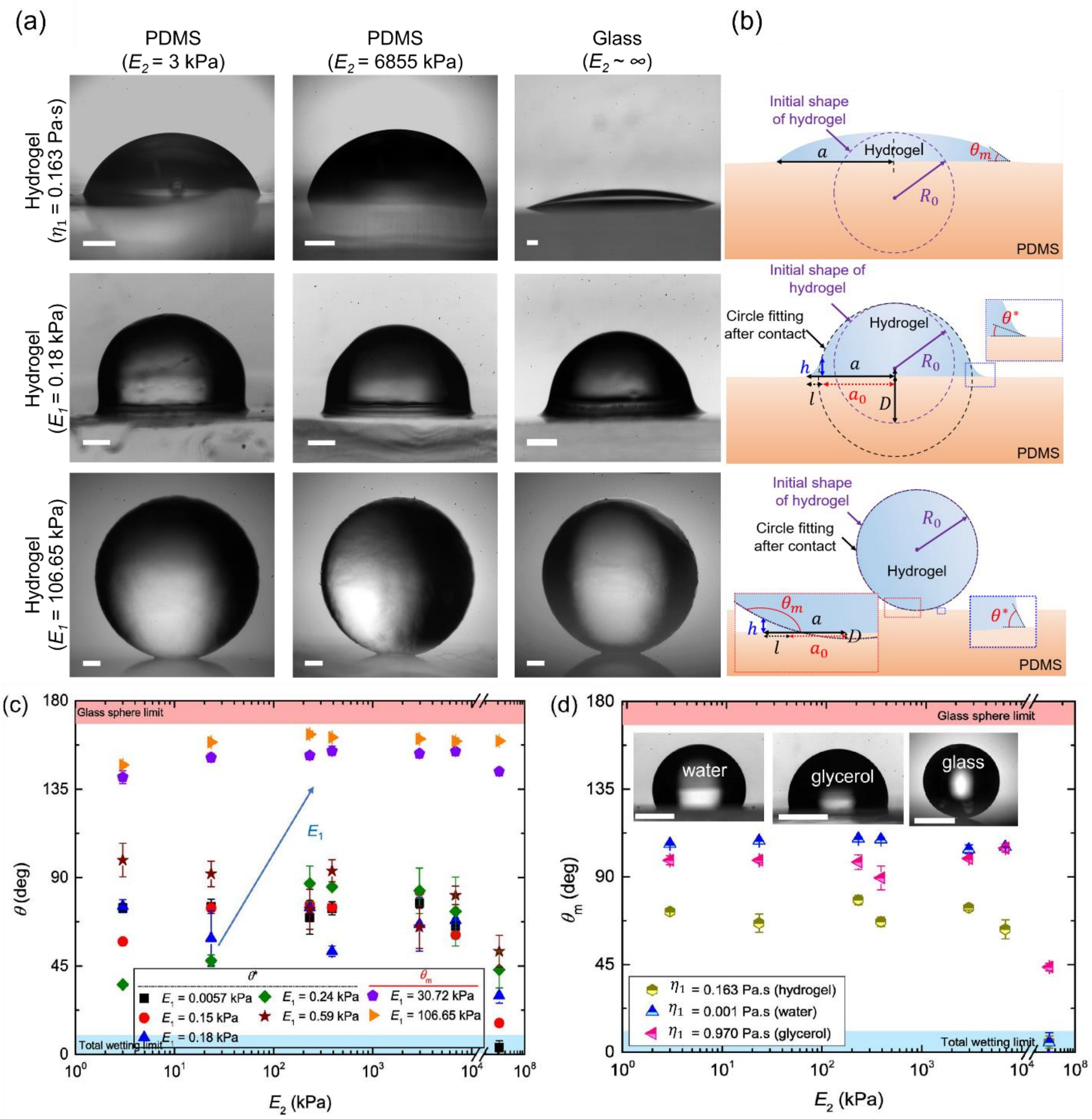

Figure 5.1 Structure of soft systems from wetting to adhesive contact. (a) Equilibrium snapshots of hydrogels of varying elasticity (E_1) on soft PDMS substrates (E_2 = 3 kPa and E_2 = 6855 kPa) and rigid glass substrates. The first row of images corresponds to the liquid-like hydrogels with μ = 0.163 Pa·s while the second and third row of images corresponds to hydrogels with Young's modulus E_1 = 0.18 kPa and E_1 = 106.65 kPa, respectively. **(b)** Schematic of the different contact/wetting configuration of hydrogels on

soft/rigid substrates. Here, R_0 and a are the initial hydrogel radius and contact radius, respectively. a_0 and δ are the fitted apparent contact radius and apparent indentation depth, respectively. h and l are the foot-height and foot-length, respectively. θ^* is the contact angle of the foot while θ_m is the macroscopic contact angle. **(C)** Variation of contact angles of hydrogels of varying elasticity (E_1) on pristine, soft PDMS substrates of varying elasticity (E_2). **(D)** Variation of macroscopic contact angles θ_m of *liquid hydrogel* and pure liquids (water, glycerol) on soft PDMS substrates. Scale bars represent 0.5 mm.

5.3 Results and Discussion

5.3.1 Morphology of the Contacting Pairs

We performed static measurements of 1 mm radius hydrogels ($R_0 = 0.96 \pm 0.04$ mm) on soft PDMS across a wide range of both hydrogel and PDMS elasticity using shadowgraphy. Briefly, we prepared hydrogel drops using acrylamide (AAm) as a monomer, N,N'-Methylene-bis-acrylamide (BIS) as the crosslinker, and 2,4,6-tri-methyl benzoyl-diphenylphosphine oxide (TPO) nanoparticle as the initiator. The elasticity of the hydrogels (*i.e.,* E_1) is varied between 0.0057 kPa to 106.65 kPa by diluting the monomer in weight percentages of 4.0 – 13.0. We further prepared a *liquid hydrogel* using 2.5 wt. % of the monomer which behaves almost like a liquid with viscosity, η_1 = 0.163 Pa·s. To prepare soft substrates, we used a combination of two different polydimethylsiloxane (PDMS): Sylgard 184 and Sylgard 527 in weight ratios of 10:1 and 1:1, respectively. Consequently, we mixed the two solutions in different weight ratios to obtain soft substrates with Young's modulus (*i.e.,* E_2) varying between 3 kPa to 6855 kPa. For each soft substrates, thus prepared, we performed static experiments on pristine surfaces as well as on ones treated with plasma to make it hydrophilic. We also performed experiments of water droplets and glass spheres on the soft PDMS and rigid glass substrates. Consequently, assuming ν_1, ν_2 ≈ 0.5 [55,222], we vary E^* between 0.007 kPa to 10^4 kPa.

In Figure 5.1(a), we show the static configuration of spherical hydrogels on pristine, soft PDMS substrates as well as on rigid glass slides. It is evident from Figure 5.1(a) that as the elasticity of the hydrogel droplet increases, its contact radius a decreases, similar to that observed in a recent study [55] (Appendix Figs. D.5.1-3). On one hand, the hydrogel with the lowest elasticity behaves like a liquid and exhibits significant spreading upon initial contact with the substrate. On the other hand, as the elasticity increases, the hydrogels exhibit decreasing spreading trend and converges to the contact behavior shown by rigid glass spheres. However, the contact behavior, *i.e.*, the contact radius is dominated mostly by hydrogel elasticity and shows certain changes with surface elasticity, which will be discussed later in text. Further, at equilibrium, the hydrogels form a distinct foot-like region close to the three-phase contact line: a phenomenon first predicted by Joanny *et al.* [238] and later experimentally verified [53]. The foot region exhibits a finite contact angle θ^* which is markedly different than that exhibited by pure water/glycerol droplets on the PDMS substrates (Figs. 5.1(b)-(d)). The appearance of the foot disappears for the liquid-like hydrogel mimicking wetting of pure liquids with a macroscopic apparent contact angle θ_m (Figs. 5.1(b) and (d)). The foot region also diminishes for the stiffer hydrogels and although they possess a finite θ^*, we use θ to analyze their contact behavior and show how the contact angle behavior for hydrogels converge to that exhibited by glass spheres (Fig. 5.1(c)). To analyze the features of this foot region, we first extract the apparent contact radius a_0 and apparent indentation depth δ by fitting the largest possible circle to the hydrogel profile (Fig. 5.1(b)). Consequently, we highlight the deformation zone, *i.e.*, the foot in terms of its height h and length l (Fig. 5.1(b)). It can be observed from Fig. 5.1(a) that with increasing hydrogel elasticity, the foot-height (and length) reduces as well (see Appendix Figs. D.5.1-3**)**.

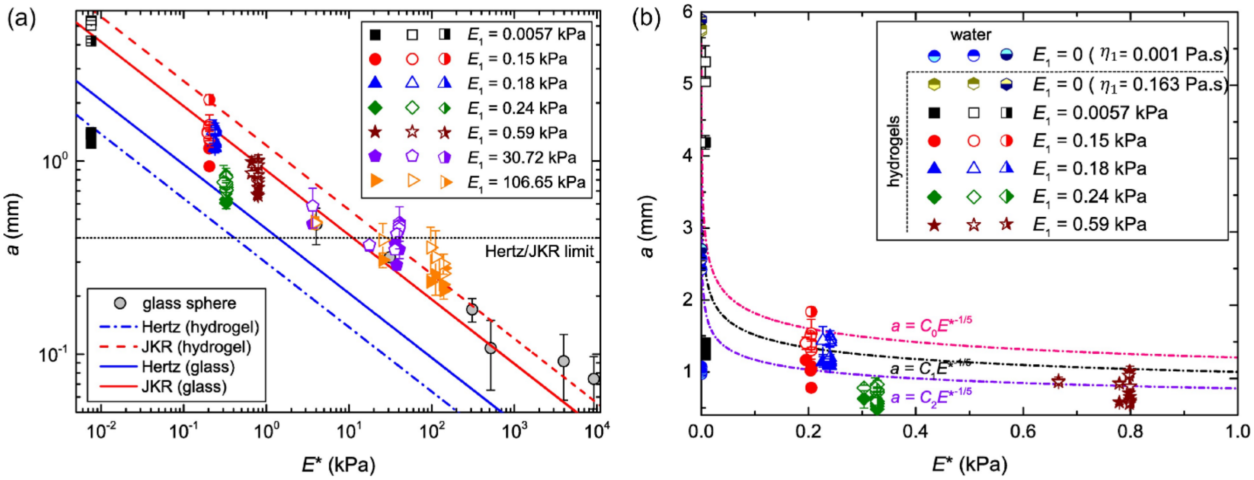

Figure 5.2 Contact radius *vs.* effective Young's modulus. (a) Variation of contact radius a with effective Young's modulus E^* for hydrogels-on-PDMS, hydrogels-on-glass slide, and glass sphere-on-PDMS system. E_1 represents the elastic modulus of the hydrogels whereas PDMS elasticity E_2 is embedded in E^*. The closed symbols, open symbols and half-closed symbols represent hydrogels on pristine PDMS, hydrogels on plasma-treated PDMS and hydrogels on glass slides, respectively. The data for spherical glass spheres on PDMS (grey circles) is also shown. The Hertz and JKR theory (see main text) for both hydrogels (dashed lines) and glass spheres (solid lines) are plotted. The plots representing the theory are extended artificially beyond the Hertz/JKR limit of small strain, or equivalently $a \geq 0.4$ (see main text). **(b)** Variation of contact radius a with effective Young's modulus E^* for hydrogels-on-PDMS as well as liquid hydrogel and water droplets on PDMS (corresponds to $E^* = 0$). The dashed lines show the fitting, $a \sim E^{*-1/5}$. The prefactors are $C_0 = 0.8$, $C_1 = 1.0$, and $C_2 = 1.2$. The symbol coding is same as **(a)**.

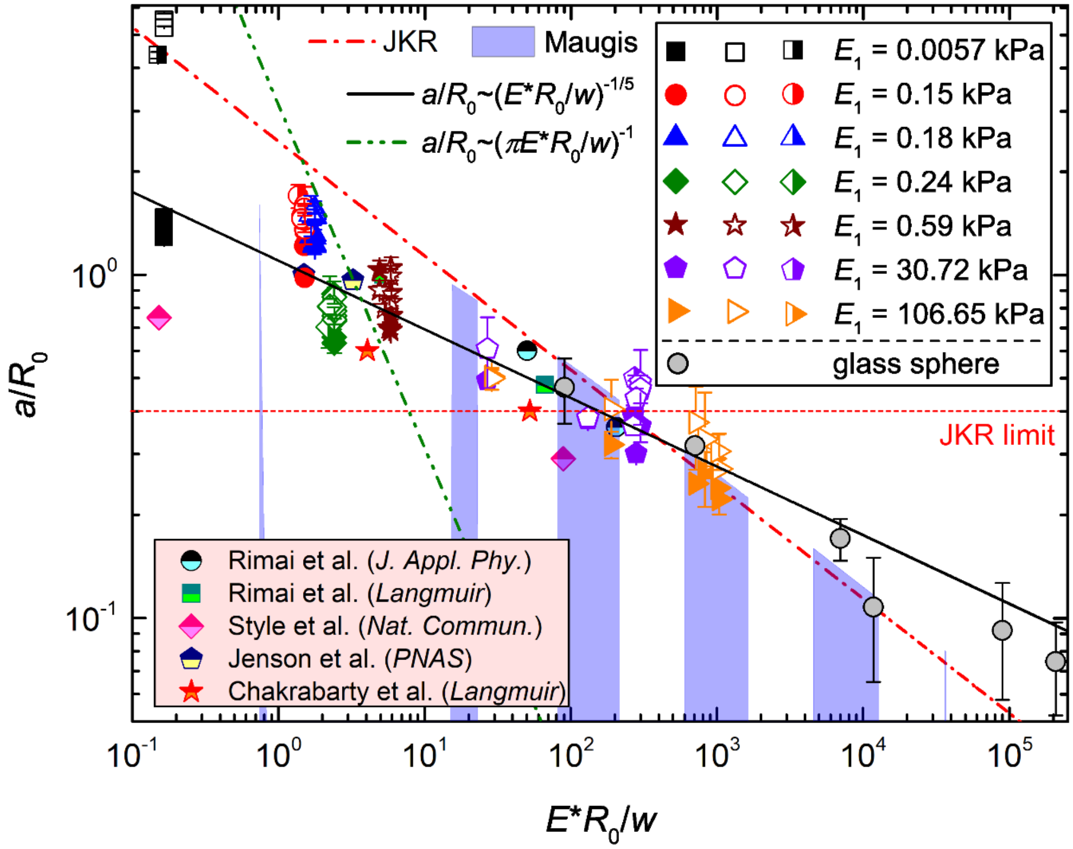

Figure 5.3 Normalized contact radius *vs.* elasto-adhesive parameter. Variation of normalized contact/wetting radius a/R_0 with elasto-adhesive parameter E^*R_0/w are shown for hydrogels of different elasticity (E_1) on soft PDMS substrates of different elasticity (E_2) as well as on rigid glass slides. The normalized contact radius data for rigid glass spheres on PDMS substrates are also shown. The contribution of E_2 is embedded in E^*. The closed symbols, open symbols, and half-closed symbols represent hydrogels on pristine PDMS, hydrogels on plasma-treated PDMS and hydrogels on glass slides, respectively. The dashed red and dashed green lines represent the JKR and approximated Maugis model, respectively (see main text). The solid black line represents the scaling law, $a/R_0 \sim (E^*R_0/w)^{-1/5}$. The blue shaded regions represent the standard Maugis model (Eq. 5.1). Literature data are shown in the same plot.

5.3.2 Variation of Contact Radius with Effective Elastic Modulus

In Fig. 5.2(a), we analyze the variation of the hydrogel-PDMS as well as hydrogel-glass contact radius a for different hydrogels with the effective Young's modulus of the contacting pair E^*. It should be noted here that the contribution of surface (PDMS/glass) elasticity, *i.e.*, E_2 is embedded in E^*. We observe that with increasing E^*, the contact radius decreases and eventually converges to magnitude for rigid glass spheres atop the soft substrates. Interestingly, we observe that the hydrogel contact radius increases only marginally on plasma treated soft substrates (see Fig. 5.2(a), open symbols), exhibiting the same overall trend with E^* as before. The effect of underlying substrate only becomes prominent for the softest hydrogel (E_1 = 0.0057 kPa), where the contact radius is significantly larger for glass slides and plasma treated PDMS substrates as compared to pristine PDMS substrates. This observation reflects that below a certain elasticity, the hydrogels start to exhibit liquid-like wetting behavior: higher degree of wetting for hydrophilic (glass, plasma treated PDMS) surfaces than hydrophobic (pristine PDMS) ones. It should be noted here that for relatively softer hydrogels, $a \approx R_0$ while for relatively stiffer ones, $a < R_0$. Consequently, the effective strain of the system, *i.e.*, a/R_0 varies from 0.05 to greater than 5. Nevertheless, we first compare our experimental data with Hertz and JKR theories. We observe that Hertz theory deviates significantly from our experimental data, whereas JKR theory finds agreement only for certain cases. Notably, for hydrogels and glass spheres, JKR theory provides a satisfactory match for $E^* > 20$ kPa. The above condition coincides with $a/R_0 < 0.4$, an important consideration for JKR (or Hertz) theory to hold. Here, for fitting JKR theory, we used $w \approx 130$ mN/m and $w \approx 44$ mN/m for hydrogel-PDMS and glass-PDMS [222] contacts, respectively. It should be noted here that the lack of agreement for Hertz theory is likely due to presence of adhesion and large deformations present in our system. Also, since the Tabor parameter [46] relevant to the problem, $\mu_T = (R_0 w^2/E^{*2} z_0)^{1/3} \gg 1$, no comparison with DMT theory [45] was performed. Here, z_0 is the characteristic length scale representing the range of surface forces and is in the order of nanometers [217,236]. The limiting case of water droplets and liquid-like hydrogel on the soft substrates are shown in Fig.

5.2(b) which corresponds to $E^* \approx 0$. Consequently, we attempt to fit our hydrogel contact radius data beyond the Hertz/JKR limit with that of wetting of pure liquids (water and liquid hydrogel). We observe that the scaling law, $a \sim {E^*}^{-1/5}$, is in close agreement with the observed data. As a holistic measure, we compared the fitted law with different prefactors: $C_1 = 0.8$, $C_2 = 1.0$, and $C_3 = 1.2$ (Fig. 5.2(b)). On dimensional analysis, the prefactor can be expressed as $w^{1/5}R_0^{4/5}$ which is approximately equal to 0.0026 $\mathrm{N}^{1/5}\mathrm{m}^{3/5}$, or equivalently 0.65 $\mathrm{N}^{1/5}\mathrm{mm}^{3/5}$ (adjusted for units in E^* converted to $\mathrm{N/mm}^2$), thus satisfying our fitted prefactor. The proposed scaling law predicts $a \rightarrow \infty$ as $E^* \rightarrow 0$. However, pure liquids exhibit finite wetting radius for partially-wetting and hydrophobic surfaces and only for complete wetting they form an extended thin film whose wetting radius can be considered approaching a very large value. Thus, the proposed scaling law is restricted only for *total wetting* scenario. To check the applicability of the scaling law to our entire range of experimental parameters as well to account for the different work of adhesion presented by the contacting pairs, *i.e.*, glass-PDMS, hydrogel-PDMS, and hydrogel-glass, we resort to non-dimensionalization for further analysis. Additionally, using non- dimensional analysis aids us in effectively comparing our findings with similar phenomena studied in existing literature [44,50,135].

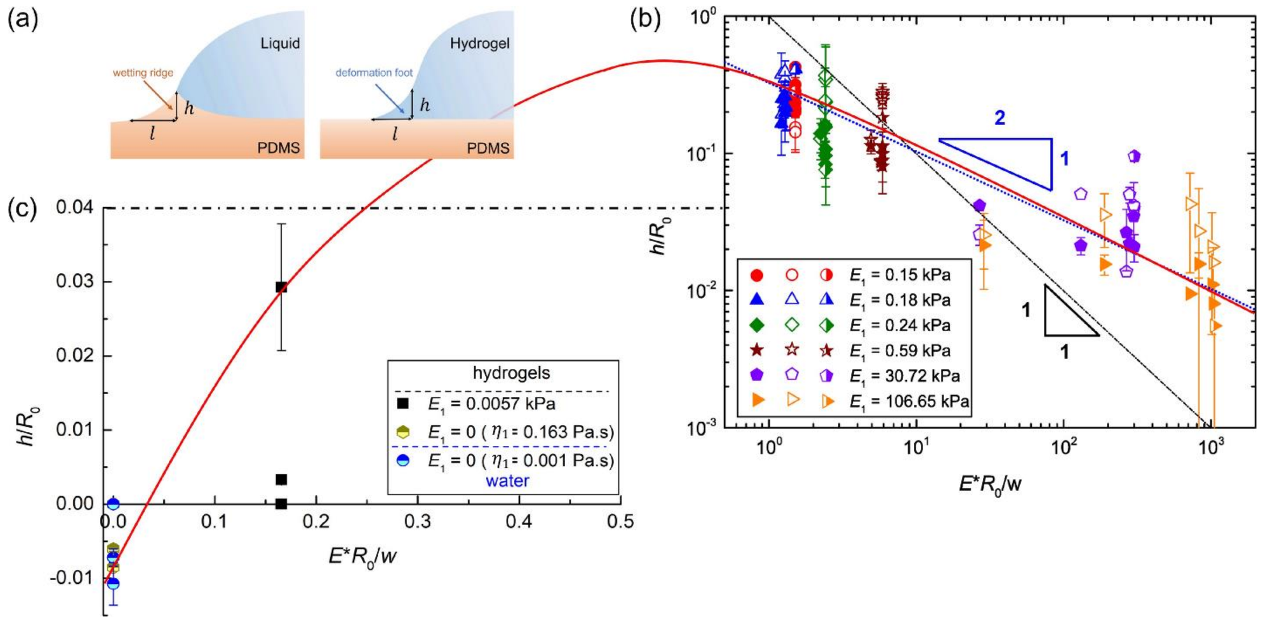

Figure 5.4 Variation of foot-like structure with elasto-adhesive parameter. (a) Schematics of liquid droplets on soft substrates forming a wetting ridge and hydrogels forming a distinct foot-like deformation region. **(b)** Variation of normalized foot-height h/R_0 with elasto-adhesive parameter E^*R_0/w for hydrogels of different elasticity (E_1) on soft PDMS substrates of different elasticity (E_2). The dashed black line represents the scaling law, $h/R_0 \sim (E^*R_0/w)^{-1}$ whereas the dashed blue line represents the scaling law, $h/R_0 \sim (E^*R_0/w)^{-1/2}$. The closed symbols, open symbols and half-closed symbols represent hydrogels on pristine PDMS, hydrogels on plasma-treated PDMS and hydrogels on glass slides, respectively. **(c)** Linear plot of variation of normalized foot-height h/R_0 with elasto-adhesive parameter E^*R_0/w for the hydrogel with the lowest elasticity, the liquid hydrogel and water droplets. Deformation in hydrogel (foot) is along the +ve h/R_0 axis, while those in PDMS (wetting ridge) is along the -ve h/R_0 axis. The red spline is artificially drawn to highlight the transition from **(b)** to **(c)**.

5.3.3 Transition between Wetting and Adhesion

Here, we analyze the variation of normalized contact radius a/R_0 with non-dimensionalized elasto-adhesive parameter E^*R_0/w. We compare our experimental data with the normalized form of JKR as well the Maugis theory. Maugis' theory [220,221,239] is applicable for large deformations and a wide parameter space. According to this approach, the contact radius can be expressed as [220],

$$F = \frac{3aE^*}{2}\left(\frac{R_0^2 + a^2}{4a}\ln\frac{R_0 + a}{R_0 - a} - \frac{R_0}{2} - \sqrt{\frac{8\pi a w}{3E^*}}\right) \tag{5.1}$$

where F is the applied load. On numerically solving Eq. (5.1) using our system properties and $F = 0$, we observe that *real number* solutions are obtained only intermittently. Further, since our experimental contact radius spans across a large range and assumes values close to the hydrogel radius, we approximated Eq. (5.1) for the case $a \rightarrow R_0$, yielding $a \sim (\pi w/E^*)$, or equivalently $a/R_0 \sim (\pi E^* R_0/w)^{-1}$. As shown in Fig. 5.3, normalized JKR theory satisfies our experimental data for $E^*R_0/w > 200$ whereas both forms of the Maugis' theory intermittently obey our experimental data. Consequently, we observe that most of our experimental data can be fitted using a scaling law, $a/R \sim (E^*R/w)^{-1/5}$. Here, the fitting parameter is of the order of unity. To highlight the applicability of our proposed scaling law, we plot existing literature data corresponding to rigid-on-soft as well as soft-on-rigid contact systems in the same plot and found them in close agreement. Although, our experimentally observed scaling law reasonably agrees with experimental data across six order of magnitude in E^*R_0/w, we argue that $E^*R/w \approx 200$ can be thought of as a reasonable transition point above which JKR theory is applicable and below which onset of wetting-like interactions occur.

We note that conventional contact theories rely on minimization of total energy (elastic, adhesion, capillary) of the contact system with respect to either contact radius a or indentation depth δ. For the large deformations present in the current work, the appropriate elastic energy is the solution of the Boussinesq problem [220,226], $U_{el} \sim E^* {R_0}^3 \int_0^{a/R_0} [1/2 - (1+x'^2)/4x' \ln((1+x')/(1-x'))]\, dx'$, where the integral representing the strain dx' diverges at $a/R_0 = 1$. However, the proposed scaling law, $a/R_0 \sim (E^* R_0/w)^{-1/5}$ smoothly translates from low deformation to deformations beyond $a/R_0 = 1$, diverging only at $E^* = 0$ (pure liquid case). At the same time, the above observation indicates that the present contact problem extends beyond Hookean elasticity and may include additional factors like non-linear elasticity [240] or plasticity [241]. Additionally, surface tension effects (hydrogel, PDMS) are expected to contribute for $E^* R_0/w \leq 10$. Eventually, the contribution from elasticity disappears in the liquid limit ($E^* = 0$), where adhesion induced contact is solely resisted by liquid (hydrogel) surface tension γ. Here, we can express the contact radius as $a/R_0 \sim f(\gamma/w)$. For the simplest case, $a/R_0 \approx \sqrt{w/2\gamma} \approx 1$ [230], which obeys our experimentally observed contact radius values for very soft/liquid hydrogels as well as water droplets on pristine PDMS substrates. In this liquid limit, elasticity effects only from the soft substrate will have contribution which is localized solely at the three-phase contact line for droplet sizes used in the present study [34,136,242]. This particular aspect is further discussed later on in the text. However, a more rigorous theoretical analysis taking into account of possible effects along the entire parameter space is beyond the scope of the present work.

5.3.4 Deformation of Foot and Wetting Ridge

Interestingly, the contact radius is not the sole variable aiding our understanding of this transition problem. As mentioned previously, the hydrogels undergo a deformation close to the contact and exhibit a foot-like region (Fig. 5.4A). The foot diminishes as the hydrogel elasticity increases (or decreases) and resembles the spherical cap configuration of water droplets for the *liquid hydrogel*. Here, we probe the evolution of the hydrogel foot-height to better understand the adhesion-wetting transition. Briefly, we recall that for rigid glass spheres ($E_1 \approx \infty$) and liquid droplets ($E_1 \approx 0$) on soft substrates, deformation entirely occurs on the soft substrates [34,40,44,128,136,216,222,242] (Fig. 5.4(a)). However, for a finite elasticity E_1, the deformation is completely in the hydrogel bulk. As shown in Fig. 5.4(b)-(c), the foot height increases with decreasing $E^*R_0/w \approx 0.2 – 0.5$ and eventually experiences an inflection point at $E^*R_0/w \approx 0.2 - 0.5$ (or equivalently, $E_1 \approx 0.005$ kPa − 0.1 kPa). Below that threshold value, the deformation occurs in the soft substrates at the contact line. The commonly called *wetting ridge* is observed for the liquid-like hydrogel (η_1 = 0.163 Pa·s) on the soft substrates. As convention, we represent deformation in the hydrogel as +ve and that in the soft substrate as -ve in Fig. 5.4(b)-(c). Further, we observe that the hydrogel with least elasticity, *i.e.,* $E_1 =$ 0.0057 kPa exhibits no *foot* for some of the softer PDMS substrates whereas the liquid hydrogel exhibits no *wetting ridge* for some of the stiffer PDMS substrates indicating a delicate dependence on E^* at the inflection point. Lastly, in stark contrast to deformation in soft substrates, which obey $h \sim \gamma/E_2$ [34,136,242], here we observe that the hydrogel foot height can be represented using a scaling law, $h/R_0 \sim (w/E^*R_0)^{1/2}$ (Fig. 5.4(b)): a dependence with $E^{-1/2}$ rather than E^{-1}.

5.4 Conclusions

Through careful experimentation of hydrogels, water droplets and rigid glass spheres on soft PDMS and rigid glass substrates, we have highlighted the transition from contacting surfaces to wetting of liquids. Our observations indicate that the transition can be represented as an extensive zone using the elasto-adhesive parameter E^*R_0/w which accounts for elasticity of both the contacting pairs as well the work of adhesion between the two. From the analysis of contact/wetting radius, we identify that the transition region has an upper bound, *i.e.,* $E^*R_0/w \approx 200$, beyond which JKR theory can adequately explain contacting surfaces. At the same time, we highlight that the crossover of the contact/wetting radius from adhesion to wetting can be expressed using the relation $a/R_0 \sim (E^*R_0/w)^{-1/5}$. Lastly, analysis of the foot-like deformation region of the hydrogel provides us with a crucial insight: as E^*R_0/w approaches zero, the deformation in the hydrogel tends to zero, and instead onset of deformation in the soft substrate, *i.e.*, the wetting ridge, occurs.

Chapter 6

Conclusions and Future Outlook

This chapter briefly summarizes the key findings and contributions of each research work with several suggestions for future studies.

6.1 Summary of Doctoral Research

Much of the richness of soft interfaces arises from conditions far from equilibrium. This is mainly because structures of soft solids are based on weak interaction forces, which can be affected by even environmental perturbations. Transient structural deformations of soft solids bring complexity to their contact systems but simultaneously create interesting, unexpected phenomena, which might be a key to resolving engineering problems in our daily lives. Nonetheless, our understanding of the inherently dynamic soft contact systems is still in infancy. Therefore, in this dissertation, systematical experimental studies were performed to explore various interface dynamic systems of soft solids from sliding to stationary contact. Chapter 2 discussed how soft viscoelastic tribopairs affect lateral sliding friction under different preloads and sliding speeds. In dry contact, the friction coefficient between viscoelastic tribopairs presented a higher dependence on the preload: $\mu_{dry} \propto F^{-0.45}$, indicating an adhesive zone outside the Hertzian contact zone. In addition, when the free liquids in soft substrates increased continuously, the dry friction coefficient increased and then decreased at the loss tangent of the underlying substrate ~ 0.1 (30 wt.% of free liquids). This sudden decrease in friction was not shown in lubricated contact, implying that the residual free liquids worked as a lubricant. The lubricating effect was more predominant than the viscoelastic dissipation over the loss tangent ~ 0.1. The relative roles of key parameters were presented through the regression analysis. The corresponding adjusted R^2 was provided to validate the reliability of the found correlations.

In Chapter 3, the role of residual free liquids was further investigated in stationary contact systems. Instead of applying shear force on the soft surfaces like in the previous chapter, we designed stationary contact systems to focus on the inherent soft solids' non-equilibrium state. While contact mechanics has been widely studied for soft solids, ideal conditions are often assumed: the semi-infinite thickness of underlying substrates and negligible gravity effect (*i.e.*, the characteristic length scale < the capillary length). However, practical examples do not always follow the ideal conditions. In this regard, we studied thin gel films in contact with a macro-scale glass sphere. In those conditions, long-term deformation of the gel surface was found over 85 hr. The surface deformation process presented two distinct stages wherein either the gravitational effect predominated (early stage) or the viscous flow of free liquids predominated (later stage).

Chapter 4 examined more dynamic interface phenomena by investigating the role of residual free liquids on the flowing fluids. In the early chapters, we found interesting roles of mobile liquids in the polymeric network at the interfaces with (rigid or soft) solids. In this chapter, the different experimental set-ups were designed wherein the free liquids in the networks contacted flowing pure liquids. While previous studies have been well studied varying hydraulic diameters of soft channels under the pressure gradient from flowing fluids, the role of soft viscoelastic walls was uncovered at the interface with flowing fluids. While limiting the deflection and compression of soft walls, the residual oligomers worked as a potential lubricant at the fluid/soft wall interface. This experimental observation was further expressed as a power-law model between the pressure drop and the loss tangent with the exponent of - 0.9. Another highlight of this work was that a modified friction factor for the viscoelastic wall channel could be approximated as $47/Re$.

In Chapter 5, a wide range of viscoelasticity of soft contact pairs was comprehensively investigated to provide a more general framework for understanding soft contact systems. The two extreme regimes were bridged, pure wetting, and adhesive contact limits. The singularity at the contact boundary created a foot-like regime. The effective elasticities of contact pairs predominantly affected the contact system over the work of adhesion. A general scaling analysis was provided between the normalized contact radius and the elasto-adhesive parameter: $a/R_0 \sim (E^*R_0/w)^{-1/5}$ that agreed well with experimental results.

Through this dissertation, soft viscoelastic solids demonstrated their wetting, adhesion, and lubrication in different contact systems, departing from classical wetting (for pure liquids) and adhesive contact physics (for elastic solids). In the following section, suggestions for future research are provided.

6.2 Suggestions for Future Work

The research reported in this thesis has comprehensively demonstrated distinctive features of soft contact systems and explained the physics behind the phenomena. However, some aspects of the soft contact systems have yet to be thoroughly examined. Exploring these subjects would deepen our understanding of soft solids, as well as help the development of advanced technologies.

One could consider examining rolling friction in a soft tribosystem. Viscoelastic properties of soft solids are quantified as the storage and loss moduli. Typically, the storage and loss moduli are measurable during frequency sweep within the linear viscoelastic region. This indicates that the measured moduli might have different values at different frequencies. Rolling friction naturally involves cyclic motions, thereby offering a specific frequency of the contact system. Hence, applying corresponding storage and loss moduli at each rolling speed might be an interesting direction for future work. In studying static signatures of soft systems, one might consider using polymeric materials with orientation-dependent properties (*e.g.*, cellulose nanocrystals (CNC)) to examine the role of anisotropic mechanical strength and surface energy on contact behaviors. One could also consider using poroelastic [152,154,243]or non-affine polymeric materials [244] to examine different governing factors at soft interfaces. Also, one could consider using imaging tools with a higher resolution, such as X-ray microscopy, to further uncover the detailed stress balance at the foot-like regions of two soft gels in contact. On the one hand, considering the prolonged interest, it could be interesting to design soft contact systems closely mimicking biological systems. Great analogies between soft tissues and soft solids make soft solids as promising qualitative models of soft tissues [13]. In biological systems, the balance between the tissue surface tension (*i.e.*, energy gain) and viscous internal friction (*i.e.*, energy loss) plays a crucial role in cell proliferation and apoptosis, which is close to the wetting and contact mechanics of soft solids.

154

References

1. Furukawa, K. S. *et al.* Novel Tissue-Engineered Artificial Vascular Graft Model composed from Cell, Gel, and Biodegradable Scaffold. *Annual International Conference of the IEEE Engineering in Medicine and Biology - Proceedings* **2**, 1207–1210 (2003).
2. Thurgood, P. *et al.* Porous PDMS Structures for the Storage and Release of Aqueous Solutions into Fluidic Environments. *Lab Chip* **7**, 2517–2527 (2017).
3. Regehr, K. J. *et al.* Biological Implications of Polydimethylsiloxane-Based Microfluidic Cell Culture. *Lab Chip* **9**, 2132–2139 (2009).
4. Tibbitt, M. W. *et al.* Hydrogels as Extracellular Matrix Mimics for 3D Cell Culture. *Biotechnol Bioeng* **103**, 655–663 (2009).
5. Stewart, B. 3D Bioprinting Hydrogel for Tissue Engineering an Ascending Aortic Scaffold. (2017).
6. Maccallum, N. *et al.* Liquid-Infused Silicone as a Biofouling-Free Medical Material. *ACS Biomater Sci Eng* **1**, 43–51 (2015).
7. Zeng, L. *et al.* Recent Advances of Organogels : from Fabrications and Functions to Applications Anti-fouling Anti-icing Droplet manipulation Organogels Drug delivery Food processing Cosmetic , Sensors , Capacitor ,. *Prog Org Coat* **159**, 106417 (2021).
8. Lavielle, N., *et al.* Lubrication Dynamics of Swollen Silicones to Limit Long Term Fouling and Microbial Biofilms. *Soft Matter* **17**, 936–946 (2021).
9. Madsen, E. L. *et al.* Instrument for Determining the Complex Shear Modulus of Soft-Tissue-like Materials from 10 to 300 Hz. *Phys Med Biol* **53**, 5313–5342 (2008).
10. Atlan, M. *et al.* A New Synthetic Model for Microvascular Anastomosis Training? A Randomized Comparative Study Between Silicone and Polyvinyl Alcohol Gelatin Tubes. *J Surg Educ* **75**, 182–187 (2018).
11. de Gennes, P. G. *et al. Soft Interfaces: The 1994 Dirac Memorial Lecture.* (Cambridge University Press, 2005)
12. Martinez, R. V. *et al.* Soft Actuators and Robots that are Resistant to Mechanical Damage. *Adv Funct Mater* **24**, 3003–3010 (2014).
13. Gong, Z. *et al.* Matching Material and Cellular Timescales Maximizes Cell Spreading on Viscoelastic Substrates. *Proc Natl Acad Sci U S A* **115**, E2686–E2695 (2018).
14. Li, Q. S. *et al.* AFM Indentation Study of Breast Cancer Cells. *Biochem Biophys Res Commun* **374**, 609–613 (2008).
15. van Vliet, K. J. *et al.* The Biomechanics Toolbox: Experimental Approaches for Living Cells and Biomolecules. *Acta Mater* **51**, 5881–5905 (2003).

16. Nerem, R. M. *et al.* Vascular Tissue Engineering. *Annu Rev Biomed Eng* **3**, 225–243 (2001).

17. Schwarz, U. S. *et al.* Physics of Adherent Cells. *Rev Mod Phys* **85**, 1327–1381 (2013).

18. Kovalenko, Y. *et al.* Bacterial Interactions with Immobilized Liquid Layers. *Adv Healthc Mater* **6**, 1–9 (2017).

19. Pan, F. *et al.* A Nanolayer Coating on Polydimethylsiloxane Surfaces Enables a Mechanistic Study of Bacterial Adhesion Influenced by Material Surface Physicochemistry. *Mater Horiz* (2019).

20. Karan, P. *et al.* Flow and Deformation Characteristics of a Flexible Microfluidic Channel with Axial Gradients in Wall Elasticity †. *Soft Matter* **16**, 5777 (2020).

21. Mirbod, P. *et al.* Laminar Flow Drag Reduction on Soft Porous Media. *Sci Rep* **7**, 1–10 (2017).

22. Fitzgerald, E. R. *et al.* Blubber and Compliant Coatings for Drag Reduction in Water I. Viscoelastic Properties of Blubber and Compliant Coating Materials. *Materials Science and Engineering C* **2**, 209–214 (1995).

23. Choi, K.-S. *et al.* Turbulent Drag Reduction using Compliant Surfaces. *Oceanographic Literature Review* **453**, 2229–2240 (1998).

24. Shuttleworth R. The Surface Tension of Solids. *Proceedings of the physical society. Section A* **63**, 444–457 (1950).

25. Chen, L. *et al.* Static and Dynamic Wetting of Soft Substrates. *Curr Opin Colloid Interface Sci* **36**, 46–57 (2018).

26. Lester, G. R. Contact Angles of Liquids at Deformable Solid Surfaces. *J Colloid Sci* **16**, 315–326 (1961).

27. Rusanov, A. I. theory of Wetting of Elastically Deformed Bodies. 1. Deformation with a Finite Contact-Angle. *Colloid Journal of the USSR* **37**, 614–622 (1975).

28. Shanahan, M. E. R. The Spreading Dynamics of a Liquid Drop on a Viscoelastic Solid. *J Phys D Appl Phys* **21**, 981–985 (1988).

29. Shanahan, M. E. R. The Influence of Solid Micro-Deformation on Contact Angle Equilibrium. *Journal of Physics D: Applied Physics J. Phys. D: Appl. Phys* **20**, 945–950 (1987).

30. Carre, A. *et al.* Viscoelastic Effects in the Spreading of Liquids. *Nature* **379**, 432–434 (1996).

31. Pericet-Cámara, R. *et al.* Effect of Capillary Pressure and Surface Tension on the Deformation of Elastic Surfaces by Sessile Liquid Microdrops: An Experimental Investigation. *Langmuir* **24**, 10565–10568 (2008).

32. Pericet-Cámara, R. *et al.* Solid-supported Thin Elastomer Films Deformed by Microdrops. *Soft Matter* **5**, 3611–3617 (2009).

33. Limat, L. Straight Contact Lines on a Soft, Incompressible Solid. *The European Physical Journal E* **35**, (2012).

34. Jerison, E. R., *et al.* Deformation of an Elastic Substrate by a Three-Phase Contact Line. *Phys Rev Lett* **106**, 1–4 (2011).

35. Style, R. W. *et al.* Static Wetting on Deformable Substrates, from Liquids to Soft Solids. *Soft Matter* **8**, 7177–7184 (2012).

36. Lopes, M. C. *et al.* Evaporation Control of Sessile Water Drops by Soft Viscoelastic Surfaces. *Soft Matter* **8**, 7875–7881 (2012).

37. Chen, L. *et al.* Short Time Wetting Dynamics on Soft Surfaces. *Soft Matter* **7**, 9084–9089 (2011).

38. Lopes, M. C. *et al.* Influence of Substrate Elasticity on Particle Deposition Patterns from Evaporating Water-Silica Suspension Droplets. *Soft Matter* **9**, 7942–7950 (2013).

39. Chen, L. *et al.* Inertial to Viscoelastic Transition in Early Drop Spreading on Soft Surfaces. *Langmuir* **29**, 1893–1898 (2013).

40. Park, S. J. *et al.* Visualization of Asymmetric Wetting Ridges on Soft Solids with X-ray microscopy. *Nat Commun* **5**, 1–7 (2014).

41. Cai, Z. *et al.* Fluid Separation and Network Deformation in Wetting of Soft and Swollen Surfaces. *Commun Mater* **2**, (2021).

42. Johnson, K. L. One Hundred Years of Hertz Contact. *Proceedings of the Institution of Mechanical Engineers* **196**, 363–378 (1982).

43. Johnson, K. L. *et al.* Surface Energy and the Contact of Elastic Solids. *Proceedings of the Royal Society A: Mathematical, Physical and Engineering Sciences* **324**, 301–313 (1971).

44. Style, R. W. *et al.* Surface Tension and Contact with Soft Elastic Solids. *Nat Commun* **4**, 1–6 (2013).

45. Derjaguin, B. V. *et al.* Effect of Contact Deformations on the Adhesion of Particles. *J Colloid Interface Sci* **53**, 314–326 (1975).

46. Tabor, D. Surface Forces and Surface Interactions. *J Colloid Interface Sci* **58**, 2–13 (1977).

47. Maugis, D. Adhesion of Spheres: The JKR-DMT Transition Using a Dugdale Model. *J Colloid Interface Sci* **150**, 243–269 (1992).

48. Carpick, R. W. *et al.* A General Equation for Fitting Contact Area and Friction vs Load Measurements. *J Colloid Interface Sci* **211**, 395–400 (1999).

49. Schwarz, U. D. A Generalized Analytical Model for the Elastic Deformation of an Adhesive Contact between a Sphere and a Flat Surface. *J Colloid Interface Sci* **261**, 99–106 (2003).

50. Rimai, D. S., *et al.* Adhesion-Induced Deformations of Polymeric Substrates: Particle Size Dependence of the Contact Area. *J Appl Phys* **66**, 3574–3578 (1989).

51. Demejo, L. P., *et al.* Direct Observations of Deformations Resulting from Particle-Substrate Adhesion. *J Adhes Sci Technol* **2**, 331–337 (1988).

52. Fogden, A. *et al.* Contact Elasticity in the Presence of Capillary Condensation. I. The Nonadhesive Hertz Problem. *J Colloid Interface Sci* **138**, 414–430 (1990).

53. Jensen, K. E. *et al.* Wetting and Phase Separation in Soft Adhesion. *Proc Natl Acad Sci U S A* **112**, 26–30 (2015).

54. Pham, J. T. *et al.* From Elasticity to Capillarity in Soft Materials Indentation. *Phys Rev Mater* **1**, (2017).

55. Chakrabarti, A. *et al.* Elastowetting of Soft Hydrogel Spheres. *Langmuir* **34**, 3894–3900 (2018).

56. Liang, H. *et al.* Surface Stresses and a Force Balance at a Contact Line. *Langmuir* **34**, 7497–7502 (2018).

57. Liang, H. *et al.* Surface Stress and Surface Tension in Polymeric Networks. *ACS Macro Lett* **7**, 116–121 (2018).

58. Glover, J. D. *et al.* Capillary-driven Indentation of a Microparticle into a Soft, Oil-Coated Substrate. *Soft Matter* **16**, 5812–5818 (2020).

59. Daalkhaijav, U. Rheological Techniques in Characterization and Aiding in the Modification of Soft Matter. (Oregon State University, 2018).

60. Yu, Y. *et al.* Multifunctional “Hydrogel Skins” on Diverse Polymers with Arbitrary Shapes. *Advanced Materials* **31**, (2019).

61. Scaraggi, M., *et al.* Experimental Evidence of Micro-EHL Lubrication in Rough Soft Contacts. *Tribol Lett* **43**, 169–174 (2011).

62. Read, M. L. *et al.* Dynamic Contact Angle Analysis of Silicone Hydrogel Contact Lenses. *J Biomater Appl* **26**, 85–99 (2011).

63. Tighe, B. J. A Decade of Silicone Hydrogel Development: Surface Properties, Mechanical Properties, and ocular Compatibility. *Eye Contact Lens* **39**, 4–12 (2013).

64. Shewan, H. M. *et al.* Tribology and its Growing Use toward the Study of Food Oral Processing and Sensory Perception. *J Texture Stud* 1–16 (2019) doi:10.1111/jtxs.12452.

65. Myant, C. *et al.* Influence of Load and Elastic Properties on the Rolling and Sliding Friction of Lubricated Compliant Contacts. *Tribol Int* **43**, 55–63 (2010).

66. Masjedi, M. *et al.* Mixed Lubrication of Soft Contacts: An Engineering Look. *Proceedings of the Institution of Mechanical Engineers, Part J: Journal of Engineering Tribology* **231**, 263–273 (2016).

67. Lee, D. W. *et al.* Stick-slip Friction and Wear of Articular Joints. *Proc Natl Acad Sci U S A* **110**, (2013).

68. Greene, G. W. *et al.* Adaptive Mechanically Controlled Lubrication Mechanism Found in Articular Joints. *Proceedings of the National Academy of Sciences* **108**, 5255 LP – 5259 (2011).

69. Guo, J. *et al.* Highly Stretchable, Strain Sensing Hydrogel Optical Fibers. *Advanced Materials* **28**, 10244–10249 (2016).

70. Miriyev, A. *et al.* Soft Material for Soft Actuators. *Nat Commun* **8**, 1–8 (2017).

71. Marco, C. De *et al.* Indirect 3D and 4D Printing of Soft Robotic Microstructures. *Adv Mater Technol* **1900332**, 1–7 (2019).

72. Greenwood, J. A. *et al.* The Friction of Hard Sliders on Lubricated Rubber: The Importance of Deformation Losses. *Proceedings of the Physical Society* **71**, 989–1001 (1958).

73. Hutt, W. *et al.* Soft Matter Dynamics: Accelerated Fluid Squeeze-out during Slip. *Journal of Chemical Physics* **144**, 1–11 (2016).

74. Selway, N. *et al.* Influence of Fluid Viscosity and Wetting on Multiscale Viscoelastic Lubrication in Soft Tribological Contacts. *Soft Matter* **13**, 1702–1715 (2017).

75. Persson, B. N. J. Silicone Rubber Adhesion and Sliding Friction. *Tribol Lett* **62**, 0–4 (2016).

76. Lorenz, B. *et al.* Static or Breakloose Friction for Lubricated Contacts: The Role of Surface Roughness and Dewetting. *Journal of Physics Condensed Matter* **25**, (2013).

77. Greenwood, J. A. *et al.* Hysteresis Losses in Rolling and Sliding Friction. *Proceedings of the royal society A* **259**, 480–507 (1961).

78. Pandey, A. *et al.* Lubrication of Soft Viscoelastic Solids. *J Fluid Mech* **799**, (2016).

79. Jacobson, B. The Stribeck Memorial Lecture. *Tribol Int* **36**, 781–789 (2003).

80. Moore, D. F. *The Friction and Lubrication of Elastomers.* (Cambridge University Press, 1972).

81. Bongaerts, J. H. H. Ã. *et al.* Soft-tribology: Lubrication in a Compliant PDMS – PDMS contact. *Tribol Int* **40**, 1531–1542 (2007).

82. Morina, A. *et al.* Surface and Tribological Characteristics of Tribofilms Formed in the Boundary Lubrication Regime with Application to Internal Combustion Engines. *Tribol Lett* **15**, 443–452 (2003).

83. de Vicente, J. *et al.* Rolling and Sliding Friction in Compliant, Lubricated Contact. *Proceedings of the Institution of Mechanical Engineers, Part J: Journal of Engineering Tribology* **220**, 55–63 (2006).

84. Myant, C. *et al.* An Investigation of Lubricant Film Thickness in Sliding Compliant Contacts. *Tribology Transactions* **53**, 684–694 (2010).

85. Yamaguchi, T. *et al.* Effects of Loading Angles on Stick–Slip Dynamics of Soft Sliders. *Extreme Mech Lett* **9**, 331–335 (2016).

86. Saintyves, B. *et al.* Self-sustained Lift and Low Friction via Soft Lubrication. *Proc Natl Acad Sci U S A* **113**, 5847–5849 (2016).

87. Hamrock, B. J. *et al.* Isothermal Elastohydrodynamic Lubrication of Point Contacts: Part III-Fully Flooded Result. *J Tribol* **99**, 264–275 (1977).

88. Esfahanian, M. *et al.* Fluid-film Lubrication Regimes Revisited. *Tribology Transactions* **34**, 628–632 (1991).

89. Kim, J. M. *et al.* Effect of Varying Mixing Ratio of PDMS on the Consistency of the Soft-Contact Stribeck Curve for Glycerol Solutions. *Tribol Int* **89**, 46–53 (2015).

90. Style, R. W. *et al.* Universal Deformation of Soft Substrates near a Contact Line and the Direct Measurement of Solid Surface Stresses. *Phys Rev Lett* **110**, 1–5 (2013).

91. Xu, Q. *et al.* Direct Measurement of Strain-dependent Solid Surface Stress. *Nat Commun* **8**, 1–6 (2017).

92. Johnston, I. D. *et al.* Mechanical Characterization of Bulk Sylgard 184 for Microfluidics and Microengineering. *Journal of Micromechanics and Microengineering* **24**, 1–7 (2014).

93. Placet, V. *et al.* Mechanical Properties of Bulk Polydimethylsiloxane for Microfluidics over a Large Range of Frequencies and Aging Times. *Journal of Micromechanics and Microengineering* **25**, (2015).

94. Wang, Z. Polydimethylsiloxane Mechanical Properties Measured by Macroscopic Compression and Nanoindentation Techniques. (University of South Florida, 2011).

95. Xu, B. *et al.* Microfluidic Channels Formed by Collapse of Soft Stamp. *J Nanomech Micromech* **1**, 3–10 (2011).

96. Fujii, T. PDMS-based Microfluidic Devices for Biomedical Applications. *Microelectron Eng* **61–62**, 907–914 (2002).

97. Volpatti, L. R. *et al.* Commercialization of Microfluidic Devices. *Trends Biotechnol* **32**, 347–350 (2014).

98. Zhang, W. *et al.* Surface and Tribological Behaviors of the Bioinspired Polydopamine Thin Films under Dry and Wet Conditions. *Biomacromolecules* **14**, 394–405 (2013).

99. Gidde, R. R. *et al.* On effect of Viscoelastic Characteristics of Polymers on Performance of Micropump. *Advances in Mechanical Engineering* **9**, 1–12 (2017).

100. Menczel, J. D. *et al.* *Thermal Analysis of Polymers*. (Wiley Online Library, 2009).

10. Studer, V. *et al.* Scaling Properties of a Low-Actuation Pressure Microfluidic valve. *J Appl Phys* **95**, 393–398 (2004).

102. Kim, S. *et al.* Revisit to Three-Dimensional Percolation Theory: Accurate Analysis for Highly Stretchable Conductive Composite Materials. *Sci Rep* **6**, 1–10 (2016).

103. Xue, L. *et al.* Stick-Slip Friction of PDMS Surfaces for Bioinspired Adhesives. *Langmuir* **32**, 2428–2435 (2016).

104. Feeny, B. *et al.* A Historical Review on Dry Friction and Stick-Slip Phenomena. *Appl Mech Rev* **51**, 321–341 (1998).

105. Berman, A. D. *et al.* Origin and Characterization of Different Stick-slip Friction Mechanisms. *Langmuir* **12**, 4559–4562 (1996).

106. Zhang, Q. *et al.* Interfacial Friction and Adhesion of Cross-linked Polymer Thin Films Swollen with Linear Chains. *Langmuir* **23**, 7562–7570 (2007).

107. Liu, Q. *et al.* Osmocapillary Phase Separation. *Extreme Mech Lett* **7**, 27–33 (2016).

108. Andreotti, B. *et al.* Statics and Dynamics of Soft Wetting. *Annu Rev Fluid Mech* **52**, 285–308 (2020).

109. Zhao, S. *et al.* Electronic Skin with Multifunction Sensors Based on Thermosensation. *Advanced Materials* **29**, (2017).

110. Yoshizawa, H. *et al.* Fundamental Mechanisms of Interfacial Friction. 1. Relation between Adhesion and Friction. *Journal of Physical Chemistry* **97**, 4128–4140 (1993).

111. Israelachvili, J. N. *Intermolecular and Surface Forces*. (Elsevier, 2011).

112. de Vicente, J. *et al.* The frictional properties of Newtonian fluids in rolling - Sliding soft-EHL contact. *Tribol Lett* **20**, 273–286 (2005).

113. Yan, Y. *Metals for Biomedical Devices.* Chapter 7, 178–201, Woodhead Publishing (2010).

114. Moore, D. F. *Viscoelastic Machine Elements: Elastomers and Lubricants in Machine Systems*. (Elsevier, 2015).

115. Khatibi, M. *et al.* Dynamical Feature of Particle Dunes in Newtonian and Shear-Thinning Flows: Relevance to Hole-Cleaning in Pipe and Annulus. *International Journal of Multiphase Flow* **99**, 284–293 (2018).

116. Makishima, A. *et al.* Calculation of Bulk Modulus, Shear Modulus and Poisson's Ratio of Glass. *J Non Cryst Solids* **17**, 147–157 (1975).

117. Gonzalez-Rodriguez, D. *et al.* Soft Matter Models of Developing Tissues and Tumors. *Science* **338**, 910–917 (2012).

118. Suresh, S. Biomechanics and Biophysics of Cancer Cells. *Acta Mater* **55**, 3989–4014 (2007).

119. Yang, H. *et al.* Fabricating Hydrogels to Mimic Biological Tissues of Complex Shapes and High Fatigue Resistance. *Matter* **4**, 1935–1946 (2021).

120. Patil, S. *et al.* Reusable Antifouling Viscoelastic Adhesive with an Elastic Skin. *Langmuir* **28**, 42–46 (2012).

121. Leong, Y. C. *et al.* The Viscoelastic Properties of Natural Rubber Pressure-Sensitive Adhesive using Acrylic Resin as a Tackifier. *J Appl Polym Sci* **88**, 2118–2123 (2003).

122. Kim, S. *et al.* Soft Robotics: A bioinspired Evolution in Robotics. *Trends Biotechnol* **31**, 287–294 (2013).

123. Zhang, Y. *et al.* Inchworm Inspired Multimodal Soft Robots with Crawling, Climbing, and Transitioning Locomotion. *IEEE Transactions on Robotics* 1–14 (2021).

124. Morales, D. *et al.* Electro-actuated Hydrogel Walkers with Dual Responsive Legs †. *Soft Matter* **10**, 1337–1348 (2014).

125. Wong, T. S. *et al.* Bioinspired Self-Repairing Slippery Surfaces with Pressure-Stable Omniphobicity. *Nature* **477**, 443–447 (2011).

126. Urata, C. *et al.* Self-lubricating Organogels (SLUGs) with Exceptional Syneresis-Induced Anti-Sticking Properties against Viscous Emulsions and Ices. *J Mater Chem A Mater* **3**, 12626–12630 (2015).

127. Lai, Y. *et al.* Indentation Adhesion of Hydrogels over a Wide Range of Length and Time Scales. *Extreme Mech Lett* **31**, 100540 (2019).

128. Style, R. W. *et al.* Elastocapillarity: Surface Tension and the Mechanics of Soft Solids. *Annu Rev Condens Matter Phys* **8**, 99–118 (2017).

129. Style, R. W. *et al.* The Mechanical Equilibrium of Soft Solids with Surface Elasticity. *Soft Matter* **14**, 4569–4576 (2018).

130. Andreotti, B. *et al.* Soft Wetting and the Shuttleworth Effect, at the Crossroads between Thermodynamics and Mechanics. *Epl* **113**, 66001 (2016).

131. Hourlier-Fargette, A. *et al.* Extraction of Silicone Uncrosslinked Chains at Air-Water-Polydimethylsiloxane Triple Lines. *Langmuir* **34**, 12244–12250 (2018).

132. Desai, P. R. *et al.* Supersolvophobic Soft Wetting: Nanoscale Elastocapillarity, Adhesion, and Retention of a Drop Behaving as a Nanoparticle. *Matter* **1**, 1262–1273 (2019).

133. Weijs, J. H. *et al.* Elasto-capillarity at the Nanoscale: On the Coupling between Elasticity and Surface Energy in soft solids. *Soft Matter* **9**, 8494–8503 (2013).

134. Rimai, D. S. *et al.* The Adhesion of Dry Particles in the Nanometer to Micrometer-size Range. *Colloids Surf A Physicochem Eng Asp* **165**, 3–10 (2000).

135. Rimai, D. S. *et al.* Adhesion Induced Deformations of a Highly Compliant Elastomeric Substrate in Contact with Rigid Particles. *Langmuir* **10**, 4361–4366 (1994).

136. Marchand, A. *et al.* Contact angles on a soft solid: From young's law to neumann's law. *Phys Rev Lett* **109**, 1–5 (2012).

137. Kenry *et al.* Viscoelastic Effects of Silicone Gels at the Micro- and Nanoscale. *Procedia IUTAM* **12**, 20–30 (2015).

138. Shull, K. R. Contact Mechanics and the Adhesion of Soft Solids. *Materials Science and Engineering: R: Reports* **36**, 1–45 (2002).

139. Crosby, A. J. *et al.* Adhesive Failure Analysis of Pressure-Sensitive Adhesives. *J Polym Sci B Polym Phys* **37**, 3455–3472 (1999).

140. Kim, S. *et al.* Whole body adhesion: Hierarchical, Directional and Distributed Control of Adhesive Forces for a Climbing Robot. *Proc IEEE Int Conf Robot Autom* 1268–1273 (2007).

141. Limozin, L. *et al.* Quantitative Reflection Interference Contrast Microscopy (RICM) in Soft Matter and Cell Adhesion. *ChemPhysChem* **10**, 2752–2768 (2009).

142. Huerre, A. *et al.* Absolute 3D Reconstruction of Thin Films Topography in Microfluidic Channels by Interference Reflection Microscopy. *Lab Chip* **16**, 911–916 (2016).

143. Misra, S. *et al.* Reflected Laser Interferometry: A Versatile Tool to Probe Condensation of Low-Surface-Tension Droplets. *Langmuir* **37**, 8073–8082 (2021).

144. Kim, A. R. *et al.* Viscoelastic Tribopairs in Dry and Lubricated Sliding Friction. *Soft Matter* **16**, 7447–7457 (2020).

145. Duineveld, P. C. *et al.* Diffusion of Solvent in PDMS Elastomer for Micromolding in Capillaries. *Langmuir* **18**, 9554–9559 (2002).

146. Robert W. S. *et al.* Traction Force Microscopy in Physics and Biology. *Soft Matter* **10**, 4047–4055 (2014).

147. Nandi, S. *et al.* Swelling Behavior of Partially Cross-linked Polymers: A Ternary System. *Macromolecules* **38**, 4447–4455 (2005).

148. Berman, J. D. *et al.* Singular Dynamics in the Failure of Soft Adhesive Contacts. *Soft Matter* **15**, 1327–1334 (2019).

149. Hertz, H. Über die Berührung Fester Elastischer Körper. *Journal für die reine und Angew. Math.* **92**, 156–171 (1882).

150. Müller, A., *et al.* A Quick and Accurate Method to Determine the Poisson's Ratio and the Coefficient of Thermal Expansion of PDMS. *Soft Matter* **15**, 779–784 (2019).

151. Cai, L. H. *et al.* Soft Poly(dimethylsiloxane) Elastomers from Architecture-Driven Entanglement Free Design. *Advanced Materials* **27**, 5132–5140 (2015).

152. Hu, Y. *et al.* Using Indentation to Characterize the Poroelasticity of Gels. *Appl Phys Lett* **96**, 121904 (2010).

153. Johnson, K. L. *Contact Mechanics*. (Cambridge University Press, 1985).

154. Xu, Q. *et al.* Viscoelastic and Poroelastic Relaxations of Soft Solid Surfaces. *Phys Rev Lett* **125**, 238002 (2020).

155. Karpitschka, S. *et al.* Droplets Move over Viscoelastic Substrates by Surfing a Ridge. *Nat Commun* **6**, 1–7 (2015).

156. Zhao, M. *et al.* Growth and Relaxation of a Ridge on a Soft Poroelastic Substrate. *Soft Matter* **14**, 61–72 (2017).

157. Du, C. *et al.* Linear Viscoelasticity of Weakly Cross-linked Hydrogels. *J Rheol* **63**, 109–124 (2019).

158. Takigawa, T. *et al.* Poisson's Ratio of Polyacrylamide (PAAm) Gels. *Polymer Gels and Networks* **4**, 1–5 (1996).

159. Oyen, M. L. Mechanical Characterization of Hydrogel Materials. *International Materials Reviews* **59**, 44–59 (2014).

160. Yang, J. *et al.* Hydrogel Adhesion: A Supramolecular Synergy of Chemistry, Topology, and Mechanics. *Adv Funct Mater* **30**, 1–27 (2020).

161. Shahsavan, H. *et al.* Bioinspired Functionally Graded Adhesive Materials: Synergetic Interplay of Top Viscous-Elastic Layers with Base Micropillars. *Macromolecules* **47**, 353–364 (2014).

162. Shahsavan, H. *et al.* Biologically Inspired Enhancement of Pressure-Sensitive Adhesives using a Thin Film-Terminated Fibrillar Interface. *Soft Matter* **8**, 8281–8284 (2012).

163. Martinez, R. V. *et al.* Robotic Tentacles with Three-Dimensional Mobility based on Flexible Elastomers. *Advanced Materials* **25**, 205–212 (2013).

164. Deneke, N. *et al.* Pressure Tunable Adhesion of Rough Elastomers. *Soft Matter* **17**, 863–869 (2021).

165. Çakmak, U. D., *et al.* Adherence Kinetics of a PDMS Gripper with Inherent Surface Tackiness. *Polymers (Basel)* **12**, 2440 (2020).

166. Matrose, N. A. *et al.* Fatigue-Induced Stress-softening in Cross-linked Multi-network Elastomers: Effect of Damage Accumulation. *Int J Plast* **142**, 102993 (2021).

167. Theodoly, O. *et al.* New Modeling of Reflection Interference Contrast Microscopy Including Polarization and Numerical Aperture Effects: Application to Nanometric Distance Measurements and Object Profile Reconstruction. *Langmuir* **26**, 1940–1948 (2010).

168. Daniel, D. *et al.* Oleoplaning Droplets on Lubricated Surfaces. *Nat Phys* **13**, 1020–1025 (2017).

169. Wilson, T. *et al. Theory and Practice of Scanning Optical Microscopy*. vol. 180 (Acamedic Press London, 1984).

170. Stenzel, Habil. O. *The physics of thin film optical spectra*. (Springer-Verlag, 2005).

171. Ghosh, G. Sellmeier Coefficients and Dispersion of Thermo-optic Coefficients for Some Optical Glasses. *Appl. Opt.* **36**, 1540–1546 (1997).

172. Cholewinski, A. *et al.* Underwater Contact Behavior of Alginate and Catechol-Conjugated Alginate Hydrogel Beads. *Langmuir* **33**, 8353–8361 (2017).

173. Berry, J. D. *et al.* Measurement of Surface and Interfacial Tension using Pendant Drop Tensiometry. *J Colloid Interface Sci* **454**, 226–237 (2015).

174. Mader-Arndt, K. *et al.* Single Particle Contact versus Particle Packing Behavior: Model Based Analysis of Chemically Modified Glass Particles. *Granul Matter* **16**, 359–375 (2014).

175. Weng, S. C. *et al.* Effect of Surface Condition on Liquid Crystal Photoalignment by Light-Induced Azo Dye Adsorption Phenomena. *Liq Cryst* **43**, 1221–1229 (2016).

176. Jensen, K. E. *et al.* Strain-dependent Solid Surface Stress and The Stiffness of Soft Contacts. *Phys Rev X* **7**, 041031 (2017).

177. Shull, K. R. *et al.* Axisymmetric Adhesion Tests of Soft Materials. *Macromol Chem Phys* **199**, 489–511 (1998).

178. Shrivastava, A. *et al.* Mass Transfer Enhancement due to a Soft Elastic Boundary. *Chem Eng Sci* **63**, 4302–4305 (2008).

179. Raj, M. K. *et al.* Hydrodynamics in Deformable Microchannels. *Microfluid Nanofluidics* **21**, 1–12 (2017).

180. Hardy, B. S. *et al.* The Deformation of Flexible PDMS Microchannels under a Pressure Driven Flow. *Lab Chip* **9**, 935–938 (2009).

181. Zhang, W. *et al.* Viscoelasticity Reduces the Dynamic Stresses and Strains in the Vessel Wall: Implications for Vessel Fatigue. *Am J Physiol Heart Circ Physiol* **293**, 2355–2360 (2007).

182. Yang, C. *et al.* A Model for Steady Laminar Flow Through a Deformable Gel-Coated Channel. *J Colloid Interface Sci* **226**, 105–111 (2000).

183. Lahav, J. *et al.* Gel-walled Cylindrical Channels as Models for the Microcirculation: Dynamics of Flow. *Biorheology* **10**, 595–604 (1973).

184. Raj, K. M. *et al.* Flow-Induced Deformation in a Microchannel with a Non-Newtonian Fluid. *Biomicrofluidics* **12**, 1–11 (2018).

185. Krindel, P. *et al.* A. Flow Through Gel-Walled Tubes. *J Colloid Interface Sci* **71**, (1979).

186. Verma, M. K. S. *et al.* A Dynamical Instability due to Fluid-Wall Coupling Lowers the Transition Reynolds Number in the Flow through a Flexible Tube. *J Fluid Mech* **705**, 322–347 (2012).

187. Gervais, T. *et al.* Flow-Induced Deformation of Shallow Microfluidic Channels. *Lab Chip* **6**, 500–507 (2006).

188. Benschop, H. O. G. *et al.* Deformation of a Linear Viscoelastic Compliant Coating in a Turbulent Flow. *J Fluid Mech* **859**, 613–658 (2019).

189. Rosti, M. E. *et al.* Numerical Simulation of Turbulent Channel Flow over a Viscous Hyper-Elastic Wall. *J Fluid Mech* **830**, 708–735 (2017).

190. Wang, J. *et al.* On the Interaction of a Compliant Wall with a Turbulent Boundary Layer. *J Fluid Mech* **899**, (2020).

191. Fisher, T. L. M. *et al.* Investigation of the Stable Interaction of a Passive Compliant Surface with a Turbulent Boundary Layer. *J Fluid Mech* **257**, 373–401 (1993).

192. Verma, M. K. S. *et al.* A Multifold Reduction in the Transition Reynolds Number, and Ultra-Fast Mixing, in a Micro-Channel due to a Dynamical Instability Induced by a Soft Wall. *J Fluid Mech* **727**, 407–455 (2013).

193. Neelamegam, R. *et al.* Experimental Study of the Instability of Laminar Flow in a Tube with Deformable Walls. *Physics of Fluids* **27**, (2015).

194. Nieman, M. *et al.* A Syringe Pump Tester. *J Med Eng Technol* **10**, 255–258 (1986).

195. Philip, J. P. *et al.* *Fox and McDonald's Introduction to Fluid Mechanics*. (John Wiley & Sons, Ltd, Oxford, UK, 2011).

196. Ēengel, Y. A. *et al.* Essentials of Fluid Mechanics: Fundamentals and Applications. (McGraw-Hill Science/Engineering/Math, 2008).

197. Xue, L. *et al.* A. Stick-Slip Friction of PDMS Surfaces for Bioinspired Adhesives. *Langmuir* **32**, 2428–2435 (2016).

198. Kim, J. *et al.* Hydrophobic Recovery of Polydimethylsiloxane Elastomer Exposed to Partial Electrical Discharge. *J Colloid Interface Sci* **226**, 231–236 (2000).

199. Herrmann, D. B. Diffusion of Water through Organic Insulating Materials. *Rubber Chemistry and Technology* **8**, 297–301 (1935).

200. Watson, J. M. *et al.* The Behaviour of Water in Poly(Dimethylsiloxane). *J Memb Sci* **110**, 47–57 (1996).

201. Law, K. Y. *et al. Surface Wetting: Characterization, Contact Angle, and Fundamentals*. (Springer, 2015).

202. Ibáñez-Ibáñez, P. F. *et al.* Contact Line Relaxation of Sessile Drops on PDMS Surfaces: a Methodological Perspective. *J Colloid Interface Sci* **589**, 166–172 (2021).

203. Martin, S. *et al.* Transparent, Wear-Resistant, Superhydrophobic and Superoleophobic Poly(Dimethylsiloxane) (PDMS) Surfaces. *J Colloid Interface Sci* **488**, 118–126 (2017).

204. Wang, X. *et al.* Theory of the Flow-Induced Deformation of Shallow Compliant Microchannels with Thick Walls. *Proceedings of the Royal Society A: Mathematical, Physical and Engineering Sciences* **475**, (2019).

205. Dhong, C. *et al.* Role of Indentation Depth and Contact Area on Human Perception of Softness for Haptic Interfaces. *Sci Adv* **5**, (2019).

206. Kumaran, V. Experimental Studies on the Flow Through Soft Tubes and Channels. *Sadhana - Academy Proceedings in Engineering Sciences* **40**, 911–923 (2015).

207. Kumaran, V. *et al.* Flow Induced Instability of the Interface Between a Fluid and a Gel at Low Reynolds Number. *J Phys II France* **4**, 893–911 (1994).

208. Shankar, V. Stability of Fluid Flow through Deformable Tubes and Channels: an Overview. *Sadhana - Academy Proceedings in Engineering Sciences* **40**, 925–943 (2015).

209. Chokshi, P. *et al.* Stability of the Viscous Flow of a Polymeric Fluid Past a Flexible Surface. *Physics of Fluids* **19**, 034102 (2007).

210. Hourlier-Fargette, A. *et al.* Role of Uncrosslinked Chains in Droplets Dynamics on Silicone Elastomers. *Soft Matter* **13**, 3484–3491 (2017).

211. Glover, J. D. *et al.* Extracting Uncrosslinked Material from Low Modulus Sylgard 184 and the Effect on Mechanical Properties. *Journal of Polymer Science* **58**, 343–351 (2020).

212. Ebrahimi, A. P. Mechanical Properties of Normal and Diseased Cerebrovascular System. *J Vasc Interv Neurol* **2**, 155–62 (2009).

213. Monson, K. L. *et al.* Axial Mechanical Properties of Fresh Human Cerebral Blood Vessels. *J Biomech Eng* **125**, 288–294 (2003).

214. Arieli, R. *et al.* Evolution of Bubbles from Gas Micronuclei Formed on the Luminal Aspect of Ovine Large Blood Vessels. *Respir Physiol Neurobiol* **188**, 49–55 (2013).

215. Ng Lee, J. *et al.* Solvent Compatibility of Poly(dimethylsiloxane)-Based Microfluidic Devices. *analysitcal chemisty* **45**, 6544–6554 (2003).

216. Butt, H. J. *et al.* Force Measurements with the Atomic Force Microscope: Technique, Interpretation and Applications. *Surface Science Reports* **59**, 1–152 (2005)

217. Liu, K. K. Deformation Behaviour of Soft Particles: A review. *J Phys D Appl Phys* **39**, (2006).

218. Prokopovich, P. *et al.* Adhesion Models: from Single to Multiple Asperity Contacts. *Adv Colloid Interface Sci* **168**, 210–222 (2011).

219. Erath, J. *et al.* Characterization of Adhesion Phenomena and Contact of Surfaces by Soft Colloidal Probe AFM. *Soft Matter* **6**, 1432–1437 (2010).

220. Maugis, D. Extension of the Johnson-Kendall-Roberts Theory of the Elastic Contact of Spheres to Large Contact Radii. *Langmuir* **11**, 679–682 (1995).

221. Maugis, D. Adhesion of spheres: The JKR-DMT transition using a Dugdale Model. *J Colloid Interface Sci* **150**, 243–269 (1992).

222. Kim, A. *et al.* Capillary Pressure Mediated Long-Term Dynamics of Thin Soft Films. *J Colloid Interface Sci* **628**, 788–797 (2022).

223. Young, T. An Essay on The Cohesion of Fluids. *Probation* **9**, 3–4 (1804).

224. de Gennes, P. G. Wetting: Statics and Dynamics. *Rev Mod Phys* **57**, 827–863 (1985).

225. de Gennes, P. G. *et al. Capillarity and Wetting Phenomena Drops, Bubbles, Pearls, Waves*. (Springer, 2002).

226. Salez, T. *et al.* From Adhesion to Wetting of a Soft Particle. *Soft Matter* **9**, 10699–10704 (2013).

227. Long, J. *et al.* Effects of Surface Tension on the Adhesive Contact between a Hard Sphere and a Soft Substrate. *Int J Solids Struct* **84**, 133–138 (2016).

228. Zhang, L. *et al.* A Refined JKR Model for Adhesion of a Rigid Sphere on a Soft Elastic Substrate. *Journal of Applied Mechanics, Transactions ASME* **86**, (2019).

229. Xu, X. *et al.* Effects of Surface Tension on the Adhesive Contact of a Rigid Sphere to a Compliant Substrate. *Soft Matter* **10**, 4625–4632 (2014).

230. Hui, C. Y. *et al.* Indentation of a Rigid Sphere into an Elastic Substrate with Surface Tension and Adhesion. *Proceedings of the Royal Society A: Mathematical, Physical and Engineering Sciences* **471**, (2015).

231. Cao, Z. *et al.* Adhesion and Wetting of Nanoparticles on Soft Surfaces. *Macromolecules* **47**, 3203–3209 (2014).

232. Ally, J. *et al.* Interaction of a Microsphere with a Solid-supported Liquid Film. *Langmuir* **26**, 11797–11803 (2010).

233. Liu, L. *et al.* Capillary Force in Adhesive Contact between Hydrogel Microspheres. *Colloids Surf A Physicochem Eng Asp* **611**, 125828 (2021).

234. Sokoloff, J. B. Effects of Capillary Forces on a Hydrogel Sphere Pressed against a Surface. *Langmuir* **32**, 135–139 (2016).

235. Yin, C. *et al.* Visible Light-Driven Jellyfish-like Miniature Swimming Soft Robot. *ACS Appl Mater Interfaces* **13**, 47147–47154 (2021).

236. Leber, A. *et al.* Stretchable Thermoplastic Elastomer Optical Fibers for Sensing of Extreme Deformations. *Adv Funct Mater* **29**, 1–8 (2019).

237. Shyam, S. *et al.* Universal Capillary-Deflection Based Adhesion Measurement Technique. *J Colloid Interface Sci* **630**, 322–333 (2022).

238. J.F., J. *et al.* Gels at Interfaces. *EPJE* **6**, 201–209 (2001).

239. Maugis, D. *Contact, Adhesion and Rupture of Elastic solids*. (Springer Science & Business Media, 2000).

240. Tatara, Y. On Compression of Rubber Elastic Sphere Over a Large Range of Displacements-Part 1: Theoretical Study. *J Eng Mater Technol* **113**, 285–291 (1991).

241. Maugis, D. *et al*. Surface Forces, Deformation and Adherence at Metal Microcontacts. *Acta Metall* **32**, 1323–1334 (1984).

242. Style, R. W. *et al.* Universal Deformation of Soft Substrates Near a Contact Line and the Direct Measurement of Solid Surface Stresses. *Phys Rev Lett* **110**, 066103 (2013).

Appendix A

A.1 Experimental

Dynamic viscosity of lubricant - The shear viscosity of glycerol was analyzed using a dynamic shear rheometer (Kinexus Rotational Rheometer, Malvern Instruments) at 25 °C. A cup and bob geometry was used, with a rotating cylinder inserted inside of the cup. Glycerol was exposed to atmospheric conditions for 24 hours before friction tests due to its hygroscopic nature, so the glycerol used to measure viscosity was also prepared in the same manner. The temperature of glycerol was equilibrated for 5 min before testing. Shear viscosity was measured at different shear rates (0.1 – 650 s^{-1}).

A.2 Results and Discussion

Viscosity of lubricants - The shear viscosity of glycerol was measured over shear rates of 0.1 – 650 s^{-1} (see Fig. A.2.5). Due to its Newtonian behavior, the viscosity remained constant at $\sim$ 0.9002 $\mathrm{Pa \cdot s}$. Literature value for the shear viscosity of water (over a range of shear rates) of $0.8 \cdot 10^{-3}$ $\mathrm{Pa \cdot s}$ used in this work.[115]

Friction measurement between a PDMS probe and a glass substrate - To test the stability of our experimental set-up and compare our systems with previous research, which studied soft-hard contacts mostly, a glass substrate with an elastic modulus of 70,000 MPa,[116] replacing a PDMS substrate, was used as a bottom substrate in dry conditions. Friction traces were obtained like Fig. A.2.1(b). In Fig. A.2.1(c), as the preload decreases and the sliding velocity increases, the friction coefficient increases which is similar to the results from literature.[65,83] The standard deviations of experimental data obtained through three to four times repeated tests present have less than 5% on average.

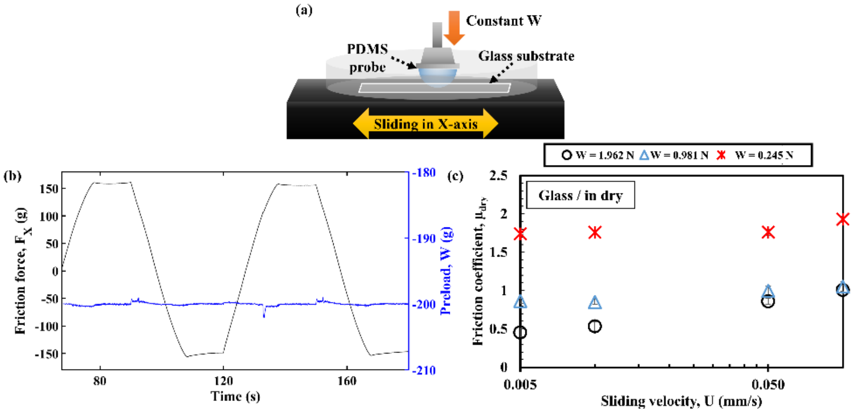

Figure A.2.1 Friction measurement between a PDMS probe and a glass slide in dry condition: the bottom glass substrate attached in a petri dish travels in x-axis against a stationary PDMS probe at a constant sliding velocity and a constant preload. **(a)** Experimental set-up. **(b)** A representative friction trace at a preload of 200 g and a sliding velocity of 0.1 mm/s. **(c)** The friction coefficient against the sliding velocity at the preloads of 25, 100, and 200 g. Error bars represent standard deviation, though some are smaller than the size of the data point.

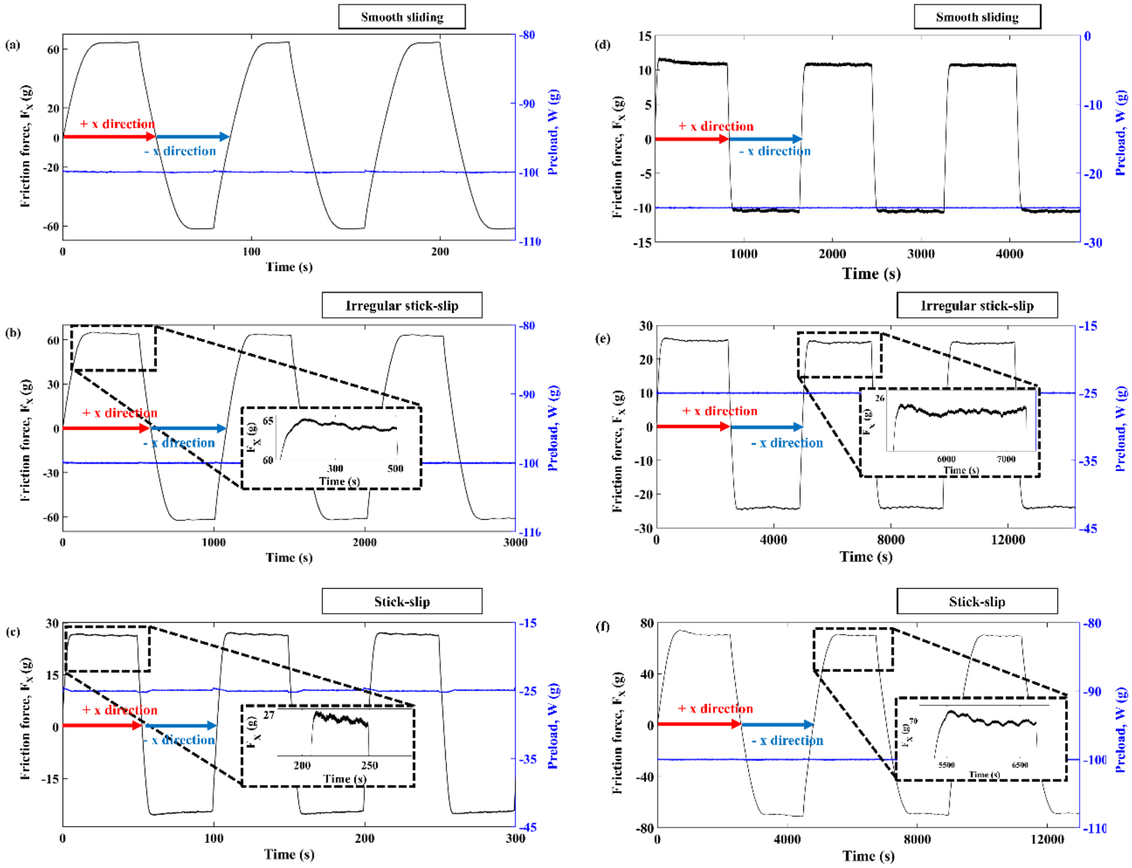

Figure A.2.2 Representative friction traces. In dry, **(a)** smooth sliding was obtained with a P20 substrate at the sliding velocity of 0.05 mm/s under the preload of 100 g, **(b)** irregular stick-slip friction was presented with a P30 substrate at the sliding velocity of 0.01 mm/s under the preload of 100 g, and **(c)** stick-slip friction was observed with a P10 substrate at the sliding velocity of 0.1 mm/s under the preload of 25g. In lubricated condition, **(d)** smooth sliding was obtained in the water with a P10 substrate at the sliding velocity of 0.005 mm/s under the preload of 25 g, **(e)** irregular stick-slip friction was shown in the water with a P10 substrate at 0.005 mm/s under the preload of 25 g, and **(f)** stick-slip friction was presented in the water with a P40 substrate at 0.005 mm/s under the preload of 100 g.

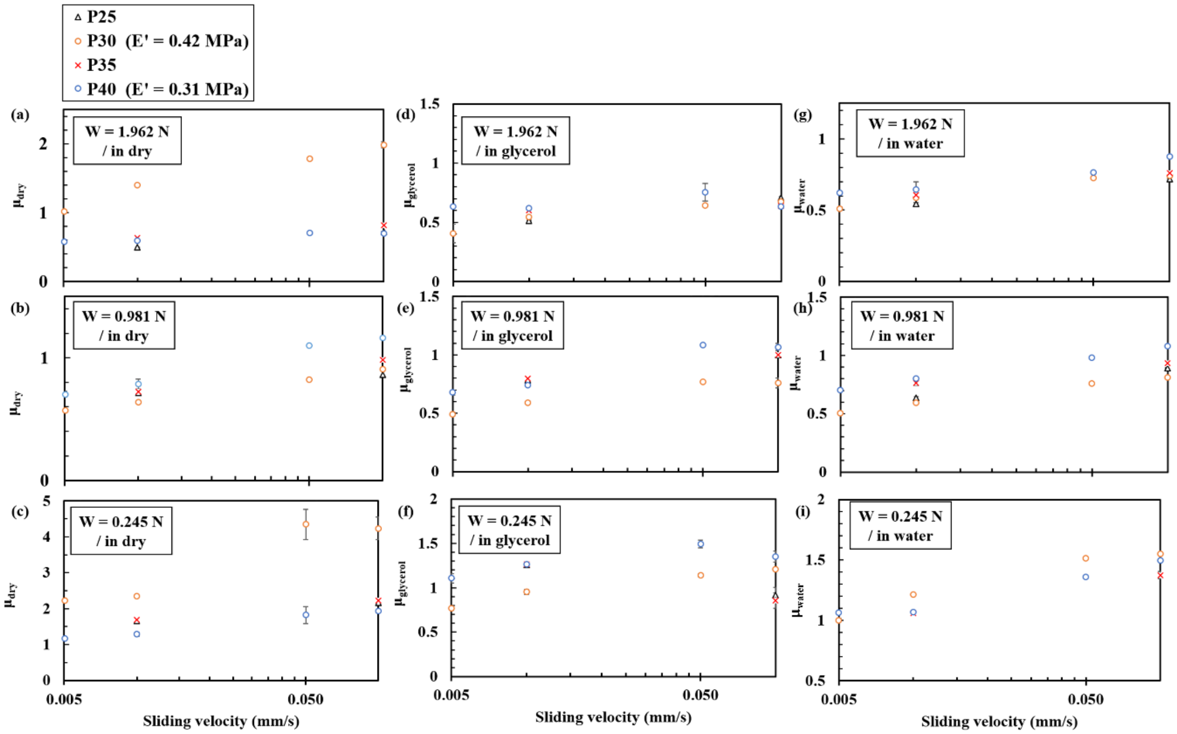

Figure A.2.3 The plot of the friction coefficient (between a P10 probe and P25 – P40 substrates) against the sliding velocity. In dry conditions, the friction force was measured at the preloads of **(a)** 1.962, **(b)** 0.981, and **(c)** 0.245 N. In glycerol lubricated conditions, the friction force was examined at the preloads of **(d)** 1.962, **(e)** 0.981, **(f)** 0.245 N. In water lubricated conditions, the friction was tested at the preloads of **(g)** 1.962, **(h)** 0.981, and **(i)** 0.245 N. To improve readability, the friction coefficient between a P10 probe, and P10 and P20 substrates are not included in this figure. Error bars represent standard deviation, though some are smaller than the size of the data point.

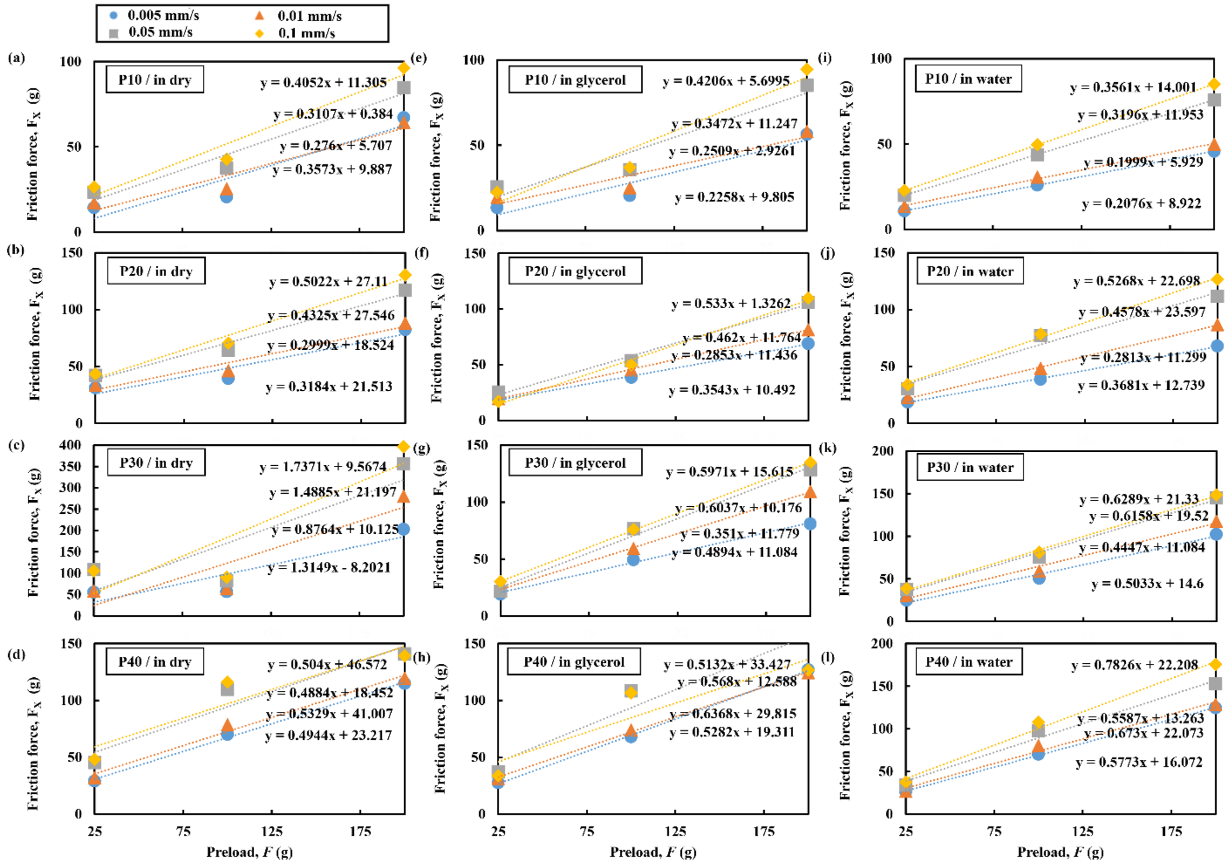

Figure A.2.4 The friction force (F_X) against the preload (*F*) for each substrate at different sliding velocities. In dry condition, the friction force was measured with **(a)** P10, **(b)** P20, **(c)** P30, and **(d)** P40 substrate. In glycerol-lubricated condition, the friction force was measured with **(e)** P10, **(f)** P20, **(g)** P30, and **(h)** P40 substrates. In water-lubricated condition, the friction force was measured with **(i)** P10, **(j)** P20, **(k)** P30, and **(l)** P40 substrate.

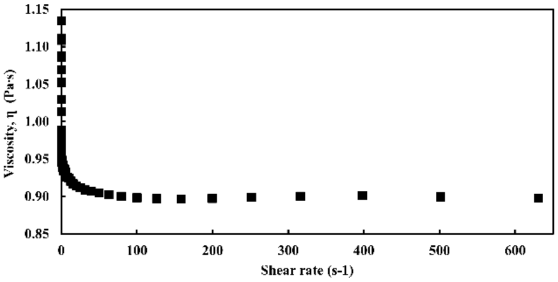

Figure A.2.5 Dynamic viscosity of glycerol: (after being exposed in the air for 24 hours) obtained from the rheometer over shear rates of 0.1 – 650 s^{-1}.

Table A.2.1 Friction modes of each friction trace for dry and lubricant contacts: "smooth" denotes smooth sliding, "s-s" denotes stick-slip sliding, and "I s-s" refers to irregular stick-slip sliding.

Experimental conditions			**Dry**	**Glycerol**	**Water**
Substrate	Preload, W (g)	**Sliding velocity, U (mm/s)**	**Friction mode**		
P10	25	0.005	Smooth	s-s	Smooth
		0.01	s-s	Smooth	I s-s
		0.05	Smooth	Smooth	s-s
		0.1	s-s	I s-s	s-s
	100	0.005	Smooth	I s-s	Smooth
		0.01	Smooth	s-s	Smooth
		0.05	Smooth	s-s	Smooth
		0.1	Smooth	s-s	I s-s
	200	0.005	Smooth	Smooth	Smooth
		0.01	Smooth	Smooth	Smooth
		0.05	Smooth	Smooth	Smooth
		0.1	Smooth	Smooth	s-s
P20	25	0.005	Smooth	Smooth	Smooth
		0.01	Smooth	Smooth	Smooth
		0.05	Smooth	Smooth	Smooth
		0.1	Smooth	I s-s	Smooth
	100	0.005	Smooth	s-s	Smooth
		0.01	Smooth	I s-s	Smooth
		0.05	Smooth	I s-s	Smooth
		0.1	Smooth	I s-s	Smooth
	200	0.005	Smooth	Smooth	Smooth
		0.01	Smooth	Smooth	Smooth
		0.05	Smooth	Smooth	Smooth

		0.1	Smooth	Smooth	Smooth
P30	25	0.005	Smooth	s-s	I s-s
		0.01	I s-s	s-s	Smooth
		0.05	s-s	I s-s	Smooth
		0.1	s-s	I s-s	Smooth
	100	0.005	I s-s	s-s	I s-s
		0.01	I s-s	s-s	I s-s
		0.05	I s-s	I s-s	I s-s
		0.1	s-s	I s-s	I s-s
	200	0.005	Smooth	s-s	Smooth
		0.01	Smooth	Smooth	Smooth
		0.05	Smooth	Smooth	Smooth
		0.1	Smooth	s-s	Smooth
P40	25	0.005	Smooth	Smooth	s-s
		0.01	Smooth	Smooth	Smooth
		0.05	I s-s	Smooth	Smooth
		0.1	I s-s	I s-s	Smooth
	100	0.005	I s-s	s-s	s-s
		0.01	I s-s	Smooth	Smooth
		0.05	Smooth	s-s	Smooth
		0.1	I s-s	Smooth	Smooth
	200	0.005	Smooth	I s-s	Smooth
		0.01	Smooth	I s-s	Smooth
		0.05	Smooth	I s-s	I s-s
		0.1	Smooth	I s-s	I s-s

Table A.2.2 Regression relations: between the empirical friction coefficient (μ) and other key parameters (the sliding velocity (U), the preload (F), the lubricant viscosity (η), the reduced elasticity (E^*), the loss tangent ($tan\ \delta$), the storage modulus of the substrate (E')): E^*, $tan\ \delta$ and E' are obtained at 0.1 and 1 Hz.

Hz	**Dry condition**	**Adjusted $\mathbf{R^2}$**	**Lubricated condition**	**Adjusted $\mathbf{R^2}$**
0.1	$\mu_{dry} \sim \frac{E^{*4.123} U^{0.175}}{E'^{3.781} (tan\delta)^{3.827} F^{0.451}}$	0.813	$\mu_{lubricated} \sim \frac{U^{0.151}}{\eta^{0.011} E'^{0.163} (tan\delta)^{0.286} F^{0.333}}$	0.89
1	$\mu_{dry} \sim \frac{E^{*3.363} U^{0.175}}{(E' tan\delta)^{3.754} F^{0.451}}$	0.813	$\mu_{lubricated} \sim \frac{U^{0.151}}{\eta^{0.011} (E' tan\delta)^{0.281}\ F^{0.333}}$	0.888

Appendix B

B.1 Experimental

AFM observation - Atomic force microscopy (AFM) (MFP-3D BIO (Asylum Research, Santa Barbara, CA, USA) was used to image the surface roughness of bare glass slides and glass spheres. Before observations, the glass slides and spheres were thoroughly washed in a sonicator using acetone, IPA, and then DI water. Then, the surface roughness was measured by tapping mode, as shown in Figure B.3.1.

Solvent extraction - We poured 2.0 g prepolymer of each silicone elastomer (after mixing in each weight ratio as mentioned in the previous section) in a rectangular metal mold with 2 cm × 2 cm dimensions. The prepolymers were cured in an oven at 80 °C for 12 – 14 hours, and then the samples were removed carefully. The fully cured samples were placed in large jars filled with pentane for one week, replacing the pentane every two days. Finally, the fully swollen samples were dried for two to three days at room temperature (22 – 24 °C). Before pentane treatment and after the dry step, the weight of samples was measured. Three individual samples were tested. The elastomer and gel were determined to contain a 4.9 and 62 wt.% fraction of liquids, respectively.

DW-RICM technique (image acquisition and processing) - The geometry of the contact was investigated using dual wavelength-reflection interference contrast microscopy (DW-RICM) (Zeiss LSM 800 confocal microscopy)[142,167,168] and a side-view camera (BASLER acA1920 – 155 μm). An LED backlight was used with the side-view camera. In DW-RICM, the objective used had magnifications M = 10× and 40× with numerical apertures (NA) = 0.3 and 0.085, respectively. We raster-scanned the surface of interest (the surface of a glass sphere or each soft film) over an area of 200 – 1830 μm × 200 – 1830 μm simultaneously with two focused beams of monochromatic lights with wavelengths $\lambda_g = 488$ nm and $\lambda_r = 561$ nm (g = green, r = red). The reflected light from the focal plane was collected through the pinhole of a confocal microscope and then reached the photomultiplier tube of the microscope. This is crucial to observe only the interface of interest without the stray light reflected from other planes. The maximum dwell-time of each pixel (size: 0.45 μm) was 8.24 μs, and the laser-scanning microscope (LSM) speed was 2. Hence, the frame time (4096 × 4096 pixels in size) was 5 min 50 seconds with 8 bits per pixel. We set the radial direction (r-axis) by the x and y coordinates: $r = \sqrt{(x - a_x)^2 + (y - a_y)^2}$ with respect to the center of the glass sphere (a_x, a_y), which is an origin of the reconstructed surface profile. We measured the light intensities along the radial direction, and then normalized, as described below:

$$\widetilde{I_r} = \frac{I_r - I_{min}}{I_{max} - I_{min}} \tag{B.3.1}$$

where $\widetilde{I_r}$ is the normalized light intensity, and I_{max} and I_{min} indicates the experimental maximum and minimum light intensities, respectively. In the glass-gel-glass contact, the normalized light intensities were filtered again according to the moving-average to reduce noises in the intensities (Fig. B.3.2). The size of the optical slice dz is determined according to[169]:

$$dz(PH) = \sqrt{\left(\frac{\lambda n}{NA^2}\right)^2 + \left(\frac{n\sqrt{2}PH}{NA}\right)^2} \approx \frac{n\sqrt{2}PH}{NA} \tag{B.3.2}$$

where PH is the size of the pinhole, λ is the wavelength of monochromatic light, and n is the refractive index of an intermediate medium (air in case of glass-glass contact, and soft (elastomer or gel) films in case of glass-elastomer-glass and glass-gel-glass contact). dz is varied from 26 – 160 μm depending on the magnifications. The fringes are reliable as long as the slope of the interference, $\frac{dh}{dr}$ is less than the maximal slope, denoted by $\left.\frac{dh}{dr}\right|_{max}$:

$$\left.\frac{dh}{dr}\right|_{max} = \frac{n}{n_3}(NA - INA) \tag{B.3.3}$$

where h is the local gap distance between the two interfaces where reflection occurs, n is the refractive index of the corresponding medium, n_3 is the reflective index of the glass sphere, and INA is the numerical illumination aperture. INA can be ignored because only the incident and reflected light rays parallel to the optical axis are considered without considering the curved interface. We assume that the surface where light rays reflect consists of infinitesimally small flat planes.

Materials where incident rays transmit (*e.g.*, glass, elastomer, and gel) are non-magnetic and isotropic. Therefore, only an electric field is considered. The incident light beams are reflected off the bottom (electric field H', with an intensity I') and the top interfaces (H'', I''), and create the resultant electric field H_r, which are given by[170]:

$$H_r = |H'| + |H''| \exp(i\varphi) = |H'| + |H''|\{cos(\varphi) + isin(\varphi)\} \qquad \text{(B.3.4)}$$

where φ is the phase difference between H' and H''. The resultant (measured) light intensity I_r can be theoretically expressed via E_r:

$$I_r \propto |H_r|^2 = I' + I'' + 2\sqrt{I'I''}cos\varphi \qquad \text{(B.3.5)}$$

Therefore, one knows that the phase difference brings alternative constructive and destructive interference fringes. The resultant local light intensity is measured from an interferogram obtained using DW-RICM, where $\widetilde{I_r}$ is the normalized light intensity, and I_{max} and I_{min} indicate the experimental maximum and minimum light intensities in the interferogram, respectively ($I_{max} = I' + I'' + 2\sqrt{I'I''}, I_{min} = I' + I'' - 2\sqrt{I'I''}$). By plugging I_{max} and I_{min}, the normalized light intensity is written as a function of the phase difference:

$$\widetilde{I_r} = \frac{cos\varphi + 1}{2} \qquad \text{(B.3.6)}$$

where φ can be calculated as:

$$\varphi = \frac{4n\pi h}{\lambda}, \text{or} \qquad \text{(B.3.7)}$$

$$\varphi = \frac{4n\pi h}{\lambda} + \pi \qquad \text{(B.3.8)}$$

where λ is the wavelength of monochromatic light ($\lambda_g = 488$ nm, and $\lambda_r = 561$ nm). Equation B.3.7 is valid for contact components with continuously increasing or decreasing refractive indices, *i.e.*, soft-rigid contact. Otherwise, we use Equation B.3.8 to consider π-shift. This normalized light intensity is filtered according to the moving-average, before calculating the gap distance (explained in the following section). When the gap distance between interference rings increases, the noise level increases proportionally. Therefore, we used a 15 – 27 points-moving average for the first 2/3 area and a 5 points-moving average for the rest section. The phase difference also can be written as:

$$\varphi = 2M\pi, \text{or} \tag{B.3.9}$$

$$\varphi = (2M+1)\pi \tag{B.3.10}$$

where M is the integer, the order of the corresponding interference ring (peak). Therefore, each interference peak point has a height increment $\frac{\lambda}{2n}$ compared to the previous peak point. By rearranging Equations B.3.5 and 6, the gap height can be found as follows:

$$h = arcos\left\{2\left(\frac{I_r - I_{min}}{I_{max} - I_{min}}\right) - 1\right\} \times \frac{\lambda}{4n_{film}\pi}. \tag{B.3.11}$$

For a simple sphere geometry, h can also be calculated according to:

$$h(r_m) = \frac{\lambda m}{2n} - R + \sqrt{R^2 - r_m^2} \tag{B.3.12}$$

where R is the sphere's radius, and r_m is the radius of the mth interference ring. The relative local height of interest was calculated based on the local intensity maxima and minima on the radial line according to:

$$h(r) = \sum_{1}^{N} \frac{\lambda}{4n} \tag{B.3.13}$$

where N is the number of peak points. We used the refractive indices of glass slides and glass spheres as $n_1 = n_3 = 1.5$[141]. The elastomer and gel's refractive indices were measured using reflectometry: n_4 (elastomer) = 1.41 and n_5(gel) = 1.4 (see Fig. B.3.3). We collected a constant number of pixels at the magnification ×40, corresponding to the actual distance, 390.156 μm, to improve the data consistency considering that we extrapolate the rest of the gel profile. We calculated the relative profile change by modifying the MATLAB codes written by Misra *et al.*[143].

Raw intensity data filtration - Intensities collected using DW-RICM contain noises due to the background light, micro-and nano-sized dust, and interferences of refracted rays from different planes, which are not the planes of interest. Especially, measured refractive light presents more noises when the light transmits soft materials, not glasses or glass spheres, as shown in Figure B.3.2. When we collected light intensities in the radial direction, several peaks from stray light were captured even on single constructive and destructive rings. Over the whole length of the radial distance, each peak point (constructive and destructive rings) seemingly looks clear (Fig. B.3.2(a)). However, in the enlarged view, one peak point (red box *a*) contains ~ 13 sub-peak points (Figs. B.3.2(b) and (c)). These false peaks bring exaggerated and steeper gel profiles into the analysis process. Therefore, we used the moving-average filter based on the following equation:

$$I_{ave}(m) = \frac{1}{3}\{I(m-1) + I(m) + I(m+1)\} \tag{B.3.14}$$

where $I(m)$ is the measured raw intensity at the mth order and $I_{ave}(m)$ is the filtered intensity of the nth data point. In Equation B.3.14, since three intensities are used to create the average value, the sum of each intensity is divided by 3. When the number of summed individual data increases, the averaged intensity becomes smoother with fewer noises, but at the same time, the original sinusoidal fluctuation of the intensity disappears. As shown in Figures B.3.2(b), (c), and (e), we tested 5, 10, and 15 as the number of summed intensities. For comparison, we deposited one droplet of silicone oil between a glass sphere and glass slide, and the resultant light intensity is much clearer with negligible noises (Figs. B.3.2(d) and (e)).

Tensile testing - Elastic moduli of elastomer films were investigated using a universal macro-tribometer (UMT-2MT, Center for Tribology, Inc.). Specific processes of mixing and polymerization are the same as mentioned earlier. 2 mm thick films of each elastomer were fabricated using glass Petri dishes (Diameter:

100 mm) as molds. After fully curing and cooling, the films were cut from the Petri dish in 10 mm × 60 mm (width × height) using a scalpel. We used a load cell with a maximum capacity of 100 N. Samples were secured into clamps, and the initial gap distance between each clamp was 30 mm. Crosshead velocity was 254 mm/min. The real-time normal force was recorded with 200 Hz at 23 °C. Elastic modulus was calculated in the linear elastic region, up to a strain value of ~ 0.4. The measured elasticity and the linear region of the strain are in good agreement with the previous work by Johnston *et al.*[92]. Each sample was tested 3 – 4 times for repeatability.

Refractive index measurement - Silicon wafers with 150 mm diameter were diced in 50 mm × 50 mm. The diced wafers were washed using acetone and then IPA for 15 min, each, sequentially, in a sonicator bath. We rinsed the wafers using DI water and then dried them sufficiently using N_2 gas. Elastomer and gel prepolymers were spin-coated on the wafers at different speeds of 5000 – 9000 rpm for 100 s. As a result, elastomer and gel films with thicknesses between 3 and 8 μm were fabricated. A Filmetrics (F50) analyzer over a 400 – 900 nm spectral range measured the refractive indices and the film thickness. Sellmeier model was used to analyze the refractive index[171]. The measurements' overall goodness-of-fit (GOF) was 0.991 for elastomer films and 0.994 for gel films. The refractive index of the elastomer film is 1.41 ± 0.001 at both wavelengths of 488 and 561 nm. The gel film has a refractive index of 1.40 ± 0.0001 at 488 nm and 561 nm, as shown in Figure B.3.3.

Volume calculation - Each volume (V_{indent} and V_{ridge}) was calculated based on the examined surface area of each section and the MATLAB built-in function trapz(). An equation for the circle (glass sphere) can be arranged as a function of h, $r = f(h) = \sqrt{2600^2 - (h - 2803.959)^2} - H$ where H is the gel film thickness. The submerged depth of the glass sphere is calculated from the observed contact radius using DW-RICM. In the case of the gel film, the calculated coordinates (r, h) from an interferogram are used to calculate the profile of the rigid and liquid components. By summing up all the infinitesimally small cross-sectional areas in the perpendicular direction to the z-axis as shown in Fig. B.3.10(b), V_{indent} can be calculated as:

$$V_{indent} = \pi \int_{D}^{0} r^2 dh = \pi \int_{D}^{0} f(h)^2 dh \tag{B.3.15}$$

where V_{indent} is the volume of the segment of a curve, $r = f(h)$ between $h = 0$ and $D =$ the indentation depth revolving around the z-axis. The phase-separated liquid and gel sections in the ridge were calculated simultaneously due to the slight difference in each reflective index. Therefore, the separate calculation of each volume of the elastic-network-based ridge and the liquid-based ridge was unavailable. Hence, we calculated V_{ridge} composed of the free liquids and elastic network together, according to:

$$V_{ridge} = \pi \int_{0}^{\delta} g(h)^2 dh - \pi \int_{0}^{\delta} f(h)^2 dh \tag{B.3.16}$$

where $g(h)$ is a function composed of the calculated and extrapolated discrete data points of gel surface profile collected every 1.8 μm along with the radial distance. The calculated discrete data points were based on the measured light intensity, collected only up to ~ 700 μm radial distance due to the limited observable area using DW-RICM. The rest of the surface profile of the gel was extrapolated using MATLAB built-in function interp1(). The extrapolated line was created considering the calculated profile of the gel. The volume of the glass sphere on the free gel surface was subtracted from the volume obtained by rotating the ridge profile on the unperturbed gel surface between $\delta =$ the ridge height and $h = 0$ around the $z-$axis. Eventually, the 3D view of the contact zone of the glass-gel-glass contact is shown in Figure B.3.10(c).

Comparison with Hertz contact theory - Using a custom-built micro-indenter, we measured the force against the indentation depth between the soft film and glass sphere to examine any possible plastic deformation on soft films. Detail explanation of the instrument is given in the work by Cholewinski *et al.*[172]. We prepared each soft film of elastomer and gel as mentioned above, but sufficiently thick films (2 – 3 mm) were fabricated to compare the experimental results with the conventional Hertz theory. The glass sphere with a radius of 2.6 mm was used as the probe. The force and displacement were recorded at 50 Hz. The glass probe was moved toward the soft films at the constant rates of 5 μm/s (for elastomer) and 1 μm/s (for gel) till the indentation force reached 50 mN (for elastomer) and 0.28 mN (for gel). Once the force reached the set forces, the probe was withdrawn from the soft films at 100 μm/s. The Hertzian force (F_H) of elastomer and gel was plotted along with the experimental data in Figure B.3.11: $F_H = \frac{4}{3}E^* R^{0.5} D^{1.5}$ [149].

Contact angle and surface tension measurement - Static contact angles of the gel base on a glass slide were measured under ambient conditions at 20 °C on a drop analyzer (Krüss, DSA30). A 10 μl droplet of the gel base was dispensed on the glass slide. The static contact angles were measured two times, right after the deposition and after 20 min. The angle decreased from ~ 40 ° to ~ 4 ° (see Fig. B.3.13). The surface tension of DMS-V31 base polymer and silicone oils was measured using the pendant drop method. 21 G needles (width: 0.8 mm) were used for DMS-V31 base, and 25 G needles (width: 0.5 mm) were used for silicone oils to dispense 3 – 4 μl droplets of each liquid at a rate 0.2 μl/s. The surface tension was measured based on the Young-Laplace equation programmed on the ADVANCE software (Krüss)[173]. Each measurement was repeated three times (see Fig. B.3.14). The surface energy of the glass (γ_1) is 64 mN/m [174,175]. The measured surface tension of the gel base (γ_2) is 20 mN/m (see Fig. B.3.14(a)). Based on Young's law, the interfacial tension between the glass sphere and gel is calculated as γ_{12} ~ 44 mN/m, assuming the surface energy of the gel is equal to the surface tension of the gel base[53].

Contact area with the finite-size effect - In the glass-elastomer-glass and glass-gel-glass contact, the ratio of the contact radius (a) to the tested film thickness of elastomer and gel (H) is larger than the assumption of the Hertz and JKR theories ($a/H \sim 0$), wherein the film cannot be considered as a semi-infinite film. Hence, we considered the finite-size effects and calculated the Hertzian and JKR contact radius[176]. The Hertzian indenter load (F_H) is calculated according to:

$$F_H = \frac{4E^* a^3}{3R} \tag{B.3.17}$$

The Hertzian indentation depth (D_H) is calculated according to:

$$D_H = \frac{a^2}{R} \tag{B.3.18}$$

In cases where the soft film thickness is relatively smaller than the contact radius, the film is not an elastic half-space anymore. Therefore, the modified Hertzian theory can be applied, assuming non-adhesive and frictionless contact. This modified theory assumes that the soft film is confined between two rigid components (here, a glass slide and a glass sphere). The relative thickness ratio, a/H is a critical factor. The Hertzian load is approximated as[138]:

$$F'_H = F_H f_p\left(\frac{a}{H}\right) \tag{B.3.19}$$

where $f_p\left(\frac{a}{H}\right) = \left(1 + \beta\left(\frac{a}{H}\right)^3\right)$; where β is 0.33 for the full-friction case and 0.15 for the frictionless condition[177]. The elastomer and glass sphere have significant friction, preventing sliding of each surface[144]. Hence, we assume the full-friction condition. The Hertzian indentation depth is similarly approximated as:

$$D'_H = D_H f_D\left(\frac{a}{H}\right) \tag{B.3.20}$$

where $f_D\left(\frac{a}{H}\right) = \left(0.4 + 0.6\exp\left(\frac{-1.8a}{H}\right)\right)$. By plugging in the correction factor, $f_p\left(\frac{a}{H}\right)$ in Equation B.3.19, we obtain the following implicit relation:

$$F'_H = \frac{4E^*a^3}{3R}\left(1 + 0.33\left(\frac{a}{H}\right)^3\right) \tag{B.3.21}$$

The applied load does not change as it is purely from the weight of the glass sphere (1.24 mN measured using a scale). Therefore, the corresponding Hertzian contact radius is 80 µm with Equation B.3.21.

To consider the finite-size effect based on the conventional JKR theory, the modified JKR indentation depth is expressed as:

$$D'_{JKR} = \frac{a^2}{R} f_D\left(\frac{a}{H}\right) + \frac{f_c\left(\frac{a}{H}\right)}{2E^*a}\left(P - \frac{4E^*a^3}{3R} f_p\left(\frac{a}{H}\right)\right) \tag{B.3.22}$$

where $f_c\left(\frac{a}{H}\right) = \left(1 + \left(\frac{0.75}{\frac{a}{H}+\left(\frac{a}{H}\right)^3} + \frac{2.8(1-2v)}{\frac{a}{H}}\right)^{-1}\right)^{-1}$. The geometry correction factors, $f_p\left(\frac{a}{H}\right)$, $f_c\left(\frac{a}{H}\right)$ and $f_D\left(\frac{a}{H}\right)$ are applicable in the range $0 < a/H < 5$. Over the limit, the calculated values (e.g., indentation depth) might be negative.

Indentation test - Poroelasticity of the material was evaluated using the simple indentation test[152,154]. We poured the gel prepolymer into a glass petri dish (diameter: 50 mm, height: 17 mm) and cured it at 80 °C for 12 – 14 hours. A glass hemisphere (radius: 3.08 mm) was indented into the cured gel to fixed depth of 1, 2, and 3 mm, over 10 s. Each depth was maintained for 5 hours, and the resultant real-time force ($F(t)$), exerted from the gel, was measured in grams (g) over time (t) at 200 Hz. The measured force was normalized as $\Delta F = \frac{F(t)-F(\infty)}{F(0)-F(\infty)}$, and the measurement time was scaled as $\frac{t}{RD}$ where R is the radius of the glass hemisphere and D is the indentation depth. $\sqrt{RD}$ is the diffusive length scale of a spherical indenter[152]. If the gel is poroelastic, the normalized force collapses onto a single line over the scaled time, regardless of the indentation depth. However, if viscoelasticity predominates, the normalized force depends on the size (the indentation depth and sphere radius) when the normalized force is plotted against the normalized time. The normalized force collapsed onto a single line against the observation time (t), as shown in Figure B.3.15(a). Therefore, the scaled time with the diffusive length separates out each curve of the normalized force (see Fig. B.3.15(b)). This result resembles the previous work by Xu *et al.*[154].

Side view image processing - To detect boundaries from the raw images, we used the MATLAB built-in function imresize() and then binarized the ridge (cropped area) using graythresh() (see Fig. B.3.16(a)). The boundary was found using binaribwboundaries() and presented as red lines (see Fig. B.3.16(b)). Next, we extracted the boundary only corresponding to the glass sphere (see Fig. B.3.16(c)). The circle fitting was performed based on the boundary to find the glass sphere (see Fig. B.3.16(d)). The interconnecting points between the glass sphere and the gel were found using intersections() (see Fig. B.3.16(e)). At these points, the contact angle θ between glass-gel spheres was measured. This procedure was also applied to measure the contact angle between glass spheres and silicone oils droplets deposited on elastomer films.

Contact between a glass sphere and silicone oils deposited on an elastomer film - Silicone oil droplets with a volume of 4 µl were dispensed on an elastomer film coated on a glass slide with a thickness of ~ 40 µm (see Fig. B.3.17). A glass sphere was then placed on the deposited oil droplet. Silicone oils with viscosities of 100 mPa·s (Molecular weight: 104.22 kg/mol, ρ: 1.05 g/ml at 20°C and *n*: *n*20/*D* 1.453) (Sigma-Aldrich) and 50 mPa·s (Molecular weight:162.38 kg/mol, ρ: 0.96 g/ml at 25°C and *n*: *n*20/*D* 1.403) (Sigma-Aldrich) were used. The side view of the contact was taken, and the angle between the glass sphere and silicone oil was measured. Details of side view analysis are already provided earlier.

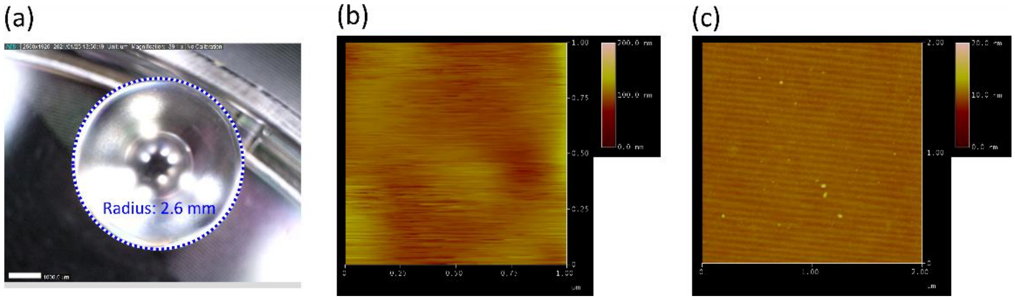

Figure B.3.1 Dimensions and surface roughness of glass contact pairs. (a) A representative top view of the glass sphere taken using a digital microscope (radius: 2.6 mm). **(b)** An AFM image of the glass sphere (radius: 2.6 mm): the arithmetic mean roughness, R_a = 7.96 nm, (Scanned area: 1 µm x 1 µm). **(c)** An AFM image of the bare glass slide: R_a = 0.39 nm (Scanned area: 2 µm x 2 µ m).

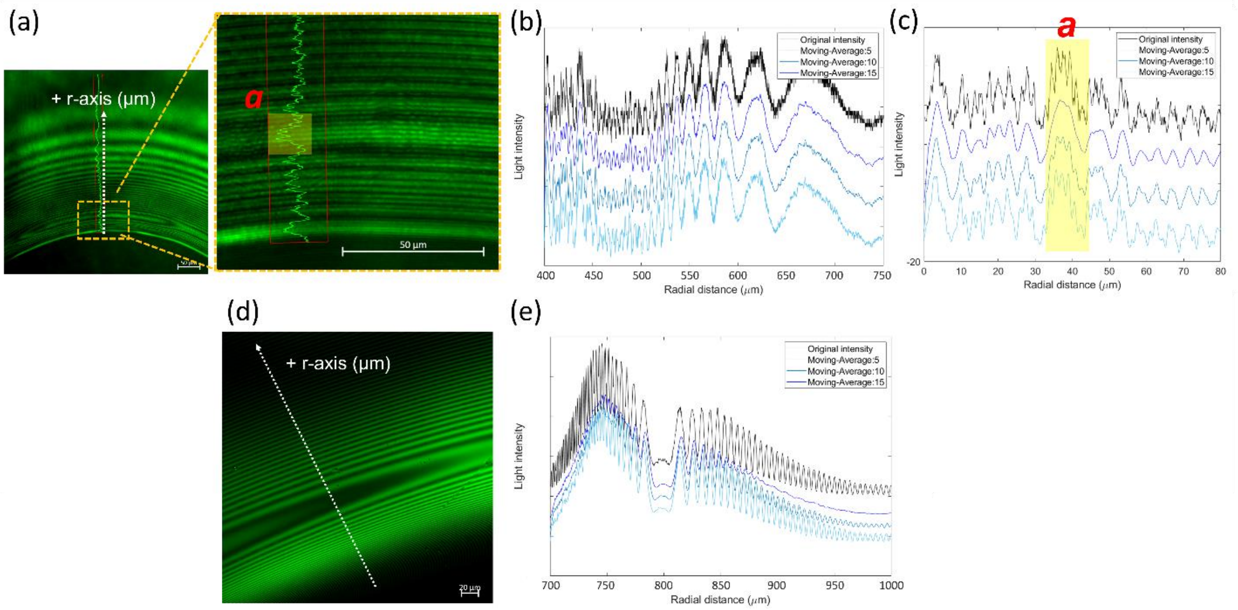

Figure B.3.2 Moving-average filtering of the resultant light intensity. (a) An interferogram between a glass sphere and a gel film (wavelength λ_g: 488 nm). **(b-c)** Normalized original intensity and filtered intensity through moving-average of 5 – 15 points over **(b)** 350 μm radial distance and **(c)** 80 μm radial distance (region *a*). Here, the origin of the radial distance is the center of the contact area. Numerical values in the vertical axis are omitted because filtered graphs are moved perpendicularly from the original intensity line to ease the comparison and not to overlap each other. **(d)** An interferogram of a droplet of silicone oil deposited between a glass sphere and glass slide (λ_g: 488 nm). **(e)** Normalized original intensity and filtered intensity through moving-average of 5 – 15 points over 300 μm radial distance. The noise level of the silicone oil between glass-glass is much lower than that between glass-gel-glass. Hence, only the signal amplitude decreases as increasing the averaged points from 5 to 15.

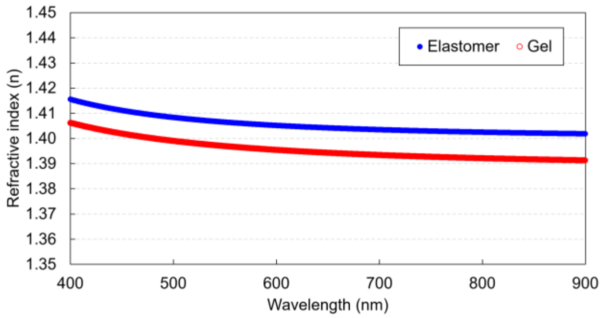

Figure B.3.3 Refractive indices of elastomer and gel films: coated on Si wafers measured using reflectometry. Measurements were repeated three times over the wavelength 400 – 900 nm, and all presented very close results. Therefore, one out of three measurements is shown for elastomer and gel, respectively.

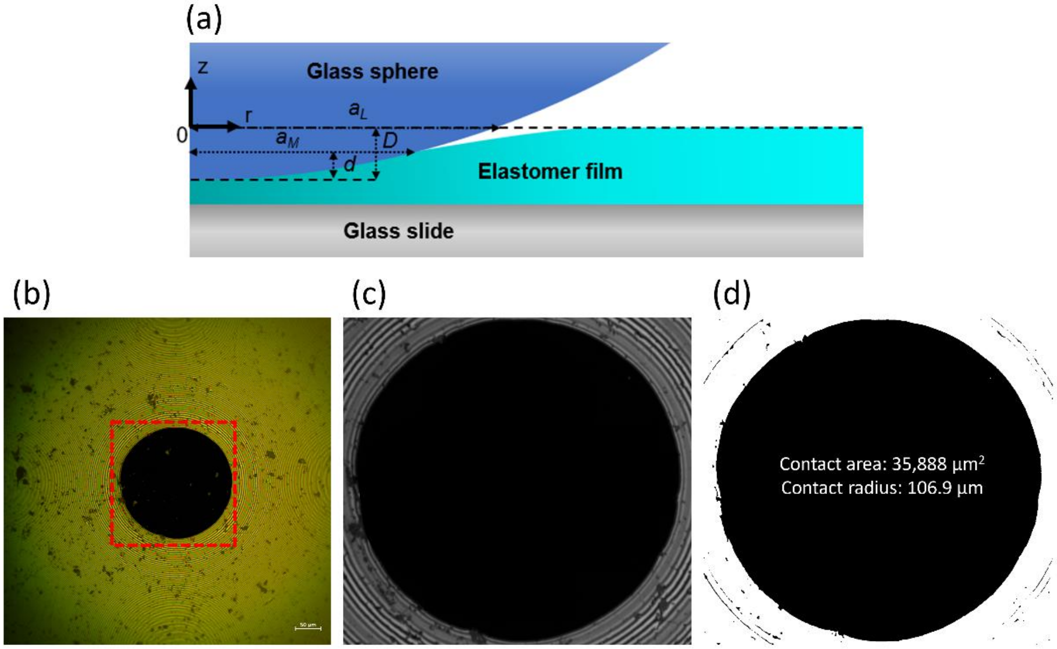

Figure B.3.4 Glass-elastomer-glass contact. (a) Schematic of the contact. **(b)** An interferogram with a focus on the surface of the elastomer film. **(c)** A magnified binary image of the dotted area in **(b). (d)** A bottom view of the contact area after processing the threshold treatment. The contact area (*A*) is measured based on the black colored-area, and the contact radius (*r*) is calculated according to $r = (A/\pi)^{1/2}$ assuming a perfect circle.

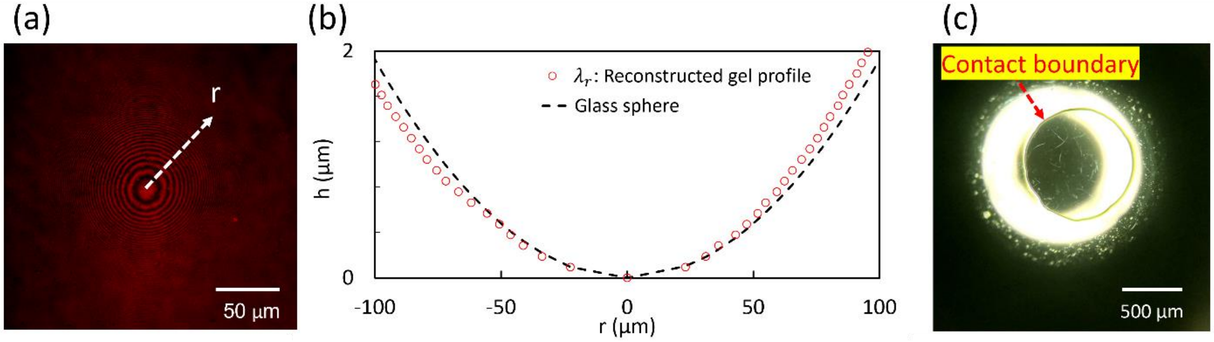

Figure B.3.5 Glass-gel-glass contact. (a) An interferogram with a focus on the center of the contact area at the interface between the glass sphere and gel film. **(b)** The reconstructed profile of the interface between the glass sphere and gel film, corresponding to the profile of the glass sphere ($\lambda_r = 561$ nm). **(c)** Bottom view of the contact taken using an inverted optical microscope.

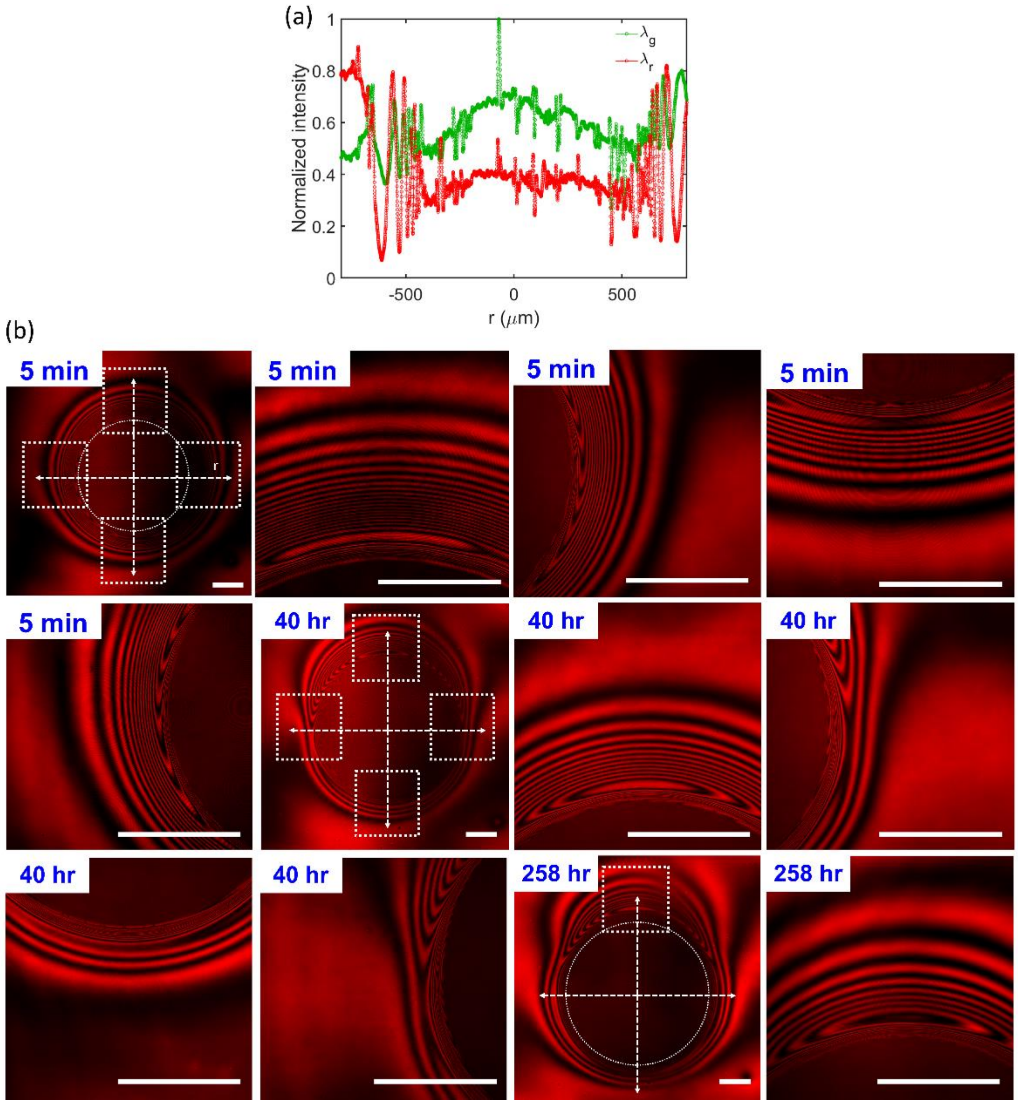

Figure B.3.6 Surface deformation of gel films with the thickness of 35 μm in transient states. (a) The resultant light intensities of the glass-gel contact over the radial distance of - 600 μm – 600 μm at the magnification 10×. **(b)** The frame time was ~ 5 min, so the shortest observation time after placing the glass sphere on the gel was 5 min. A magnified view at the magnification 40× is given on the right side when the dotted boxes are drawn. The interference rings near the contact boundary are not axisymmetric after 20 hr, implying the local pinning because of the potential local heterogeneity of the glass sphere or gel surface. The resultant light intensities were collected along the dotted lines as shown in the first figure (5 min). Scale bars: 200 μm.

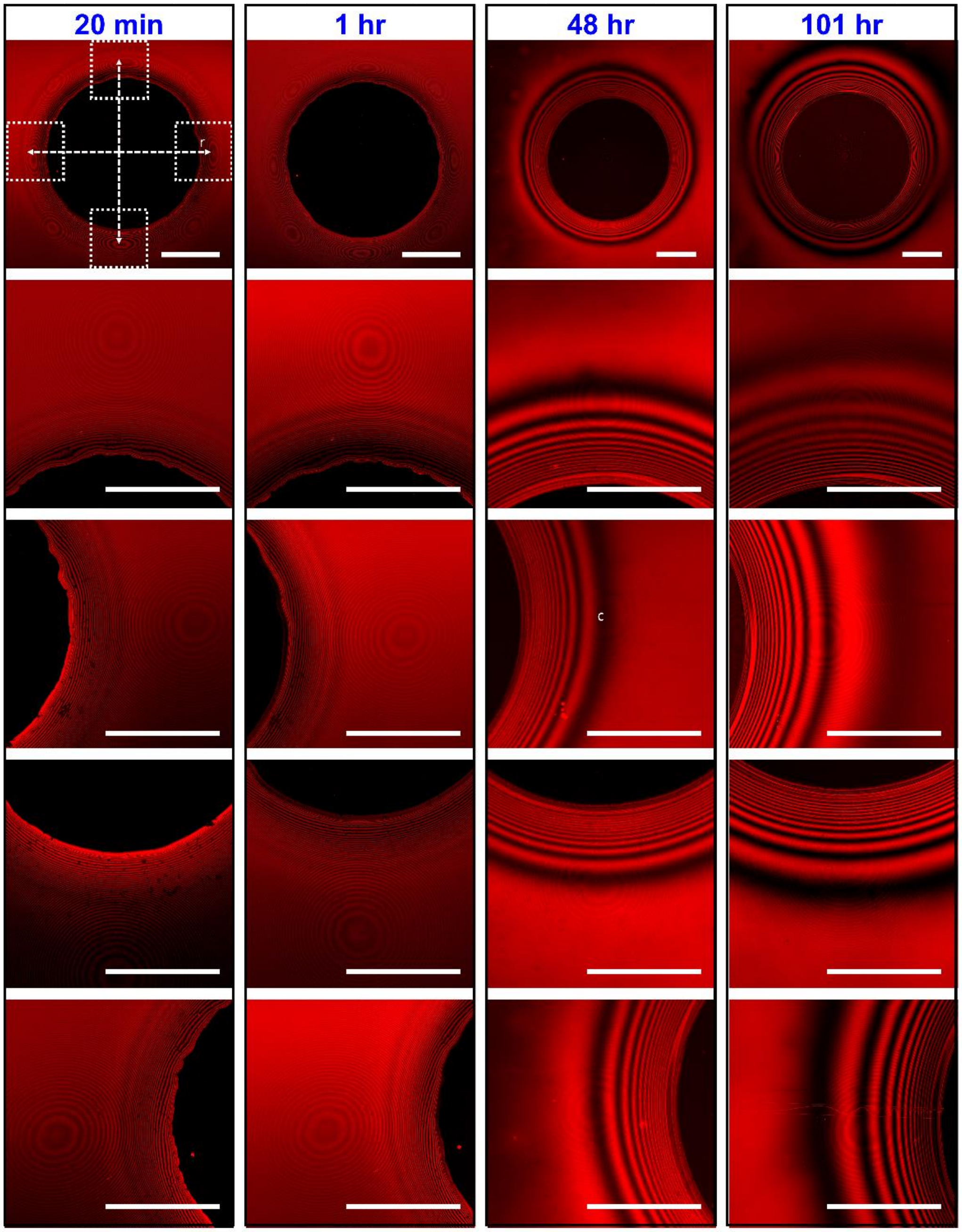

Figure B.3.7 Interferograms of evolving surface profiles of gel films with the thickness of 20 μm at different time scales: 5 min, 1 hr, 48 hr, and 101 hr contact. Four magnified views around the contact boundary at the magnification of 40× are given below each magnification of 10×. The resultant light intensities were collected along the dotted lines as shown in the first figure (20 min). Scale bars: 200 μm.

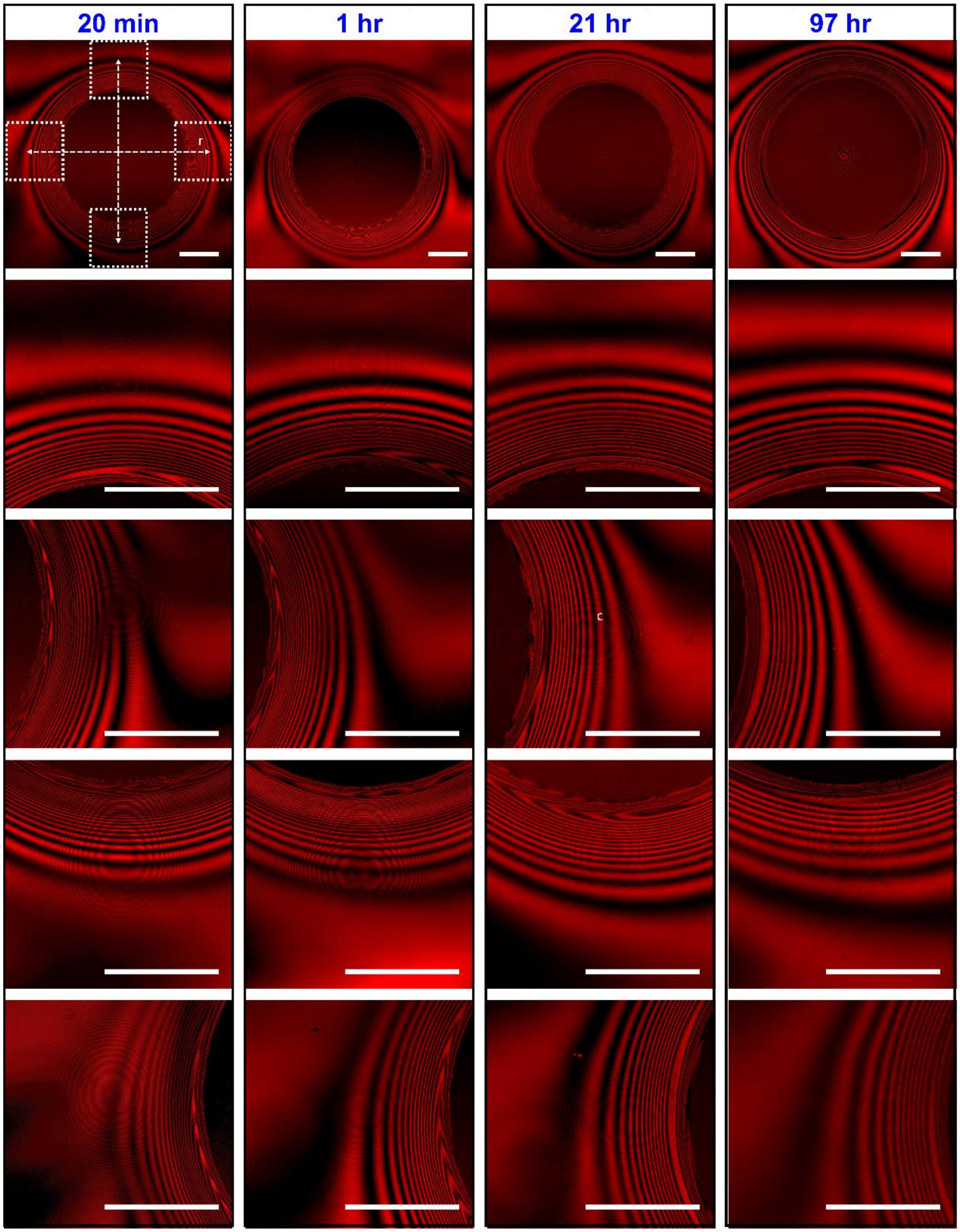

Figure B.3.8 Interferograms of evolving surface profiles of gel films with the thickness of 30 µm at different time scales: 20 min, 1 hr, 21 hr, and 97 hr contact. Four magnified views around the contact boundary at the magnification of 40× are given below each magnification of 10×. The resultant light intensities were collected along the dotted lines, as shown in the first figure (20 min). Scale bars: 200 µm.

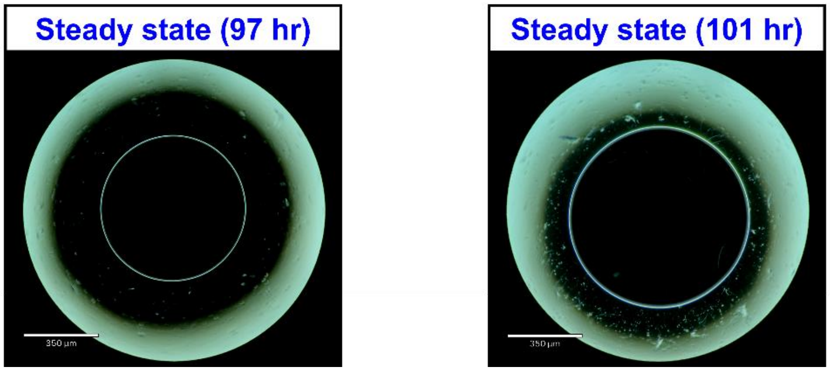

Figure B.3.9 Optical microscopic bottom views at the steady state: gel films with the thickness of 20 µm (left) and 30 µm (right). Scale bars: 350 µm.

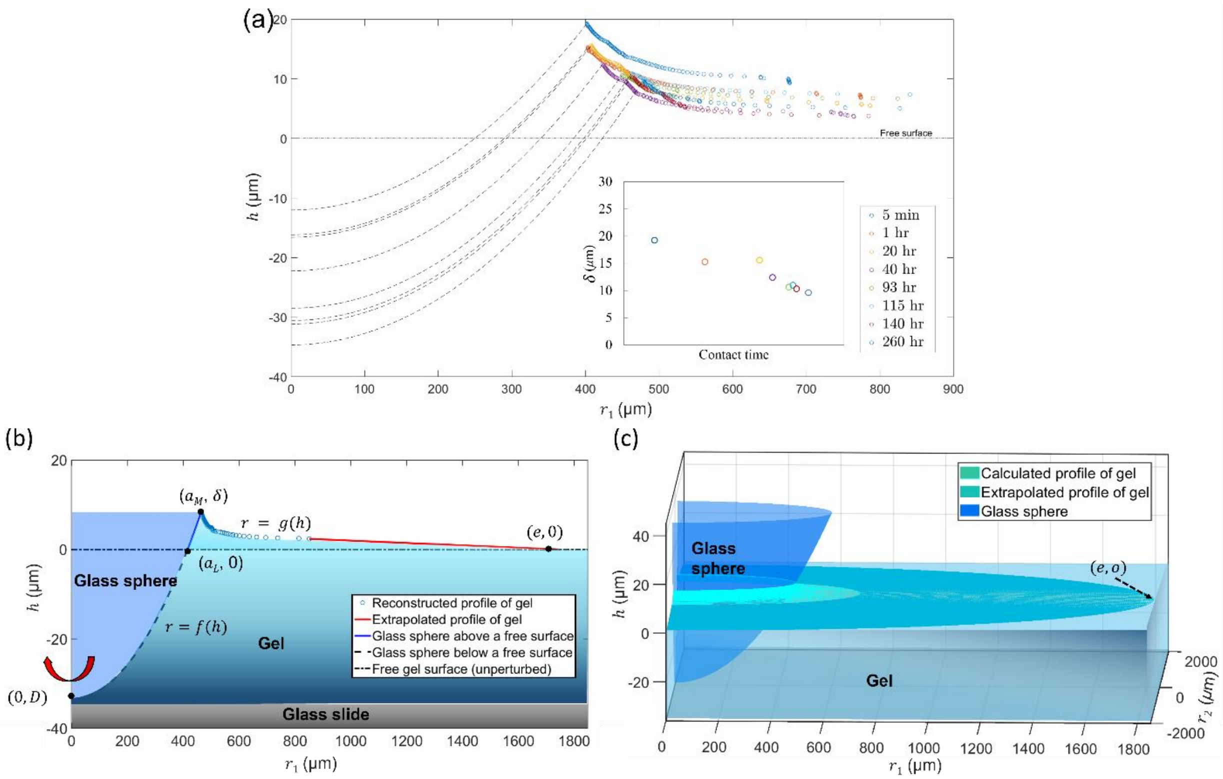

Figure B.3.10 Reconstruction of the gel deformation. (a) The representative 2D view of the gel deformation over time. Calculated profiles (*h*) are only shown, without the extrapolated profile of the gel. The ridge height (δ) is plotted against the contact time in the sub-plot. The free gel surface is at $h = 0$. **(b)** The representative view of 2D surface profile of the gel intercalated between the glass sphere and glass slide at the steady state (258 hr). **(c)** The representative reconstructed view of the 3D gel deformation at the steady state, drawn by rotating figure **(b)** with respect to z-axis. The glass sphere is indented ~ 35 μm under the free surface (unperturbed) of the gel ($h = 0$). The brightest fluorescent blue at the contact boundary is reconstructed based on the interferograms (calculated profile), and the outer transparent dark blue indicates the extrapolated surface profile of the gel based on the calculated profile of the gel. Only half of the 3D view is given to prevent the extreme distortion of the image due to the large aspect ratio between the gap distance, *h* (from -35 to 40 μm) and the radial distance, *r* (from -1900 to 1900 μm for the full view).

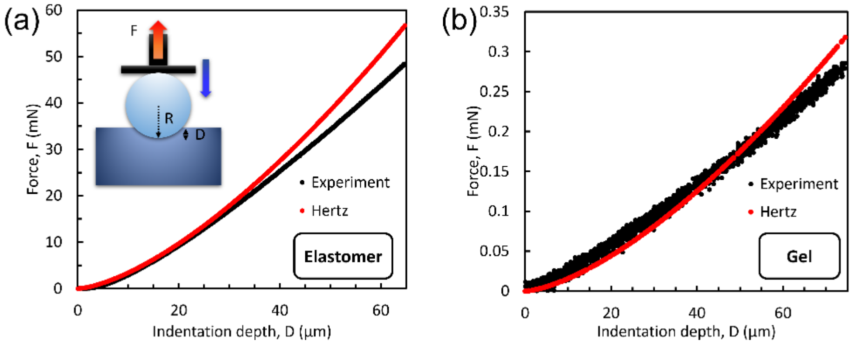

Figure B.3.11 Force (F) and indentation depth (D) data for the elastomer and gel. (a) The elastomer film in contact with the glass sphere with a radius of 2.6 mm. **(b)** The gel film in contact with the glass sphere. The force curve calculated with Hertz theory is given with each experimental data.

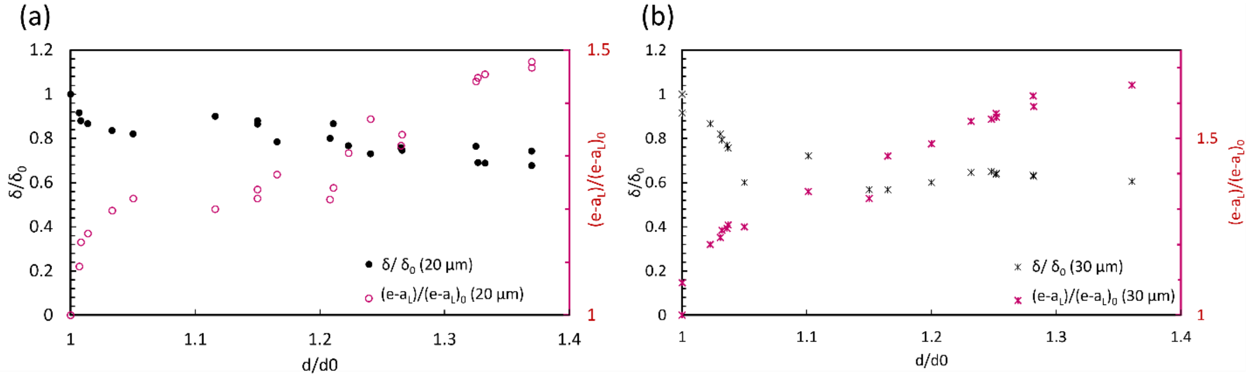

Figure B.3.12 Evolvoing ridge height and width over time: The normalized ridge height (δ/δ_0) and the normalized ridge width $(e-a_L)/(e-a_L)_0$ against the normalized submerged depth (d/d_0). Gel thin films with the thickness of **(a)** 20 µm and **(b)** 30 µm.

Appendix C

C.1 Experimental

Measurement of the average flow rate - The volumetric flow rate at the outlet was evaluated by measuring the weight of the flowing fluid. The fluids at the outlet of the soft wall channel were collected in a plastic beaker, which was hung on a hook connected to the load cell of a universal mechanical tester (UMT-2MT, Center for Tribology, Inc.). The beaker was covered using tape to prevent the evaporation of the fluids while measuring the weight. The initial weight of the tape and the beaker were subtracted from the measured weight. The real-time weight of the fluids was measured in grams with a frequency of 200 Hz, as shown in Figure C.4.1(a). The flow rate at the outlet was the same as the imposed inlet flow rate applied using the syringe pump, as presented in Figure C.4.1(b).

Fabrication of PDMS films - To investigate the surface properties and the swelling degree of PDMS in water, we fabricated PDMS films. PDMS base and cross-linker were mixed in weight ratios of 10:1 and 35:1 using a planetary mixer (Thinky Corporation, ARE-310) for 8 minutes. The mixed pre-polymer was poured in a petri-dish (diameter: 100 mm). Here, the volume of the pre-polymer was decided to achieve film thickness, 2 mm. The pre-polymer was cure at 21 – 23 °C for 12 hours first, and then at 80 °C for 24 hours. After curing, the films were cut in 60 mm × 10 mm. We submerged the cured PDMS films in DI water for 4 days, like the preparation process of the soft wall channels. At the same time, for controls, three PDMS films at each mixing ratio were kept in the air at 21 – 23°C for 4 days. Each preparation method is arranged in Table C.4.1.

Table C.4.1 Fabrication conditions of each PDMS film.

	$\mathbf{P10_{bare}}$	$\mathbf{P35_{bare}}$	$\mathbf{P10_{air}}$	$\mathbf{P35_{air}}$	$\mathbf{P10_{water}}$	$\mathbf{P35_{water}}$
Curing	At 21 – 23°C for 12 hours and then, at 80 °C for 24 hours					
Post-treatment	N/A		Exposed in the air at 21 – 23 °C for 4 days		Submerged in DI water at 21 – 23 °C for 4 days	

Extraction of free oligomers - We poured 2.0 g pre-polymer of each silicone elastomer (after mixing in each weight ratio as mentioned in the main manuscript) in a rectangular metal mold with 2 cm × 2 cm dimensions. The pre-polymers were cured at 21 – 23 °C for 12 hours, and then in an oven at 80°C for a day. The fully cured samples were carefully removed and then placed in large jars filled with HPLC grade pentane (Fisher Scientific) for one week. Pentane was replaced every two days. The fully swollen samples were dried for two to three days. Before the pentane treatment and after the dry step, the weight of samples was measured. Three to four samples were tested.

Swelling of PDMS in water - We confirmed the swelling of PDMS films by comparing the weight of PDMS films before and after being immersed in DI water. We immersed the PDMS films in DI water for 4 days until the swelling was equilibrated. Also, after evaporating the water absorbed in the PDMS for 1 day at 21 – 23˚C, the PDMS films were weighed again. The degree of swelling was expressed by the following ratio:

$$Swelling\ ratio\ (\%) = \frac{W_s - W_d}{W_d} \times 100 \tag{C.4.1}$$

where W_d and W_s are the weight of PDMS before and after 4 days in water, respectively. Three individual films were tested, and we used a scale that measures up to four places of decimals in gram.

Static and dynamic contact angle measurements - The static and dynamic contact angle (CA) of water were analyzed under ambient conditions at 21 – 23˚C on a drop shape analyzer (Krüss, DSA30). In the static CA measurement, a DI water drop with a controlled volume of 5 µl was dispensed on a PDMS film using an automatic dispenser. The baseline was selected manually. The static CA was measured using the tangential method programmed on the ADVANCE software (Krüss). The needle-embedded sessile drop method was used to measure the dynamic CA. Firstly, a DI water drop with a volume of 1 µl was deposited on a PDMS film, and a 9 µl volume was more dispensed at a controlled volumetric rate of 1 µl/s. After then, the droplet was sucked up from the surface at the same rate of 1 µl/s. The deformation of the droplet was filmed continuously. When de-pinning occurred in increasing and decreasing the droplet volume, the advancing and receding angles were determined, respectively, using the tangential method on the ADVANCE software.

C.2 Results and Discussion

The fraction of free oligomers in the PDMS network - Untethered monomers and oligomers in the elastic network were extracted using solvent extraction. The weight of each PDMS sample before/after the solvent extraction was measured. Also, for the control, bare PDMS at each mixing ratio was kept in air and weighed together. The normalized weight of each sample ($= \frac{the\ sample\ weight\ at\ each\ condition}{the\ initial\ sample\ weight}$) is given in Figure C.4.1. By decreasing the ratio of the cross-linker, more free oligomers were extracted. The amount of untethered free oligomers in the P35 network (33.5 wt.%) was approximately seven times larger than the P10 network (4.9 wt.%).

Swelling of PDMS films in water - After 4 days in DI water, P10 maintained clear transparency, but P35 changed to be an opaque white (Fig. C.4.2(a)). This transparency change indicates the diffusion of the water through the PDMS, and a small volume of water could be absorbed in PDMS. Therefore, even if the poor compatibility between PDMS and water was reported, the degree of swelling of PDMS was investigated [215]. Both P10 and P35 absorbed water and the weight increased. P10 films presented a 0.02 % lower degree of swelling than P35 films on average (see Fig. C.4.2(b)). The degrees of swelling for both P10 and P35 were zero after they were dried under ambient conditions for one day; P10 and P35 returned to the initial weight.

Surface properties of PDMS films - P10 and P35 films were investigated with CA and sliding angle measurements (see Figs. C.4.3(a) and (b)). Each data presents the average measured values of at least three individual measurements, which creates the error bars of the data points. In the case of $P10_{water}$ and $P35_{water}$, the surface of the films was wiped out using a Kimwipe tissue before the test. The static CAs of P10 and P35 did not demonstrate a noticeable change, maintaining 115° and 130°, respectively, regardless of the preparation conditions.

In the dynamic CA, the advancing CAs of PDMS films were maintained similarly in different conditions, but the receding CAs increased after 4 days (Figs. C.4.3(a) and C.4.4). $P10_{air}$ and $P10_{water}$ represent ~ 20° increased receding CAs compared to $P10_{bare}$. $P35_{air}$ and $P35_{water}$ showed ~ 5° increased receding CAs than $P35_{bare}$. Hence, the difference between the advancing and receding CAs, called CA hysteresis, decreased after 4 days, which could originate from the migration of the un- or partially-crosslinked polymers with low molecular weights from the crosslinked networks to an air-PDMS interface. In all conditions, P35 films have a lower receding CA than P10 films. During withdrawing the water drop, no residual water was left on the PDMS films. The advancing CA measures the dry-wetting interaction between PDMS-water, while the receding CA represents the remaining interaction between PDMS-water, thus implying that the P35 has higher adhesion to water than P10.

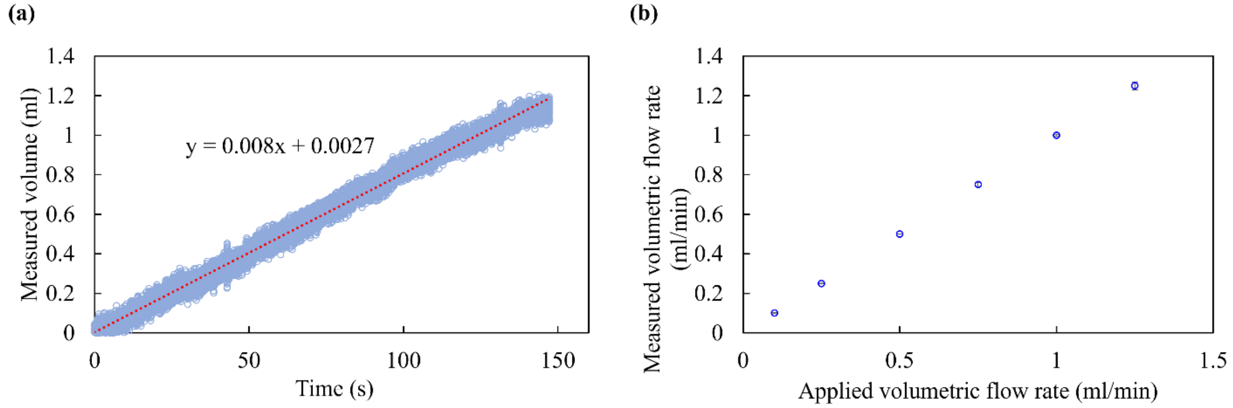

Figure C.4.1 Volumetric flow rate of the fluidic system. (a) The measured volume (ml) of water at the outlet of the P20 soft wall channel using a universal mechanical tester (UMT-2MT) for ~ 150 s when applying 0.5 ml/min at the inlet using a syringe pump. **(b)** The measured volumetric flow rate (ml/min) against the applied volumetric flow rate (ml/min). Error bars are presented, which are the standard deviations of three measurements. The error bars are covered by the data markers due to the small deviations. The measurements were repeated three times at each flow rate.

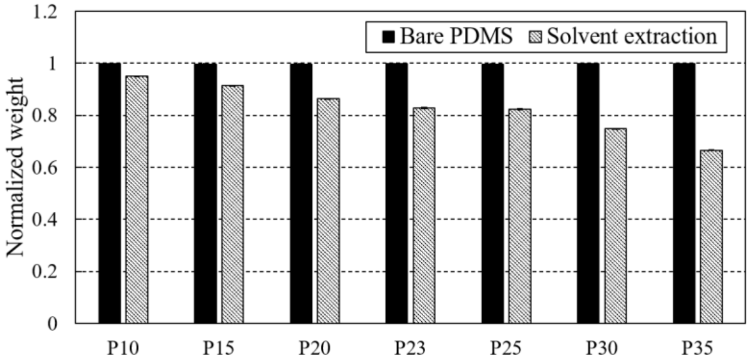

Figure C.4.2 The normalized weight of each PDMS mixing ratio before and after solvent extraction. Error bars are the standard deviations calculated with at least three individual measurements. Due to the negligible value of each error bar, error bars are not visible on the graph.

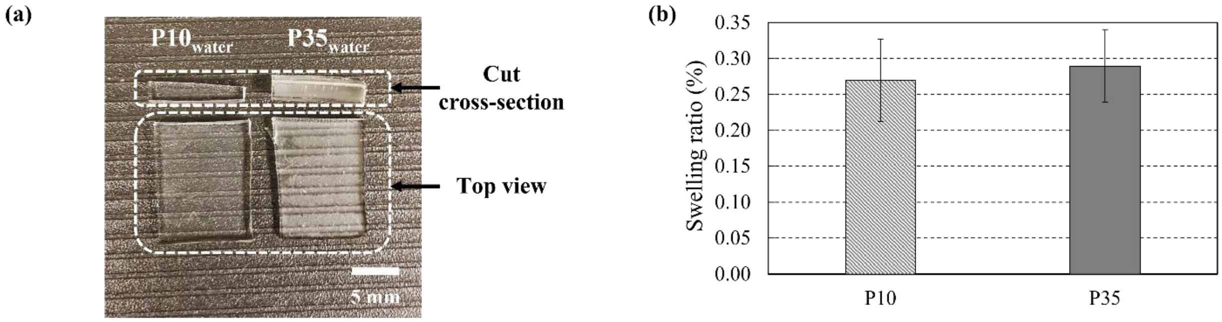

Figure C.4.3 Swelling of PDMS films in water. (a) The cut cross-section and top views of P10$_{water}$ and P35$_{water}$ films. Scale bar: 5 mm. **(b)** The degree of swelling (%) before and after immersion in water for 4 days. Error bars are the standard deviations calculated with three to four individual measurements.

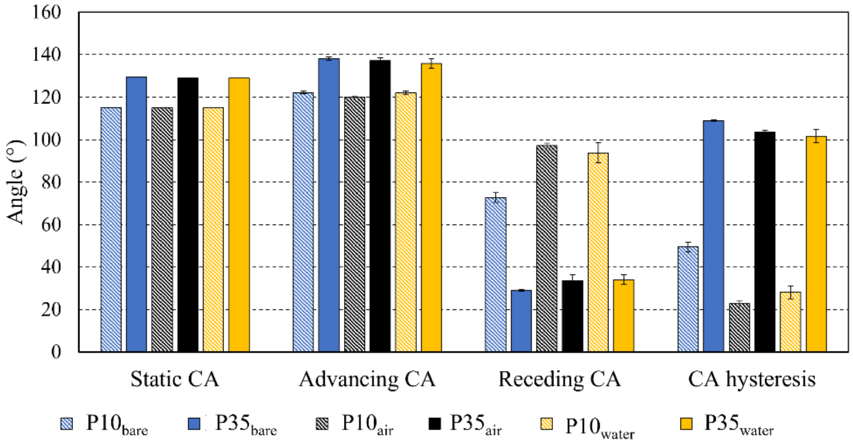

Figure C.4.4 Surface properties of PDMS in different conditions: The measured static CA, dynamic CA, and sliding angle. Error bars are the standard deviations calculated with three to four measurements.

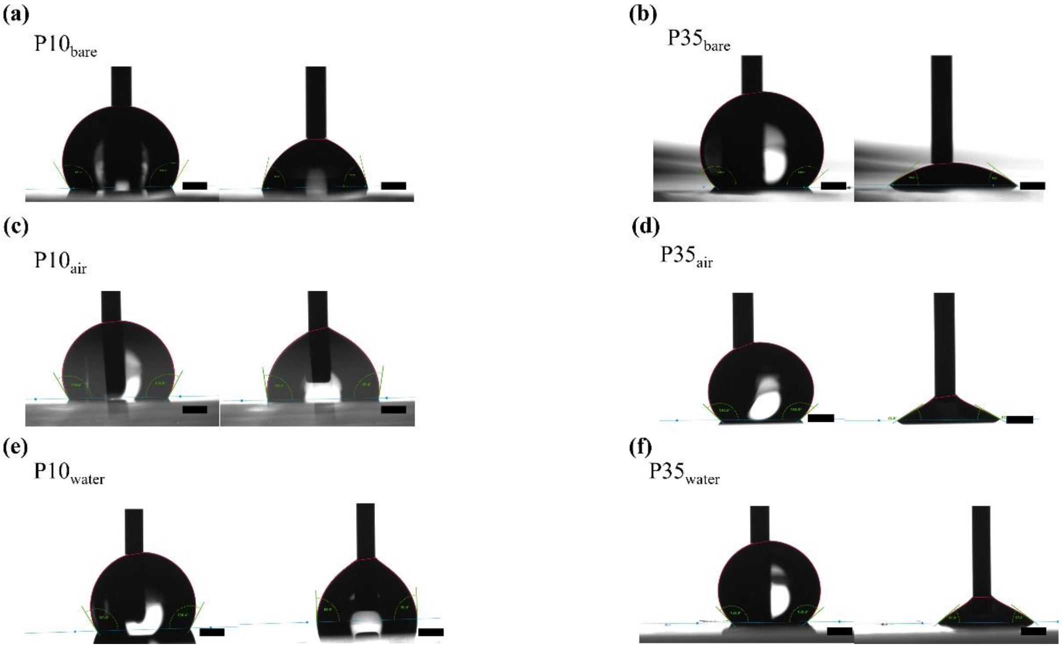

Figure C.4.5 Representative images of dynamic contact angle of PDMS films in different conditions: the advancing contact angle (left) and the receding contact angle (right) in each condition. **(a)** P10_{bare}. **(b)** P35_{bare}. **(c)** P10**air**. **(d)** P35_{air}. **(e)** $\text{P10}_{\text{water}}$. **(f)** $\text{P35}_{\text{water}}$. Scale bar: 0.5 mm.

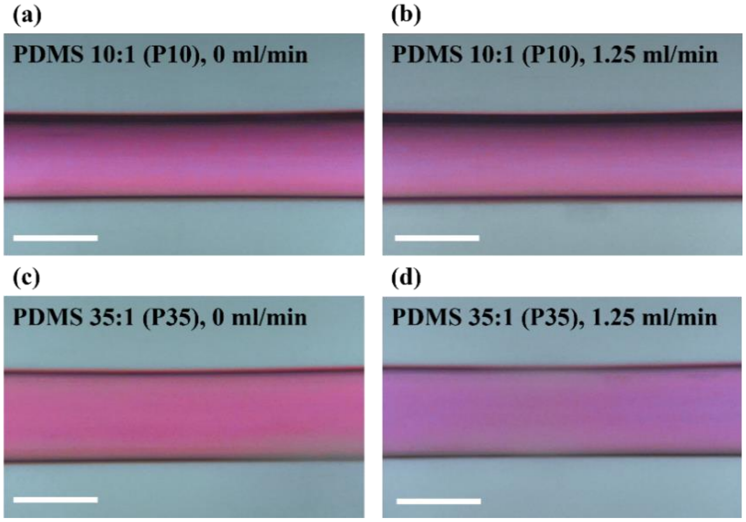

Figure C.4.6 The soft wall channels within confinement tubes (cellulose tubes) before and after flowing DI water mixed with a red dye. PDMS 10:1 soft wall channel at volumetric flow rates of **(a)** 0 ml/min. and **(b)** 1.25 ml/min. PDMS 35:1 soft wall channel at **(c)** 0 ml/min. and **(d)** 1.25 ml/min. Scale bar: 500 μm.

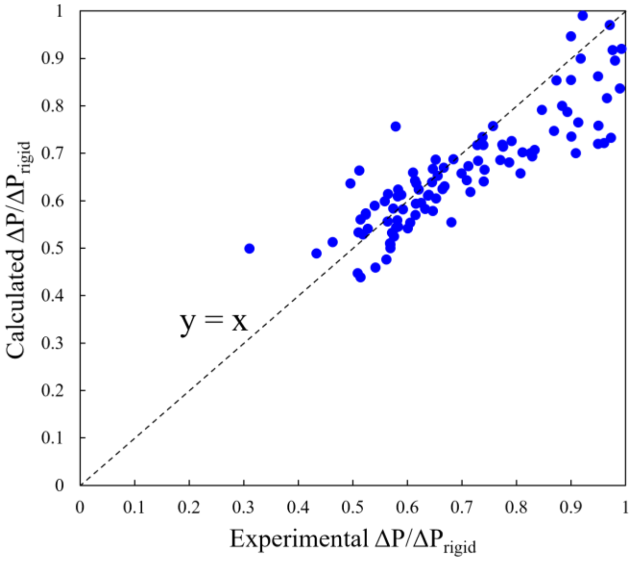

Figure C.4.7 The experimental normalized pressure ($\Delta P/\Delta P_{rigid}$) against the calculated $\Delta P/\Delta P_{rigid}$ using Eq. (4.7).

Appendix D

Table D.5.1 Physical properties of Acrylamide (AAm) solvent for different monomer weight percentage.

Monomer weight %	Surface tension, γ (mN/m)	Density, ρ (kg/m^3)
2.5	70.9±0.2	999.7
4.0	69.6±0.1	1001.0
6.3	65.7±0.1	1003.1
6.5	65.6±0.2	1003.3
7.0	65.6±0.1	1003.8
7.5	64.8±0.3	1004.3
10.0	64.2±0.2	1006.8
13.0	61.9±0.1	1009.8

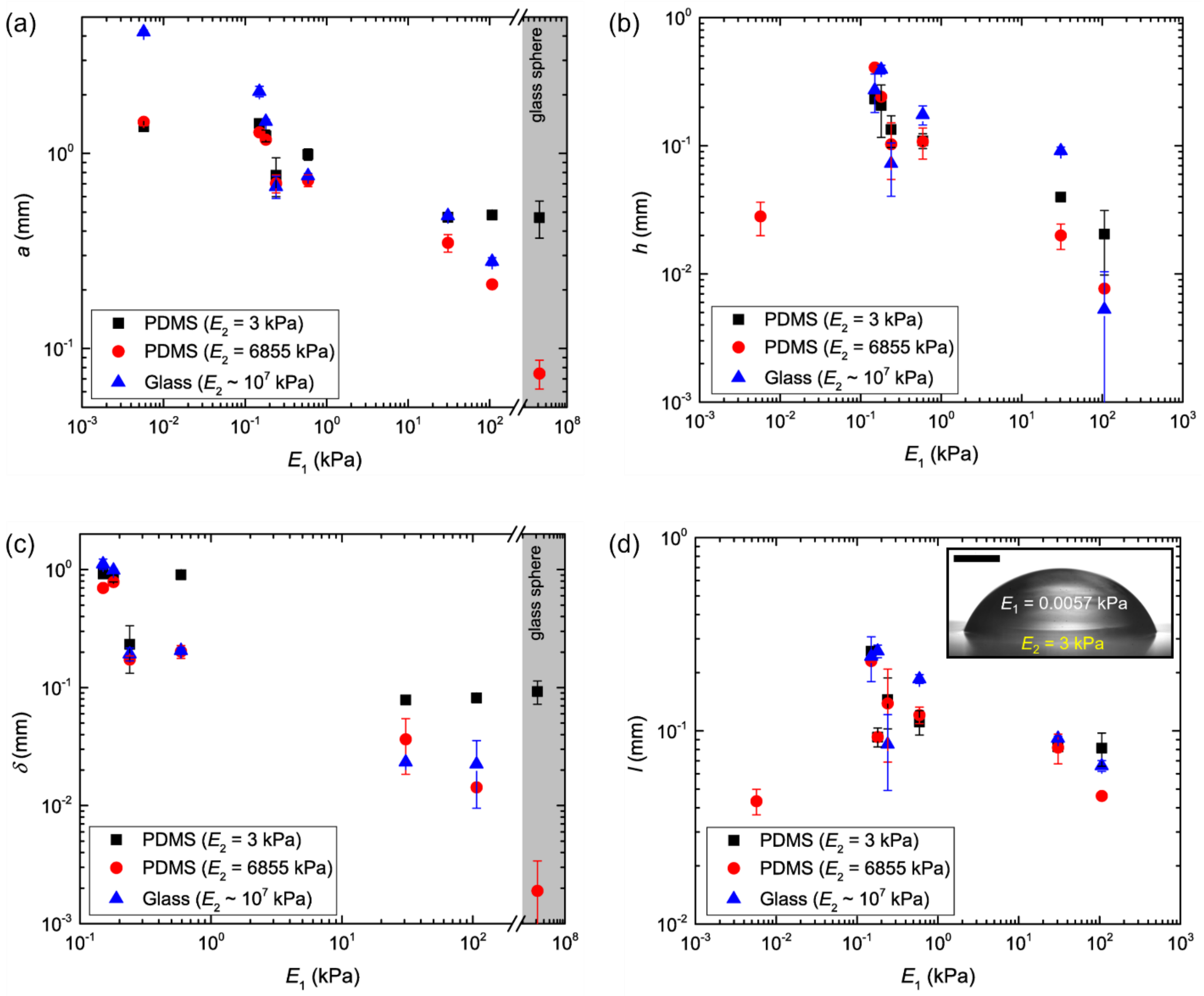

Figure D.5.1 Hydrogels on pristine PDMS. Variation of hydrogel contact radius **(a)**, foot-height **(b)**, apparent indentation depth **(c)** and foot-length **(d)** for different hydrogel elasticity (E_1) on relatively soft PDMS ($E_2 = 3$ kPa), relatively stiff PDMS ($E_2 = 6855$ kPa) and rigid glass slides ($E_2 \approx 107$ kPa). The data for rigid glass sphere is also shown for **(a)** and **(c)**. The hydrogel with the lowest elasticity, *i.e.*, $E_1 = 0.0057$ kPa exhibits no foot on the softest PDMS substrate, *i.e.*, $E_2 = 3$ kPa (inset of **(d)**). The radius of hydrogel is $R_0 \approx 1$ mm. All soft substrates are 2 mm thick.

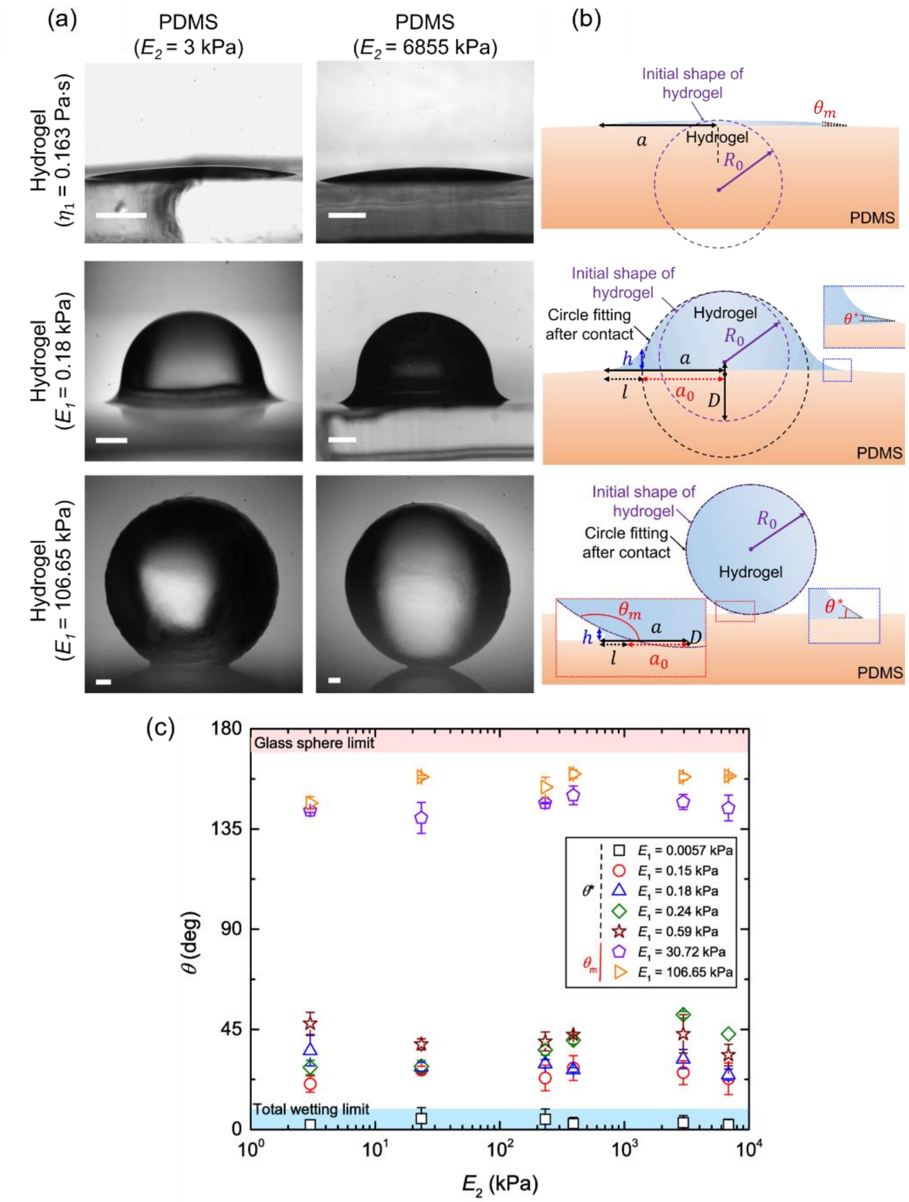

Figure D.5.2 Hydrogel configurations on plasma-treated PDMS. (a) Experimental snapshots of the static configuration of different hydrogels on plasma-treated soft substrates with elasticity $E_2 = 3$ kPa and $E_2 = 6855$ kPa. Scale bars represent 0.5 mm. **(b)** Schematics of the different possible hydrogel profiles of initial radius R_0 on the soft substrates. θ_m and θ^* are the macroscopic and foot contact angles, respectively. a and a_0 are the real and apparent contact radius, respectively. δ is the apparent indentation depth. h and l are the foot height and length, respectively. **(c)** Variation of contact angles (θ_m, θ^*) of the hydrogels of different elasticity E_1 on plasma-treated soft substrates of different elasticity E_2.

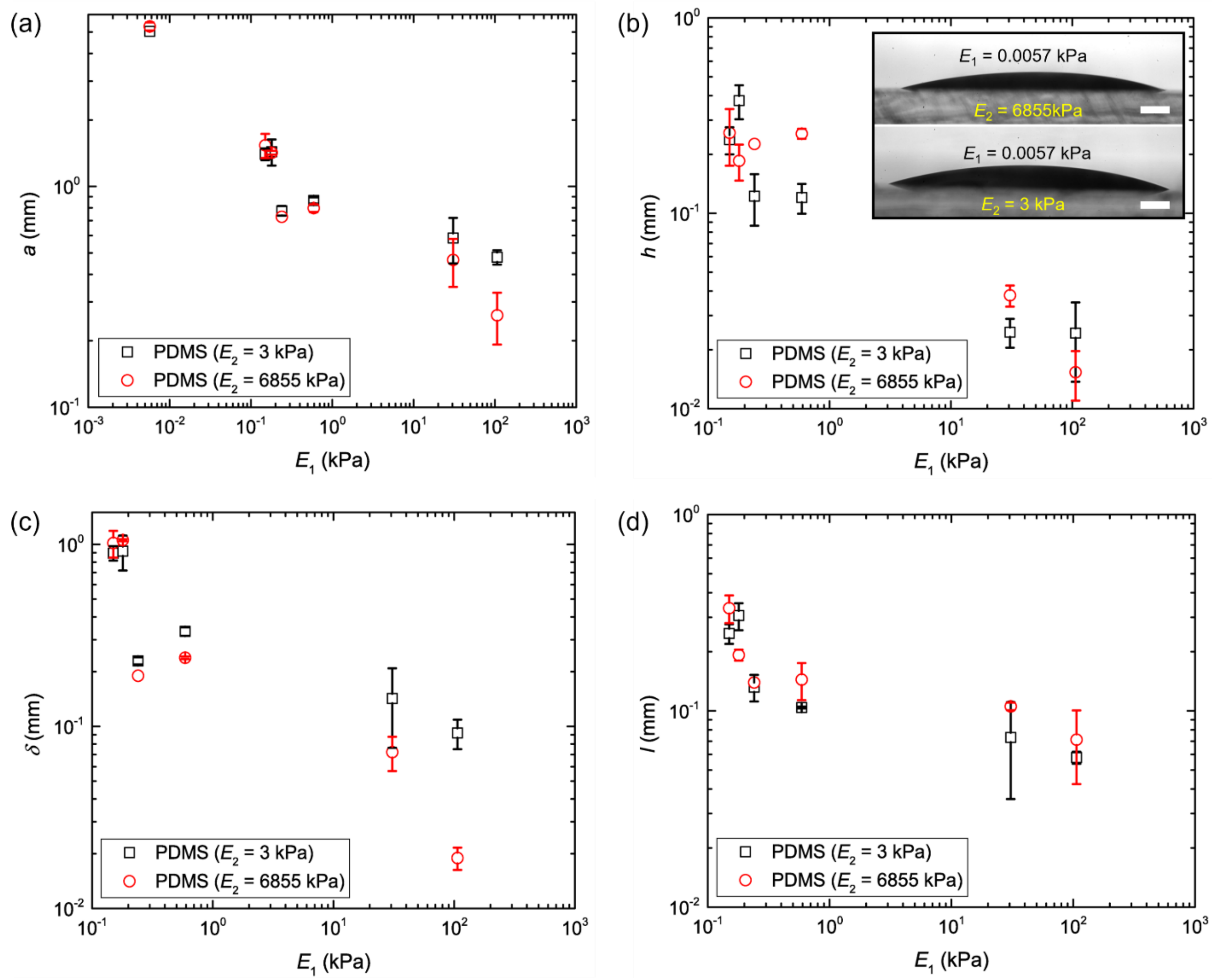

Figure D.5.3 Hydrogels on plasma-treated PDMS. Variation of hydrogel contact radius **(a)**, foot- height **(b)**, apparent indentation depth **(c)** and foot-length **(d)** for different hydrogel elasticity (E_1) on relatively soft PDMS ($E_2 = 3$ kPa) and relatively stiff PDMS ($E_2 = 6855$ kPa). The hydrogel with the lowest elasticity, *i.e.*, $E_1 = 0.0057$ kPa exhibits no foot on either of the plasma-treated PDMS substrates (inset of **(b)**). The radius of hydrogel is $R_0 \approx 1$ mm. All soft substrates are 2 mm thick.

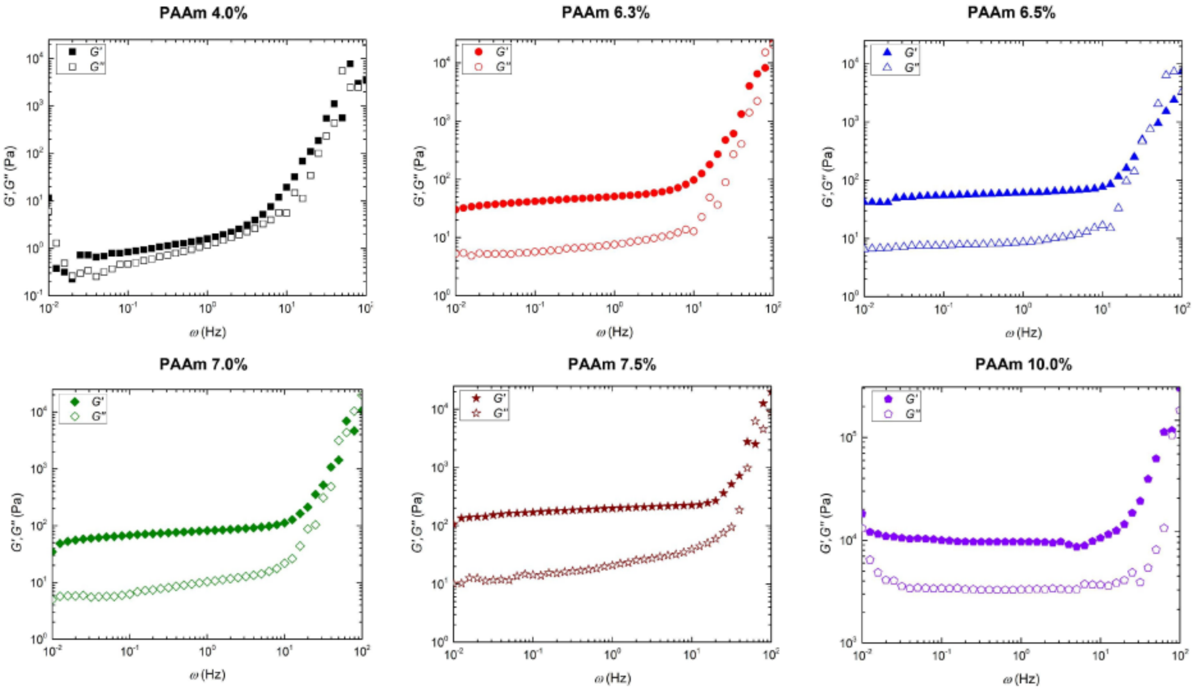

PAAm 4.0%

PAAm 6.3%

PAAm 6.5%

PAAm 7.0%

PAAm 7.5%

PAAm 10.0%

Figure D.5.4 Rheology of hydrogels. Variation of storage modulus (G') and loss modulus (G'') with angular frequency ω for hydrogels with different monomer weight percentages. The static shear modulus G is calculated using $G = \sqrt{G'^2 + G''^2}$ at $\omega = 1$ Hz.

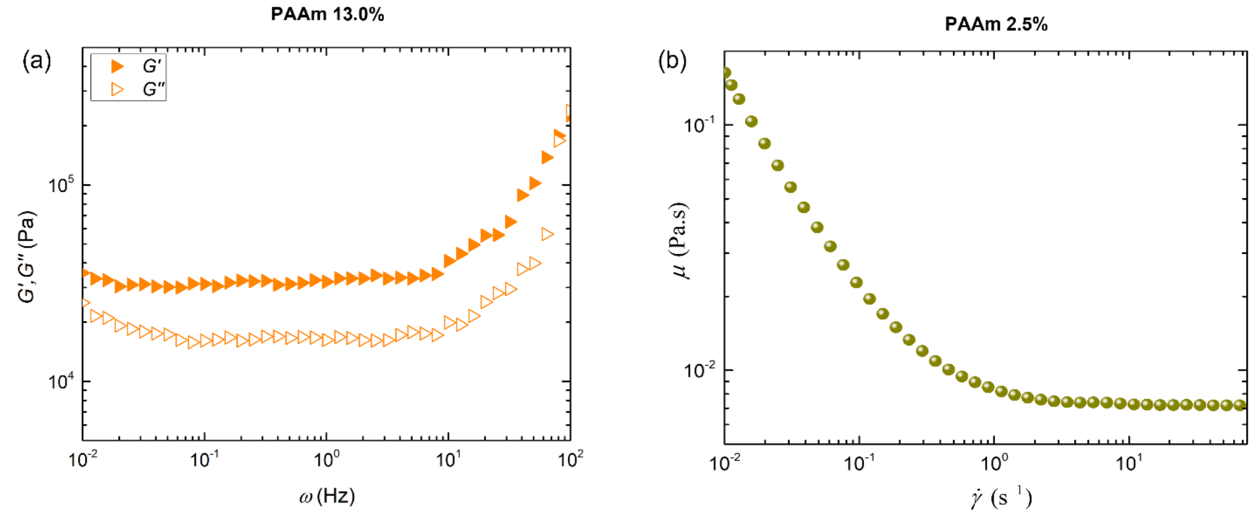

Figure D.5.5 Rheology of hydrogels. (a) Variation of storage modulus (G') and loss modulus (G'') with angular frequency ω for PAAm 13.0%, *i.e.*, hydrogel with 13.0% monomer weight percentage. The static shear modulus G is calculated using $G = \sqrt{G'^2 + G''^2}$ at $\omega = 1$ Hz. **(b)** Variation of shear viscosity η with shear rate $\gamma^{\cdot}$ for the liquid hydrogel, *i.e.*, hydrogel with 2.5% monomer weight percentage.

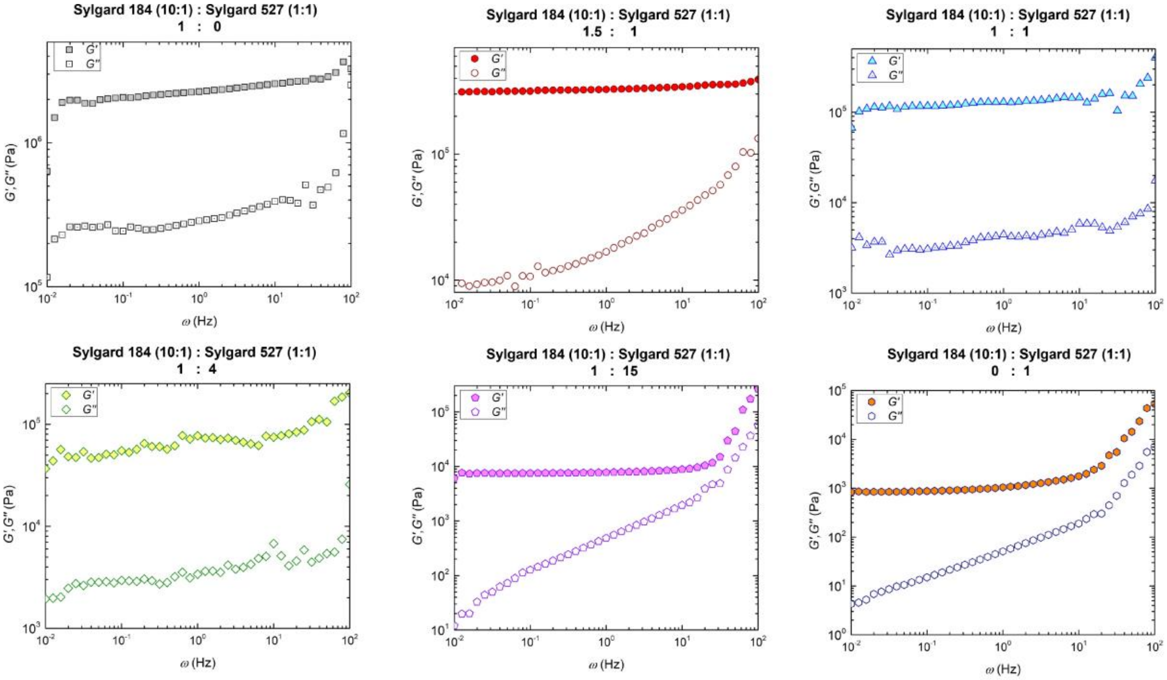

Figure D.5.6 Rheology of soft substrates. Variation of storage modulus (G') and loss modulus (G'') with angular frequency ω for substrates prepared combining Sylgard 184 PDMS (10:1) and Sylgard 527 (1:1) in different weight ratios. The static shear modulus G is calculated using $G = \sqrt{G'^2 + G''^2}$ at $\omega = 1$ Hz.

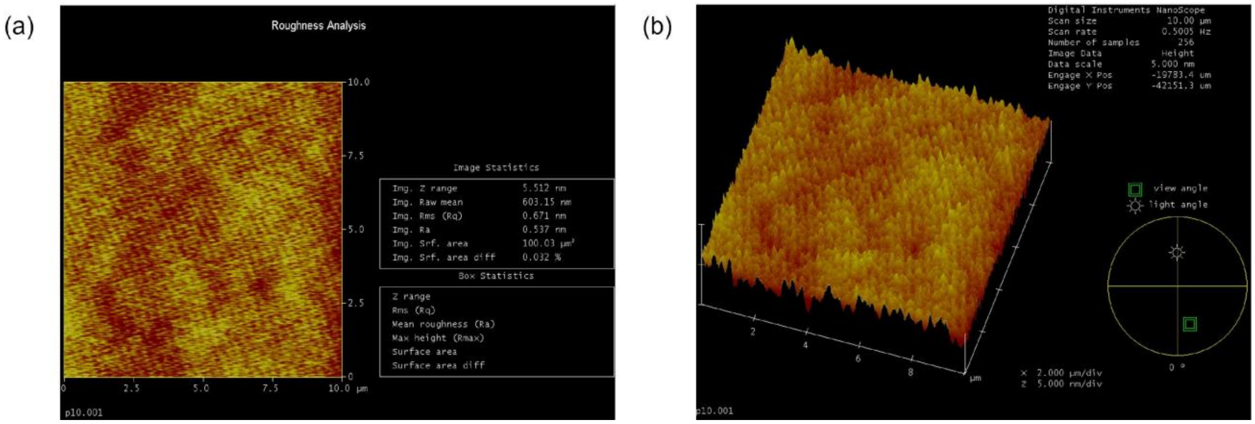

```
Image Statistics
Img. Z range             5.512 nm
Img. Raw mean            603.15 nm
Img. Rms (Rq)            0.671 nm
Img. Ra                  0.537 nm
Img. Srf. area           100.03 µm²
Img. Srf. area diff      0.032 %
Box Statistics
Z range
Rms (Rq)
Mean roughness (Ra)
Max height (Rmax)
Surface area
Surface area diff
```

```
Digital Instruments NanoScope
Scan size                 10.00 µm
Scan rate                0.5005 Hz
Number of samples           256
Image Data               Height
Data scale             5.000 nm
Engage X Pos        -19783.4 um
Engage Y Pos        -42151.3 um
```

Figure D.5.7 AFM measurements. (a) Atomic force microscopy (AFM) scan on a 10 µm × 10 µm cross-section of a plasma treated PDMS substrates with elastic modulus, $E_2 = 6855$ kPa. R_q and R_a values for the scan are shown. **(b)** Three-dimensional profile of the scan shown in **(a)**.

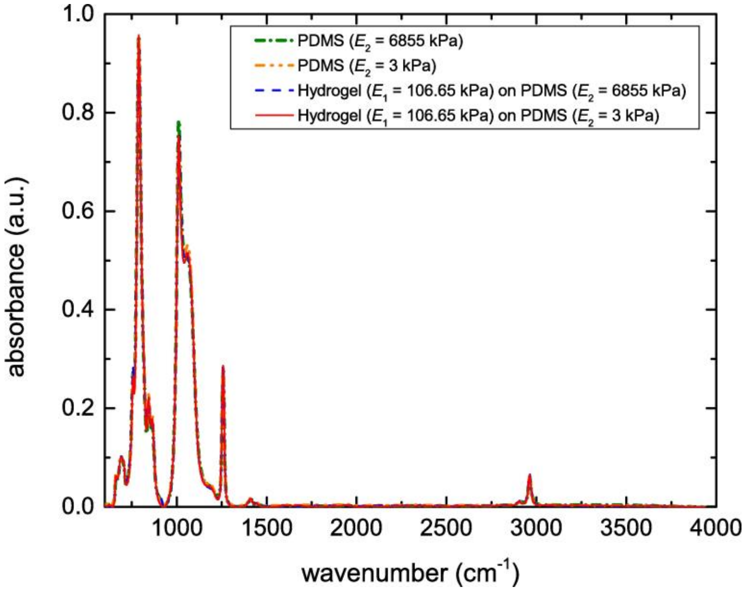

Figure D.5.8 FTIR measurements. FTIR spectra for pristine 2 mm thick PDMS substrates ($E_2 = 3$ kPa and $E_2 = 6855$ kPa) and the same substrates with hydrogel ($E_1 = 106.65$ kPa) deposition.

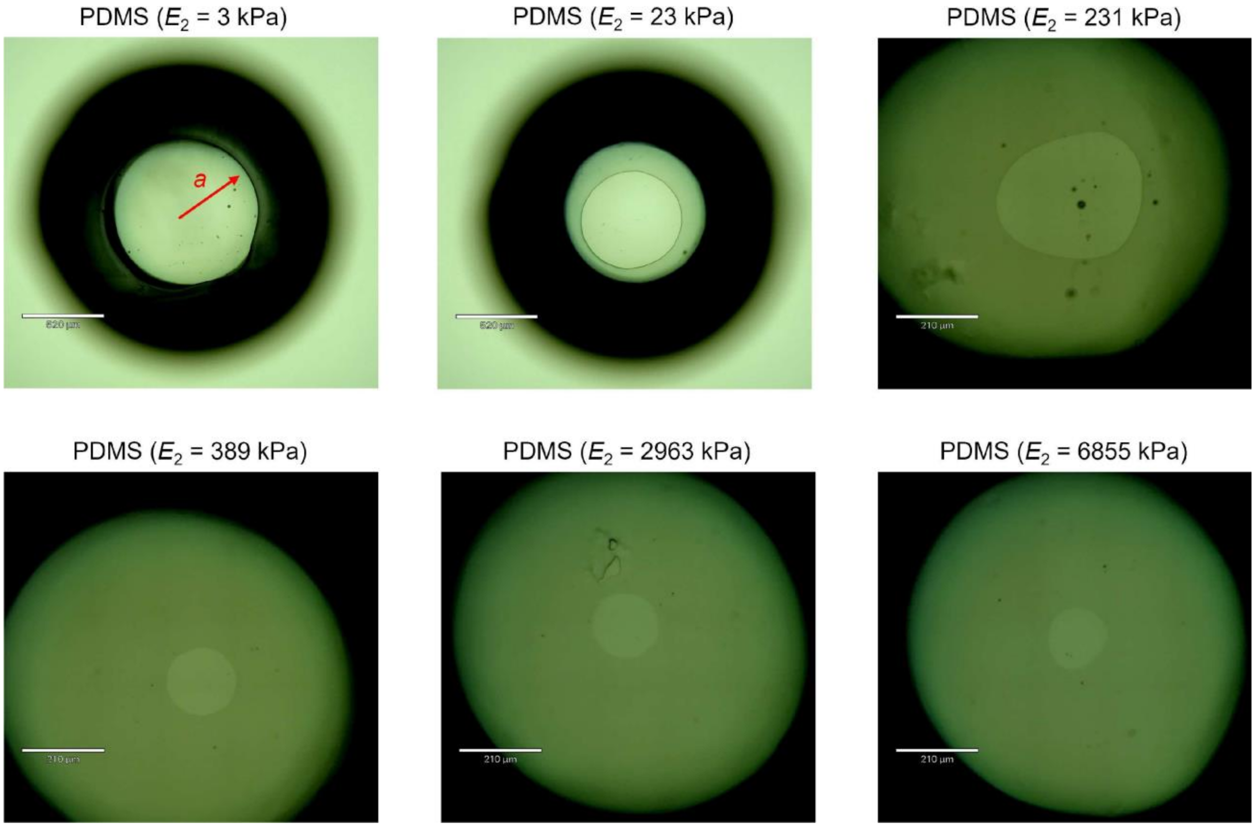

Figure D.5.9 Glass sphere on soft PDMS. Bottom-view bright-field microscopy images of 1 mm radius rigid glass spheres in contact with soft PDMS substrates of varying elasticity (E_2). a denotes the contact radius. Note the different scale bars.